Deformation and Aerodynamic Performance of a Ram-Air Wing

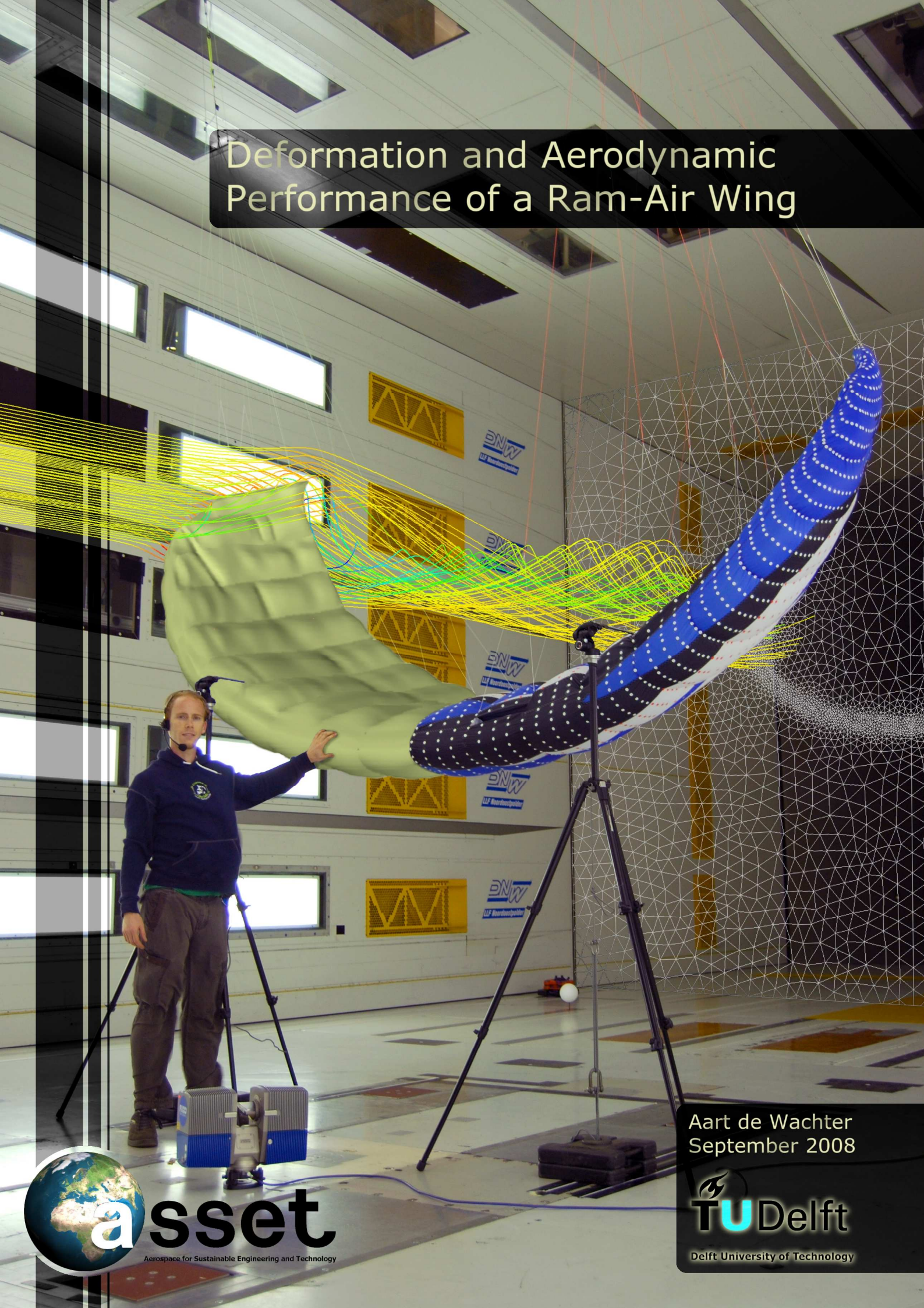

Aart de Wachter
September 2008

asset
Aerospace for Sustainable Engineering and Technology

TU Delft
Delft University of Technology

Deformation and Aerodynamic Performance of a Ram-Air Wing

Master thesis by Aart de Wachter

Graduation committee:

Prof.Dr. W.J. Ockels
Ir. L.M.M. Boermans
Ir. J. Breukels
Dr. R. Ruiterkamp

September 30th, 2008

Delft University of Technology
Faculty of Aerospace Engineering

Copyright

Preface

Before I wrote the project proposal for my master thesis in November 2007 first I wrote down all the things that I wanted to learn and do before I would leave the University. Then I tried to cast all these things into one project. With a few minor changes and additions the project was accepted. It became a project that was even more exciting than winning 3rd price in the AIAA aircraft design competition in 2003.

Because this is a very multidisciplinairy report it won't go into all the underlying theory of the treated subjects. But to make reading easier there is a basic introduction into the most important aspects of this report. The reader should at least be familiar with the basics of aerodynamics. Readers who are unfamiliar with ram-air wings are referred to chapter 3 for a brief explanation about ram-air wings. A basic introduction about computational fluid dynamics, laser scanning and photogrammetry is found in appendices A, B and C.

I owe a number of people my thanks for cooperating with me in this project. The time in the windtunnels with Roland, Max, Jeroen and Jochem was simply unforgettable. Thanks for your help, support and all the fun guys!

A few more thank-you's to the other people that were involved in this project, so thanks:

- To Jeroen Breukels and Richard Ruiterkamp, my two graduation supervisors, for their guidance.
- To Loek Boermans for having a seat on the graduation committee.
- To the people of the University of Stuttgart for all their help and assistance.
- To the team of the German-Dutch Windtunnel Institute for allowing us to use their facilities.
- To Nikon for all the cameras and lenses.
- To Max Dereta for his fantastic photographs.
- To the people of superbus for their help while I was using their CFD facilities.
- To the people of the Department Earth Observation and Space systems for their help with laser scanning and photogrammetry.
- To Nana for taking care of my administrative mess.

But most of all thanks to my professor Wubbo Ockels for making this whole project possible.

I hope you will enjoy reading this report and learn as much from it as I did.

Aart de Wachter
September 30th, 2008
Delft, The Netherlands

Abstract

Ram-air wings form an ever increasing market of soft fabric, air inflated wings. They are primairily used in air sports such as parachuting, paragliding and kiting. Ram-air kites may also be used for electric power generation by letting the kite pull a cable from a drum that is connected to a generator. An example if this principle is the Laddermill concept.

But since ram-air wings are flexible by nature they will deform and depart from their intended design shape when they are loaded by aerodynamic forces. These deformations generally affect the performance of the wings adversely.

Kites with a higher lift-to-drag ratio on the Laddermill could mean a direct increase of the energy produced per square meter of kite. Besides this benefit for the Laddermill there is a huge, world-wide market of parachuting, paragliding and kiting that can benefit from more research and a better understanding of the deformation and aerodynamic performance of ram-air wings.

The goals of this thesis are to be able to point out where a ram-air kite departs from the intended design shape, to investigate how well the kite performs, to understand how the deformations affect the airflow and to make suggestions for possible improvements of the design. Since little has been published about these subjects this report will most of all form a basis for further research.

This report presents a method to analyse the shape and the aerodynamics of a ram-air kite. The kite is tested in the windtunnel. Its 3D shape is captured using two techniques: photogrammetry and laser scanning. Using the geometry data the structural deformation of the wing is dissected. With computational fluid dynamics the aerodynamics of the deformed shape is analyzed. An extra result of this study is the comparison of photogrammetry and laser scanning in terms of their suitability to capture the 3D shape of the ram-air kite.

A number of interesting deformations and flow features were found on the ram-air wing:

- Theoretically the bumps (ballooning) and grooves on a ram-air wing hinder the spanwise flow on a 3-dimensional wing, but in practise this effect is only visible on small parts of the upper surface.
- The pull of the suspension lines on the under surface and the internal construction of the wing make the upper surface of the wing deform. This results in a decrease of the upper surface curvature, especially near the nose. This curvature decrease causes a loss of lift of at least 5%.
- Because the flat, 2-dimensional fabric is inflated into a 3-dimensional shape the fabric wrinkles. The wrinkles continue from the top and bottom surface into the ribs that internally connect and support the top and bottom surface. On average these wrinkles shorten the ribs in chordwise direction by 3.5%. This decreases the surface area of the wing and it makes the ribs effectively thicker.

Many more details became visible with the thorough analysis of the wing's shape. The conclusion is that the performance of the ram-air wing can be improved by changing these details. The photogrammetry measuring technique gave better results than laser scanning and is very suitable tool to make these details visible. It allows a designer to identify where the real flying shape deviates from the design shape. This can help kite designers and designers of other ram-air wings to reverse-engineer a ram-air wing such that it takes the intended shape when it is flying.

Contents

Nomenclature

G = $9.81 m/s^2$

b' = projected span [m]
C_L = lift coefficient [-]
C_P = pressure coefficient [-]
D = drag [N]
d = out of plane deflection of the wing tips [m]
$dC_L/d\alpha$ = lift slope
F = measured force [N]
k = turbulent kinetic energy [m^2/s^2]
k = wing efficiency factor (Oswald factor) [-]
L = lift [N]
L = reference length to calculate Reynolds number
L/D = lift-to-drag ratio
$(L/D)_K$ = lift-to-drag ratio of a kite [-]
R_a = resultant aerodynamic force [N]
Re = Reynolds number [-]
S = wing area [m^2]
V = velocity [m/s]
V_A = airspeed [m/s]
V_C = cross wind speed [m/s]
V_L = line reel out speed [m/s]
V_W = free stream wind speed [m/s]
W = weight of the kite [N]
y^+ = scaled coordinate normal to a wall

α = angle of attack [degrees]
β = camber factor [-]
β = compressibility correction $\sqrt{1 - Mach^2}$ (only figure 4.7b)
$\Delta\theta$ = pitch angle correction for weight of the kite
ε = turbulent dissipation rate [m^2/s^3]
μ = dynamic viscosity [$Pa \cdot s$]
ρ = air density [kg/m^3]
τ = local anhedral angle (camber angle) [degrees]
ω = specific dissipation rate [1/s]

Abbreviations:
2D = 2 dimensional
3D = 3 dimensional
AoA = angle of attack
BWK = Böenwindkanal (= turbulent wind tunnel)
CAD = computer aided design
CFD = computational fluid dynamics
FEA = finite element analysis
FSI = fluid-structure interaction
HD = high definition
IR = infra red
LLF = Large Low-speed Facility
RMS = root-mean-squared
URF = under relaxation factor

x

1 Introduction

The demand for clean, renewable energy is ever rising. The chair of Aerospace for Sustainable Engineering and Technology (ASSET) of Delft University of Technology applies innovative technology to produce renewable energy.

The main focus of ASSET is on the Laddermill project. It utilizes large kites to pull a cable from a drum that is connected to a generator. In this way wind power from high altitudes can be captured. The energy that can be produced by such a system is very much dependent on the performance (by "performance" the lift-to-drag ratio is meant) of the kites. Apart from rigid wings, ram-air wings are amongst the best performing kites. These soft fabric wings obtain their aerodynamic shape from the air that is pushed into the wing through openings at the nose. They are cheaper, lighter, require less material and are easier to transport and store than rigid wings.

But since ram-air wings are flexible by nature they will deform and depart from their intended design shape when they are loaded by aerodynamic forces. These deformations generally affect the performance of the kites adversely. Kites with a higher lift-to-drag ratio on the Laddermill could mean a direct increase of the energy produced per square meter of kite (this is explained in chapter 2).

Besides this benefit for the Laddermill there is a huge, world-wide market of parachuting, paragliding and kiting that can benefit from more research and a better understanding of the deformation and aerodynamic performance of ram-air wings.

The goals of this thesis are to be able to point out where a ram-air kite departs from the intended design shape, to investigate how well the kite performs, to understand how the deformations affect the airflow and to make suggestions for possible improvements of the design. Since little has been published about these subjects this report will most of all form a basis for further research.

This report presents a method to analyse the shape and the aerodynamics of a ram-air kite. The kite is tested in the windtunnel. Its shape is captured using two techniques: photogrammetry and laser scanning. Using the geometry data the structural deformation of the wing is dissected. With computational fluid dynamics the aerodynamics of the deformed shape is analyzed. These are the first steps of a reverse-engineering process with which the shape and aerodynamics of a ram-air wing can be improved. The last steps of this process, actually making changes to the construction of the kite and testing the effects, is not part of this thesis. An extra result of this study is the comparison of photogrammetry and laser scanning in terms of their suitability to capture the 3D shape of the ram-air kite.

The detail of the geometry analysis depends on the accuracy of the method that is used to capture the geometry of the wing. With the techniques used in this thesis analysis is restricted to the global deformations of the wing. Local material strain is not included.

To give the reader a better understanding of the Laddermill project and of the market of ram-air wings, chapters 2 and 3 address these two topics in more detail. Chapter 4 goes into the most elementary deformation of ram-air wings: ballooning. As an example the lift and drag changes and flow phenomena due to ballooning on the NACA0012 airfoil are investigated. This part of the project was finished before the windtunnel test on the actual ram-air wing. Chapter 5, 6 and 7 form the core of the report. Chapter 5 explains the windtunnel tests. In chapter 6 the geometric deformations of the kite are discussed in detail and chapter 7 deals with the computational fluid dynamics analysis of the shapes that were measured in the windtunnel. The conclusions from the foregoing chapters are summed up in chapter 8.

2 Laddermill

The laddermill is an electrical generator that produces renewable energy. It utilizes large kites to pull a cable from a drum that is connected to a generator, as depicted in figure 2.1. In this way windpower from high altitudes can be captured.

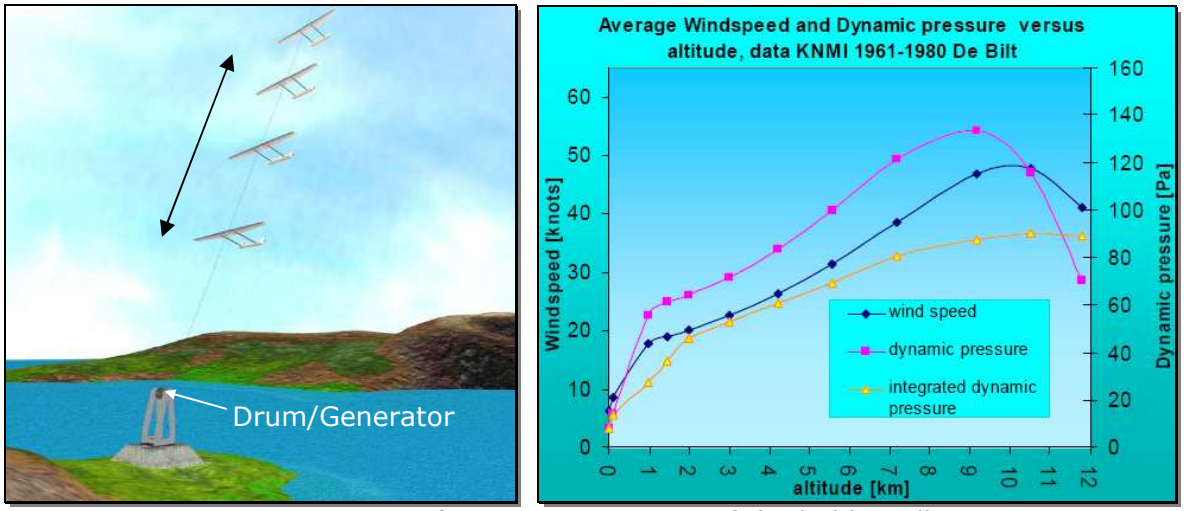

Figure 2.1: Left: Artist impression of the laddermill. Right:Wind speed and dynamic pressure versus altitude. [6]

Looking at figure 2.1, one can say that from windturbine technology the next step in wind power generation is to go to high altitudes. Modern large wind turbines operate in between 50 and 150 meters. Increasing this height to 1km already gives a four fold increase in dynamic pressure, the kinetic energy per cubic meter of air.

With the ground station that arrived in the summer of 2008 the Laddermill is capable of generating up to 18kW of wind power. The generator of this ground station is what currently limits the power output. In the future it will be sized up to several megawatts. At the moment the Laddermill is flown with a $10m^2$ Peter Lynn Venom II kite, a C-shaped ram-air kite. This kite differs from the kite that is shown on the front page in that its bottom surface is not supported by a cascade of bridle lines. It is only supported at the tips. This makes the kite form into a C-shape. The unique feature of this particular kite is that it is self stabilizing. This means that when the controls are in a neutral position the kite will stay in zenith, right above the ground station. Most kites that are controlled with four lines don't possess this property. When left uncontrolled they turn towards the ground and crash in seconds. A disadvantage of a C-kite is that, compared to bridled kite with a flatter surface area and higher aspect ratio, it is less efficient. A large part of the lift acts sideways and is not used to pull on the lines, but to pull the tips apart.

Figure 2.2: The C-shaped ram-air kite of the Laddermill.

The potential of power generation with a kite on a tether was shown in the article "Cross wind kite power" by Loyd [17]. He showed that a Laddermill with one kite that has the properties of a C5 cargo airplane can theoretically produce 6.7MW in a 10m/s wind. Back then in 1980 that was about three times the output of a windturbine. Today it is still more than the largest commercially available windturbines.

The kite is able to produce such a large amount of energy because it flies perpendicular to the free stream wind direction. This situation is sketched in figure 2.3. T, D and L are the cable tension, drag and lift respectively. V_C is the cross wind velocity, V_A the speed of the kite through the air, V_W is the free stream wind speed and V_L is the reel out speed of the line.

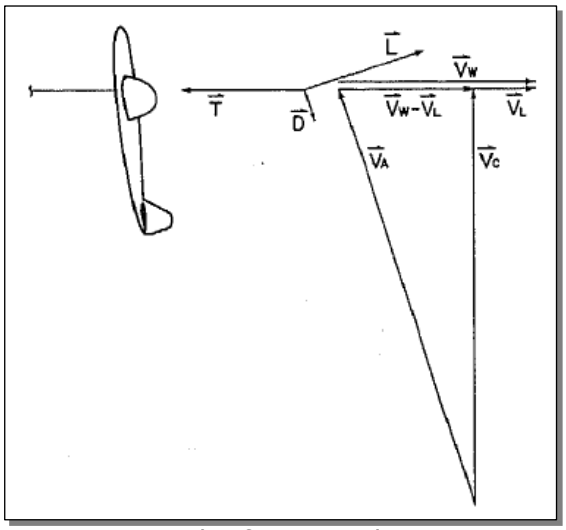

Figure 2.3: The forces and velocities of a kite flying cross wind. [17]

Loyd [17] showed that the maximum velocity that the kite can reach is:

$$V_A = (V_W - V_L) \cdot \left(\frac{L}{D}\right)_K \qquad (2.1)$$

Where $(L/D)_K$ is the lift-to-drag ratio (or glide ratio) of the kite. So the airspeed of the kite is proportional to the lift-to-drag ratio of the kite. It follows from equation 2.1 that the lift of the kite is given by:

$$L = C_L \frac{1}{2}\rho V_A^2 S = C_L \frac{1}{2}\rho (V_W - V_L)^2 \left(\frac{L}{D}\right)_K^2 S \qquad (2.2)$$

The line tension and the lift of the kite are approximately the same. This means that in the cross wind situation the force in the line is proportional to the square of the lift-to-drag ratio of the kite. Also the power output of a Laddermill is proportional to the lift-to-drag ratio of the kite system.

This shows that the lift-to-drag ratio is crucial for power production, and basically for any application of kites where the pulling force of the kite is very important.

3 Ram-air wings

This chapter is a basic introduction into ram-air wings. It explains what their basic working principles are and what kind of applications they are currently used for.

3.1 Definition of a ram-air wing

A ram-air wing is a hollow, soft fabric wing that takes its shape when it is inflated with high pressure air that is forced into the wing through openings at the stagnation point on the leading edge.

There is one point on a wing where the static air pressure is the highest and equal to the atmospheric pressure plus the dynamic pressure. This point is the stagnation point at the leading edge. When an opening is made at the stagnation point of a wing, which is made of a fabric that is almost impermeable to air, the wing will inflate when it moves through the air.

Once the wing is inflated there will be very little air flowing in and out of the wing as long as the stagnation point stays over the air intake and there is no leakage from other parts of the wing. The wing has taken its aerodynamic shape and it will work with the same aerodynamic principles as a rigid wing.

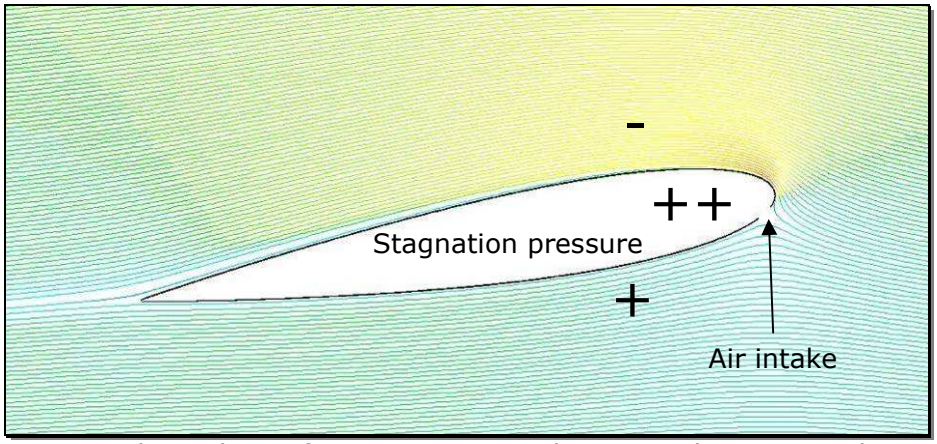

Figure 3.1: Principle working of a ram-air wing. The wing takes its aerodynamic shape because high pressure air from the leading edge stagnation point is forced into the wing.

The wing is kept in shape by ribs that connect the top surface of the wing to the bottom surface, as shown is figure 3.2. The space in between two ribs is called a cell. In the ribs are holes. The ribs of rigid wing aircraft also have holes. These serve the purpose of making the construction lighter and allowing control mechanisms to pass through the wing. In ram-air wings the holes serve the purpose of allowing air to pass through the wing in spanwise direction. These holes are called cross-ports. They improve the inflation and deflation characteristics. The amount cross-ports of is limited by the structural integrity of the wing.

In most applications the ram-air wing is supported by lines that are connected to the ribs on the under side of the wing. To reduce the amount of lines by which the wing is supported and thus to reduce the drag, some ribs are not externally supported by lines, but they are internally supported by diagonal cross bracings. These bracings can be in the form of ribs or tapes, called V-ribs or V-tapes respectively. The cross bracings also give the wing more rigidity.

Due to the internal over pressure the top and bottom surface will billow outwards in between the ribs. This is called ballooning. Because of the ballooning the shape of the cell centers is not the same as that of the ribs. Therefore, the aerodynamic shape of a ram-air wing is a compromise between the airfoil shape at the rib and the airfoil shape at the cell center.

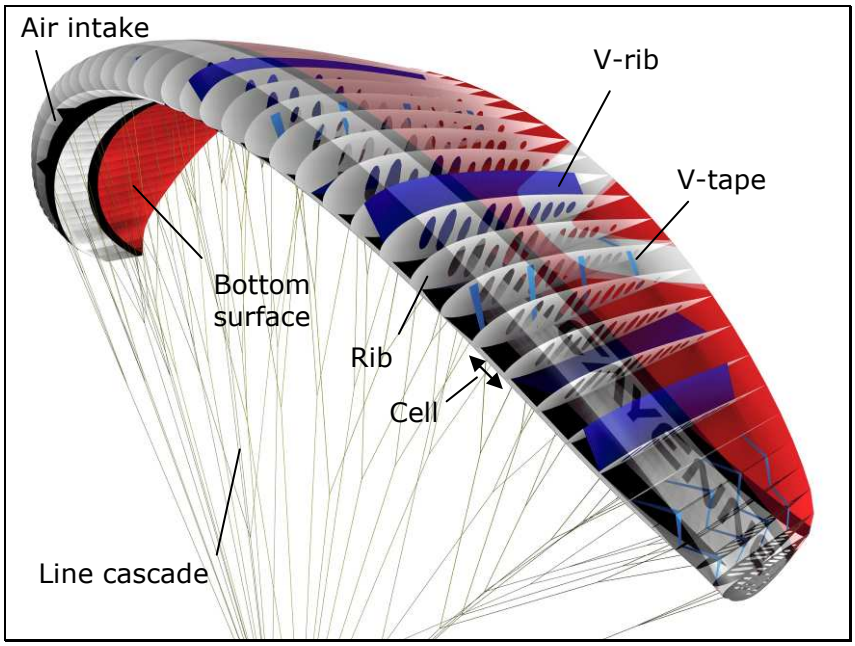

Figure 3.2: See through impression of the construction of a ram-air wing. [Source: Skywalk GmbH]

3.2 Applications of ram-air wings

Originally designed by Domina Jalbert in the 1950's the first ram-air wings or parafoils were parachutes. Since then there has been a continuous development of ram-air wings for a number of applications where a wing with low weight, low cost and small storage volume was required. More and more sophisticated designs led to wings with better handling. This made them more accessible to the masses. Because of their low cost and portability their main application is in air sports, but also other applications benefit from these advantages. Nowadays, these are the most common applications of ram-air wings on the market:

- Skydive canopy: The purpose of this ram-air wing is to decelerate the fall of the skydiver to a speed with which he can safely land and to allow him to fly a certain distance. The wing has a rectangular planform. It is primarily built to resist the shock of the opening and to open slowly and safely. During flight it has a wing profile that is very stable and difficult to collapse. The performance of the wing is quite low due to the thick suspension lines and special profile shape. The glide ratio or lift-to-drag ratio is in between 4 and 6.

[Source: flickr.com – qak4]

- Base jump canopy: Base jumping is related to skydiving. The main difference is that the jumper falls from an object instead of an airplane. This means that there is significantly less time for the parachute to open and the jumper has no reserve parachute. To increase the opening reliability the wing has much larger cell openings than a regular skydive canopy. This means that a base jump canopy has a worse aerodynamic performance than a skydive canopy. But for base jumping opening reliability is more important than aerodynamic performance. The glide ratio is on the order of 3 to 4.

[Source: flickr.com – Edward]

- Paraglider: Unlike the skydive canopy that is made for decelerating a fall a paraglider is made to allow a person to fly and use currents of rising air to gain height. Because of the low wing loading and efficient airfoils a paraglider can fly as slow as 6m/s and have minimun sink rate of around 1m/s. A downside of these characteristics is that a paraglider is prone to deflations when flying in turbulent air. The glide ratio is in between 8 and 11.

[Source: Skywalk GmbH]

- Speed rider: Speed riding is a spinoff from paragliding. These wings are around 2.5 times smaller than the ones used for paragliding and they are meant for high speed descents, of up to 20m/s, along steep mountain slopes. This is preferably done on skies to cope with the high take off and landing speeds. The airfoil is much more stable than that of a paraglider, making the wing much less likely to collapse. Unlike a skydive canopy they are not designed for opening at terminal velocity. Their glide ratio is on the order of 3-5.

[Source: Ozone]

- Land kite: A ram-air land kite is a so-called mattress kite that is used for dragging people or objects on land. Common applications are buggy kiting (the kite is used to pull a tricycle and the kiter) and snow kiting (the kite pulls a skier or snowboarder). The kite is mostly flow on 20-30m kite lines. Neglecting the drag of these kite lines the glide ratio of such kites is approximately between 8 and 12.

[Source: Peter Lynn]

- Surf kite: With the development of kitesurfing most surf kite designers developed tube kite (kites consisting of an inflated tube as leading edge and a single skin surface). However, two of them design ram-air surf kites. One makes kites that are supported by a whole cascade of lines, like a paraglider. The other manufacturer only supports the kite at its wing tips (shown in figure 2.2). The main difference with other ram-air wings is that these kites have a closed leading edge with only two or three air intakes. These air intakes have valves in them to prevent air leaking back out. The reason for the closed leading edge is that this allows the kite to float and not fill up with water when it lands in the water. The glide ratio of a surfkite is in between 5 and 8.

[Source: Flysurfer]

- Cargo parafoil: A cargo parafoil is designed for precision airdrops when the payload must be flow for a certain distance from the drop zone to the landing zone. The payload can weigh several thousand kilos. The glide ratio of a cargo parafoil is usually between 3 and 4.

[Source: Atair Aerospace]

- Shipping kite: The shipping kite is a recent development. It is a ram-air wing specifically designed to pull large cargo ships across the ocean. Controlability is key design requirement. The glide ratio of such a kite is in the order of 3 to 5.

[Source: Skysails]

- Wingsuit: The wingsuit is a rather exotic application of a ram-air wing. As can be seen on the photo the wingsuit has ram-air pockets in most parts of the suit to give it better aerodynamics. The air intakes are on the shoulders and between the legs. Dispite its low aspect ratio and poor aerodynamic shape a glide ratio of 2 to 3 can be obtained.

[Source: Phoenix-Fly]

Figure 3.3 shows the wing loading and glide ratio of the wings discussed above in the form of graphs. The minimum and maximum values of the wing loading are the values of how these wings are used in every day life. They are a good indicator of how fast a wing will fly as flight speed *V [m/s]* is related to wing loading by:

$$V = \sqrt{\frac{1}{C_L} \cdot \frac{2}{\rho} \cdot (\text{Wing Loading})} \qquad (3.1)$$

Where C_L is the lift coefficient, and ρ *[kg/m^3]* is the air density. Wing loading should be inserted in N/m^2.

The shown values are not necessarily the minimum and maximum values of what these wings can take. Especially the wings that need to be landed by a person on foot have an adequate safety margin and a low wing loading in order to have a reasonable landing speed. But in an application where no people are involved they can be loaded much higher. Some cargo parafoils are made out of old skydive canopies. But while a skydive canopy is only loaded to around 6 kg/m^2 the cargo parafoil is loaded to around 40 to 50 kg/m^2. Also the Laddermill currently uses a regular surf kite. But it is flown at a much higher loading than what is normally experienced in kite surfing.

The consequence is that the structural safety margins are reduced, which in principle doesn't have to be a problem because there are no people attached to the wing. A surf kite for example is designed to take approximately 5G. This means that the kite can take a load of in between 400 and 500kgf. The exact load is not known because there is no load certification for surf kites. Paragliders are certified to withstand 8 times the maximum load of the large size of a model. For most models this is around 1000kgf. Another consequence is that the material will wear out much faster. Mechanical stress is one of the major causes that reduce the life time of the cloth that is used in most ram-air wings.

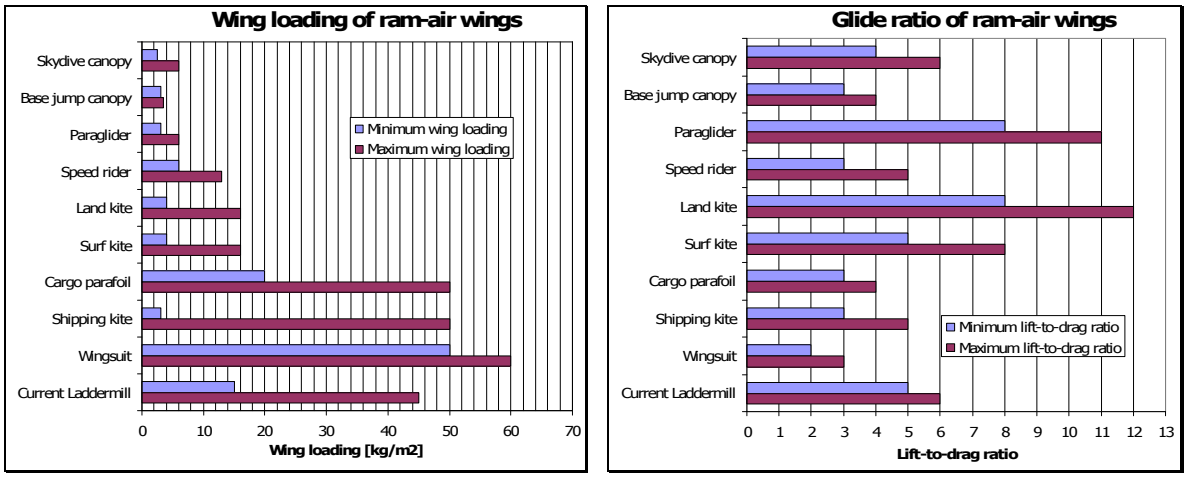

Figure 3.3: Estimated performance characteristics of different ram-air wings.

The right graph of figure 3.3 shows the minimum and maximum glide ratios of the different wings. The glide ratio is a measure of the speed that a wing theoretically can obtain when it is flown as a kite on a line (see equation 2.1). The high performace of paragliders comes from the strong competition drive in this sport and the fact that they only need to carry a person at a low wing loading. This means that their bridle lines can be very thin, which is good for drag reduction. High performance land kites can be designed very aggressively for high glide ratio because they don't have to carry a person safely and because crashing is not as much of an issue as is the case with kite surfing.

The reason that a surf kite is chosen for this project is because unlike paragliders it is made in a size that fits in the available windtunnels. And because the surf kite has a closed leading edge it will be easier to use for analysis than a land kite.

3.3 Design and simulation of ram-air wings

The design of most modern ram-air wings involves a large number of prototypes (sometimes more than 15 is possible). The reason is that the shape of the real wing is so much different from what is designed in the computer that many real life tests are needed to trim and fine-tune the wing to get the desired flight characteristics.

The difference between the computer model and the real wing comes from the fact that accurate calculation and simulation of the deformation of a ram-air wing is very difficult and requires a large amount of computing power. Ideally, a ram-air wing would be designed by means of fluid-structure interaction (FSI). This is a combination of finite-element analysis (FEA) of the fabric wing and computational fluid dynamics (CFD) analysis of the flow around and inside the wing. The reason that this approach is rarely taken is that such a simulation of a ram-air wing could take months or even years and would require a large computer cluster. This method is often too expensive and too time consuming for a ram-air wing manufacturer to employ.

The excepted method to design and build ram-air wings is to make a design in the computer that is based on a previous model. This design is built and test flown. It is trimmed and tuned to improve its characteristics. These changes are incorporated in the next prototype, which is also trimmed and tuned to further improve the flight characteristics. And so on until the design is good enough to put it on the market.

The approach taken in this project, with 3D measurement of the flying shape and fluid analysis of this shape in the computer, is a middle course in between FSI and the industry practise. The advance with respect to industry practise is that this method allows a more thorough analysis of the flying shape. This will make it more straighforward to change the flying shape into the desired shape. Compared to FSI this method is still a way of reverse engineering but the advantage of that is that it requires much less parallel computing than FSI.

4 Properties of a ballooned wing

The purpose of this part of this study is to give an introduction into how ballooning generally affects the aerodynamics of a wing with infinite span. At the same time this part of the study was used to determine the grid size and density for the CFD analysis of a full sized surf kite (this will be discussed in chapter 7). In this chapter it is explained how ballooning of the wing generally affects the flow and the resulting lift and drag.

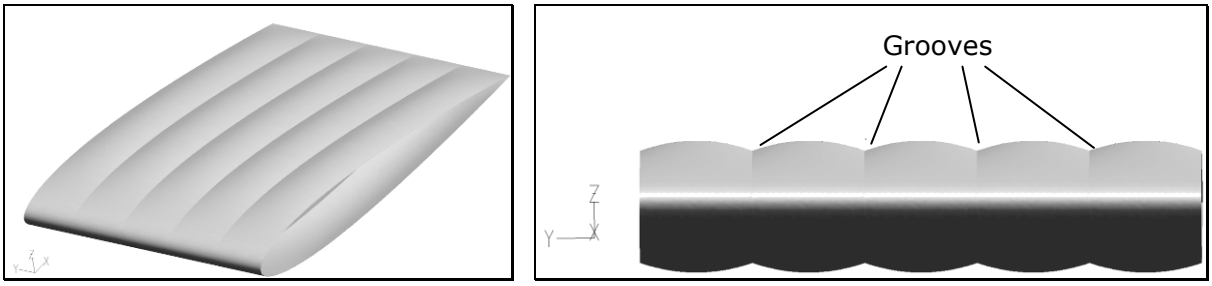

Figure 4.1: Grooves in the upper and lower surface due to ballooning of the wing.

When a ram-air wing is inflated the ribs will give the wing its aerodynamic shape. The space in between the ribs will billow out due to the internal overpressure (stagnation pressure) in the wing. At the cell centers the wing won't have the shape that was intended by the designer. Looking in spanwise direction the wing has bumps at the cell centers and grooves at the ribs, as depicted in figure 4.1. One may expect that this deformation will have a significant effect on the aerodynamic performance of the wing.

4.1 Geometry of the ballooned wing

The NACA0012 profile is choosen as a base line, since it is a well documented airfoil. The shape of the deformed cell center profile is taken form research by Babinsky [3] who measured the ballooning of a paraglider cell in the windtunnel. Figure 4.2 shows the thickness increase of the profile at the cell center.

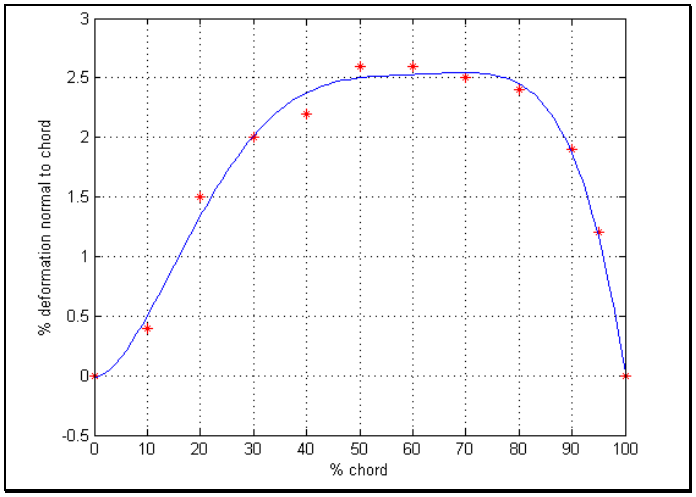

Figure 4.2: Dots show the measured deformation of a paraglider cell center [3]. The line shows the deformation that is superimposed on the NACA0012 airfoil.

This deformation is superimposed onto the NACA0012 profile to form the wing's cross section at the cell center, see figure 4.3. From Babinsky's research it could not be determined what the ratio between top and bottom ballooning is. It is assumed here that the thickness increase at the cell center is equal on the top and bottom surface. On a real wing there is more thickness increase at the bottom surface than at the top surface because more tension is built into the top surface to have a cleaner wing surface there.

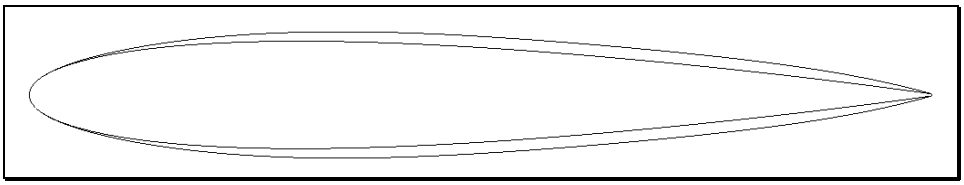

Figure 4.3: The NACA0012 profile (inner)
and the ballooned NACA0012 cell center profile (outer).

The spacing between the ribs is chosen at 12% of the chord length, giving a cell aspect ratio of 1 (the spacing of the ribs devided by the maximum thickness of the ribs). The wing surface is constructed with a smooth surface blend over the three cross sections, as show in Figure 4.1.

4.2 Computational Fluid Dynamics model

Computational Fluid Dynamics (CFD) is a method of solving the governing equations of fluid and gas flow, the Navier-Stokes equations, in a finite number of discrete volumes. For the basics of CFD the reader is referred to Appendix A and the Fluent user manual [28].

The first step in CFD is to create a volume around the wing geometry in which the fluid calculations are performed. This volume is discretized into small volumes that, in this case, have the shape of tetrahedra and prisms. This is the grid or mesh. An unstructured grid with prisms and tetrahedra is used because this allows easy and quick grid generation with good control over the grid density. Especially later when the whole kite will be analized with CFD the flexibility of an unstructured grid may be advantageous compared to a structured grid.

For turbulence modeling the k-ω SST model is used with transitional flow and enhanced wall treatment. Using Large Eddy Simulation or the Reynolds Stress Model is not considered because they are more computationally intensive than the k-ε and k-ω models. The reason that k-ε is not used is because these models are in principle designed for high reynolds number flow. This means that the model performs worse than the k-ω models near stagnation points and inside a boundary layer. The SST, or Shear Stress Transport, model is a combination of the standard k-ε model and the standard k-ω model. The k-ε model is used where the reynolds number is high. At places where the reynolds number is low the model is blended into the k-ω model. This gives the advantages of both models.

Enhanced wall treatment is used instead of wall function, because it is anticipated that there is premature flow separation on the ballooned wing. Wall functions predict separation far worse than enhanced wall treatment. Also, using enhanced wall treatment the grid resolution is much higher in the boundary layer. This allows a more detailed analysis of the flow. The price is more cells and more computation time.

The transitional flow option is enabled because it is advised in the Fluent user manual [28] to activate this option when using a high resolution boundary layer grid and enhanced wall treatment.

Wrinkles that normally occur in the fabric of a kite are not modeled. To model the small wrinkels an enormous amount of cells would be required to capture their shape accurately. Another option would be to model the wrinkles with a certain surface roughness, so-called "sand grain roughness". Using sand grain roughness requires the wall functions boundary layer treatment. As said before, this method performs worse at modeling separated flow.

At the inlet of the domain the flow enters with 3% turbulence intensity. This is such a high value because kites usually experience very turbulent flow because they fly low in the atmospheric boundary layer. The same value was also used by Miller [21]. The length scale is set to 5mm. For internal flows (flows inside a structure, for example a pipe) it is common practise to take the length scale as 7% of the diameter of the pipe which comes from Nikuradse's analysis of turbulence in pipes [27]. For external flows it is not unambiuous to find the right length scale. The length scale is the "*size of the large energy containing eddies in the flow"* [31]. According to Prandtl near a wall the length scale is on the order of 0.4 times the distance from the wall. Further away from the wall these eddies are on the order of the thickness of the boundary layer [27]. However to find a correct free stream value requires a thorough study of the specific flow case. The influence of this measure is mainly found in the development of turbulence in the flow. A large length scale decreases the damping and dissipation of turbulence and a small length scale increases the damping and dissipation of turbulence. This means that a too small length scale will immediately dissipate turbulence, causing an almost laminar flow.

Because there is no production of turbulence between the inlet and the wing but there is a certain dissipation, it is not straight forward to let sufficient turbulence reach the wing. Having a very large length scale to decrease the dissipation leads to unrealistic turbulence generation in the vicinity of the wing. Increasing the turbulence intensity at the inlet helps very little, because the higher the turbulence intensity the stronger the dissipation is.

As discussed by Menter [20] there is a maximum amount of k (turbulence intensity) and ω (specific dissipation rate) that can reach a certain distance from the inlet. The rest will just be dissipated by the flow, depending on the value of the length scale. Make the length scale too large and the flow will develop unrealistically high values of turbulence because too little turbulence is dissipated. In this case with the NACA0012 profile the effect on lift and drag is negligible but the turbulent structures in the flow can be significantly altered. The final value of 5mm is an intermediate value that causes neither excessive damping nor excessive growth of turbulence.

The problem remains that the turbulence that enters the inlet is mostly dissipated before it reaches the wing. To overcome this problem the flow domain is split in two. The first flow domain is the flow from the inlet up to a half chord length in front of the wing. This is still in front of the point where the presence of the wing starts to affect the turbulence intensity. The second flow domain is the rest of the flow. In the first part, so from the inlet up to a half chord in front of the wing, both k and ω are fixed.

Figures 4.4a, b and c illustrate the influence of the free stream turbulence intensity and length scale. The difference is in the different shades of blue in between the inlet on the left side and the leading edge of the airfoil. The color scale represents the turbulence intensity.

In figure 4.4a the turbulence intensity at the inlet is 10%. But because the length scale is only 0.5mm most of the turbulence is dissipated just behind the inlet. The turbulence intensity just in front of the wing is only 0.75%.

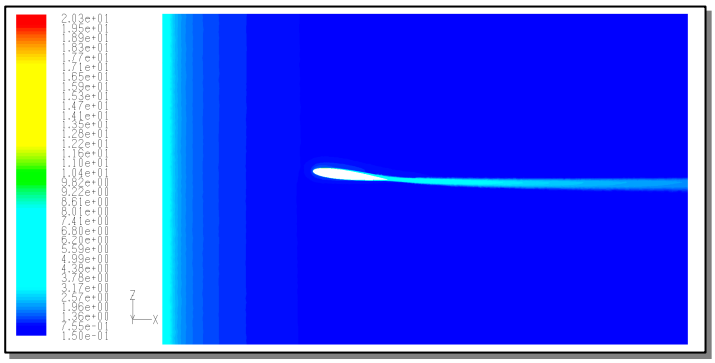

Figure 4.4a: 10% turbulence intensity, 0.5mm turbulence length scale.

In figure 4.4b the inlet turbulence is 3% and the length scale is 5mm. Because the length scale is 10 times larger the dissipation of turbulence is much lower and despite that the inlet turbulence is more than three times smaller than in figure 4.4a the turbulence intensity that reaches the wing is 1.5%.

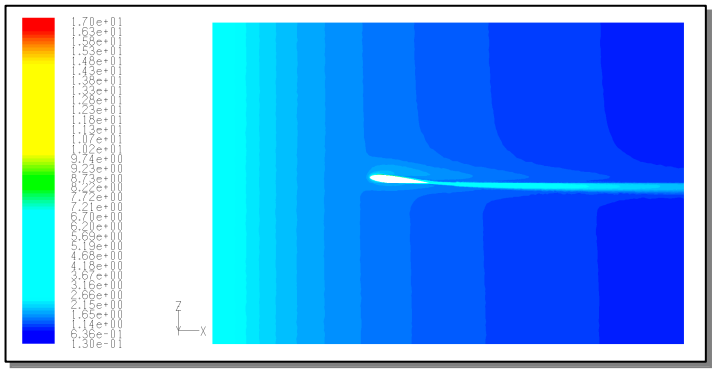

Figure 4.4b: 3% turbulence intensity, 5mm turbulence length scale.

Figure 4.4c shows that in the first part of the flow the turbulence parameters are fixed to an intensity of 3% and a length scale of 5mm. A half chord length in front of the wing the turbulence is released and 2.8% turbulence intensity actually reaches the wing.

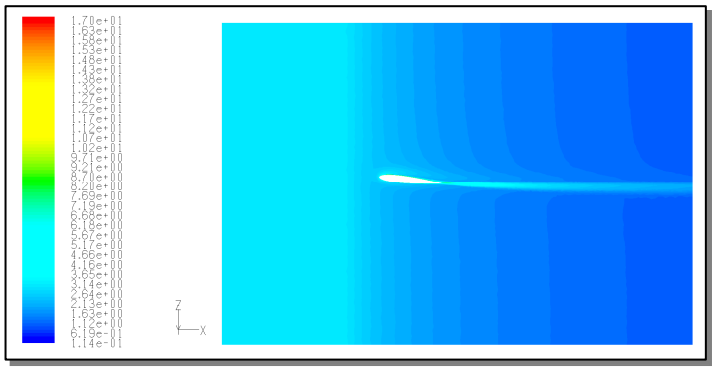

Figure 4.4c: 3% turbulence intensity, 5mm turbulence length scale, domain split in two at 0.5 chord length in front of the wing.

For the first 50 interations the discritization was put at first order and the pressure-velocity coupling at SIMPLE. The under-relaxation factors, which dampen the overshoot of the solution, of pressure, momentum, k and ω were put at 0.5. This led to a fast damping of the initial wiggles in the solution. After those 50 interations the solution was continued to 5000 interations with second order discritization, SIMPLEC and the under-relaxation factors at 0.7.

To understand the influence of the different parameters in Fluent, to get the right domain size without significant wall effects and the correct grid density to obtain a grid independent solution 32 different cases were run before starting with the actual analysis. The settings that resulted form these trail runs are listed in table 4.5.

Table 4.5: Settings of the NACA0012 CFD model.

Grid generator	ICEM CFD 11
Solver	Fluent 6.3
Gradient option	Node-based
Turbulence model	k-ω SST transitional flow
Wall treatment	Enhanced wall treatment
Numerical scheme	Second order upwind
Pressure	Second order
Pressure-Velocity coupling	Simplec
Chord length	1m
Span	12cm
Velocity	15m/s
Reynolds number	1.0 million
Surface cell size	16mm
Leading edge cell size	5.5mm
Trailing edge cell size	1mm
Total number of cells	~1.5 million
Number of prism layers	25
Initial cell height	0.065mm
Prism growth factor	1.2
Y^+ values	0-5
Inlet	Velocity inlet
Turbulence Intensity	3%
Length scale	5mm
Distance from wing to inlet	2.5 chord lengths
Outlet	Pressure outlet, gauge pressure = 0
Distance from wing to outlet	4 chord lengths
Roof and floor	Symmetry plane
Distance from wing to roof and floor	3 chord lengths
Side walls symmetric flow	Symmetry plane
Side walls asymmetric flow	Interface, pressure gradient = 0

With the settings from table 4.5 CFD grids were made around the NACA0012 profile at different angles of attack. For each angle of attack a different grid was made because the orientation of the wing is different with respect to the wake. Having a grid with a high enough resolution in the wake is very important. A too coarse grid in the wake can significantly alter the lift and drag values.

The angle of attack range for both the normal and ballooned wing consisted of 0, 3, 6, 8, 10, 11, 12, 13, 14, 15, 16 and 17 degrees angle of attack. Next to the analysis with head on flow each case was also run at 10 and 20 degrees side slip angle using a periodic flow boundary condition at the two side walls. Hence, in total a data set of 72 cases was made.

The simulation of side slip is significant because on a ballooned wing of finite span the flow is only aligned with the ribs at the center of the wing. The closer to the tip, the larger the angle between the local flow and the ribs is.

4.3 Lift and drag results of the CFD analysis

First, the influence of side slip on lift and drag is analysed. Figure 4.6 shows the polars of lift coefficient versus angle of attack for slip angles of 0, 10 and 20 degrees of the normal NACA0012 profile without ballooning. For reference additional curves are shown: X-foil low turbulence, X-foil high turbulence (3%), data from Abbot [1] and data form McCroskey [19].

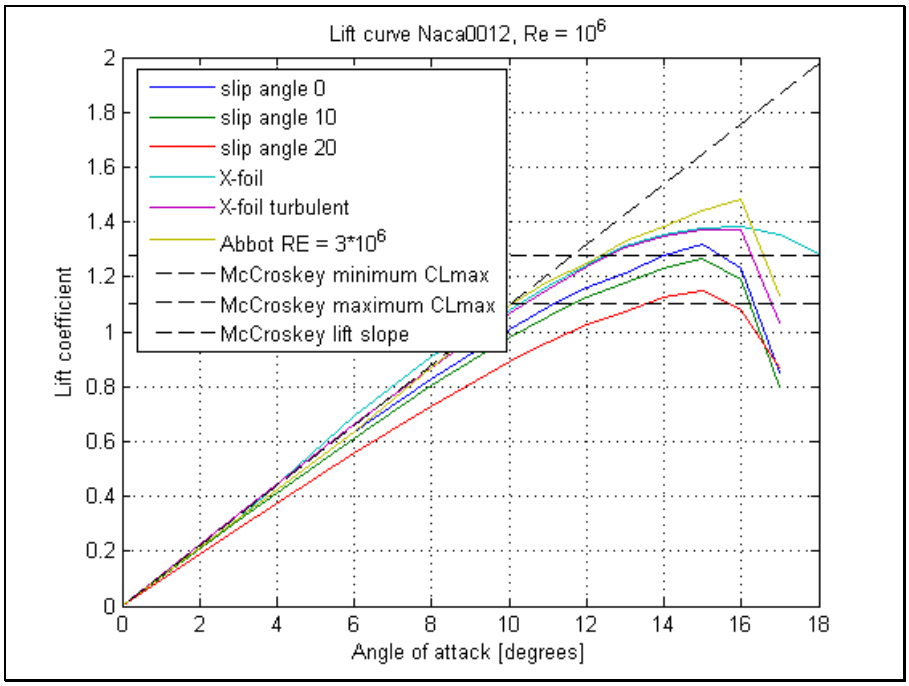

Figure 4.6: Lift coefficients of the Naca0012 profile (without ballooning) for 0, 10 and 20 degrees slip angle. All reference data are at 0 degrees slip angle.

The first thing to notice is the spread of the data. Clearly the different sources give different outcomes. This can be explained in the following way: according to a report by McCroskey (NASA) [19], who gathered windtunnel data about the NACA0012 profile from more than 40 windtunnels, there is a large spread in all of these data. The NACA0012 profile is very sensitive to Reynolds number and free stream turbulence. From that perspective it may have been better to choose a different profile for this part of the analysis, but then there would also be less reference data.

The difference between the fluent simulation and X-foil is likely to come from the various differences of the numerical models. First of all X-foil is a 2D simulation. In Fluent a quasi 3D simulation was used. That means that a slice of wing was simulated between two symmetry planes. The consequense is that also out of plane turbulence affects the flow. Furthermore, the way in which a turbulent boundary layer is treated is different. X-foil calculates with a transition point on the upper and lower surface. The Fluent flow is fully turbulent and is initialized with a certain free stream turbulence. The maximum lift coefficients of the two approaches differ by 6.5%.

The difference in maximum lift coefficient between the simulation and the data taken from Abbot [1] is easily explained by the fact that there is a strong dependence of the maximum lift coefficient of the NACA0012 profile on the Reynolds number, as shown in figure 4.7a.

McCroskey [19] shows that the range of maximum lift coefficient of the NACA0012 profile at a Reynolds number of 10^6 is approximatly from 1.1 to 1.28. From that perspective the 3D analysis is the closest. The lift slope, as shown in figure 4.7b, is 0.11 per degree. This is closer to the lift slope calculated with X-foil. It should be added that the data from McCroskey comes from various windtunnel tests and most windtunnels are designed to have as little free stream turbulence as possible.

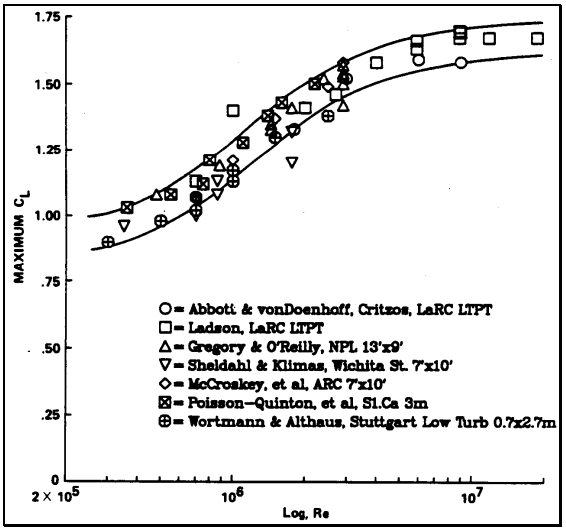

Figure 4.7a: Maximum C_L versus Reynolds number NACA0012. [19]

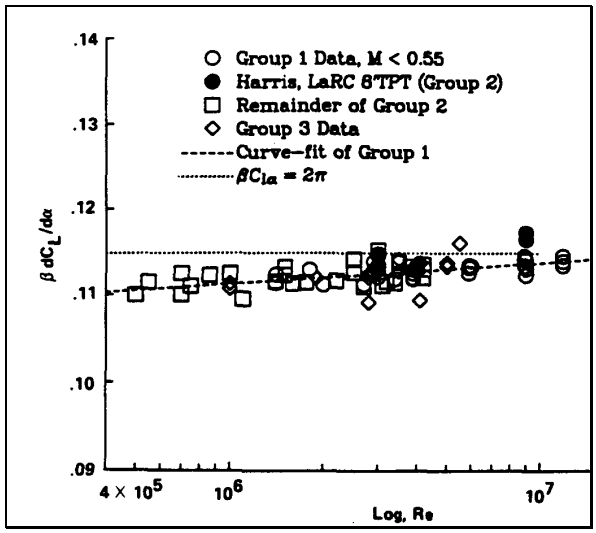

Figure 4.7b: Lift slope versus Reynolds number NACA0012. [19]

Now focussing on the different results for the different side slip angles it can be concluded that a larger side slip angle causes a shallower lift slope and a lower maximum lift coefficient. However, the stall angle remains approximately the same. It must be added, though, that an infinite wing at a certain side slip angle is the same as a wing with a certain sweep. Because of this effectively the chord length increases and the angle of attack decreases. However, for the graphs in this chapter the reference chord length and angle of attack where not corrected for the side slip angle. They are the same as for the head on flow.

Figure 4.8 shows the lift-drag polars of the NACA0012 profile. Again, the spread in the data is very clear. The drag rise in the 3D analysis is very different from the X-foil simulation. Up to $C_L = 0.4$ there is less than 5% difference with the turbulent X-foil simulation. But the higher the angle of attack the poorer the turbulence model predicts the drag. This is something that is commonly seen in CFD. Because of this the calculated drag can be as much as two or three times higher than the real drag. So for comparison with real drag the drag calculation is usually of little use. But for drag comparison between different numerical simulations it can be used to see trends of drag increase or decrease.

Looking at figure 4.8, one can see that the larger slip angles have a slightly higher drag rise above C_L = 0.8.

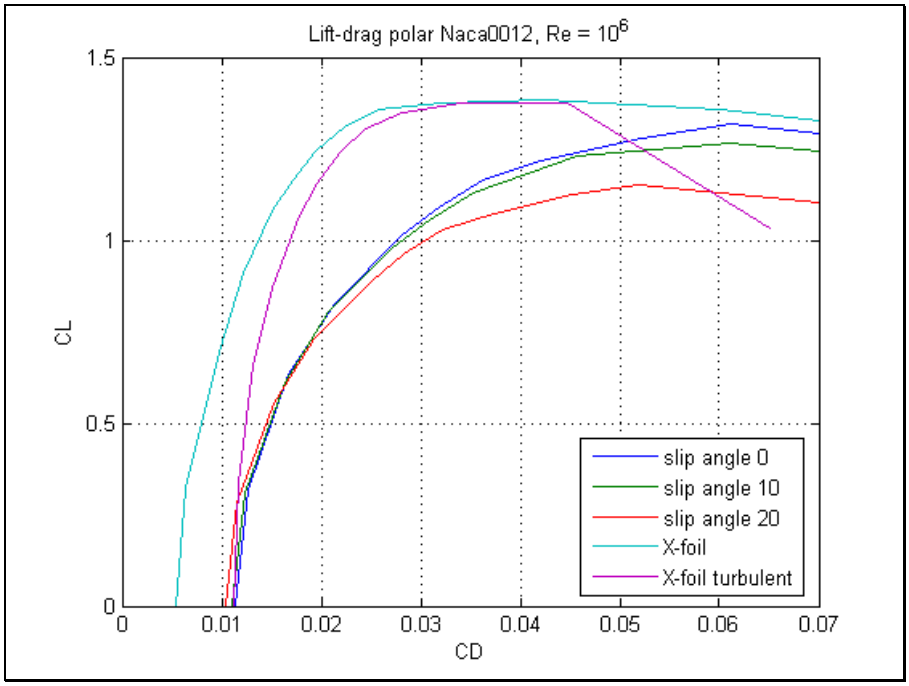

Figure 4.8: Lift-drag polars of the NACA0012 profile.

In figure 4.9 the lift coefficients of the normal NACA0012 profile and the quasi 2D ballooned NACA0012 wing are compared. The trends in this figure are that ballooning decreases the lift slope in al cases. In the cases of side slip the stall point is postponed and stall is more gradual.

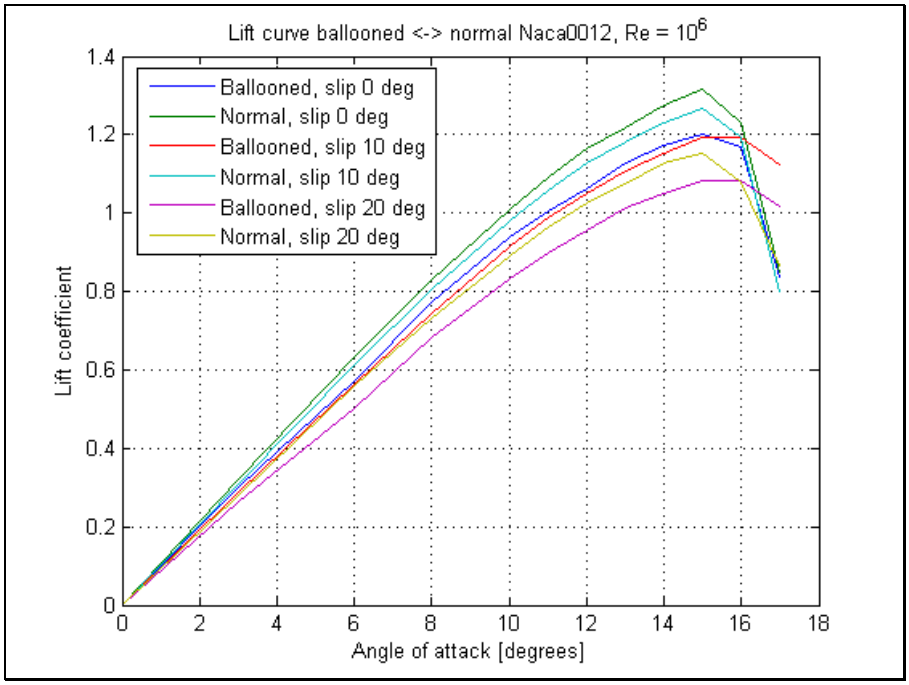

Figure 4.9: C_L comparison of the normal and ballooned NACA0012 wing.

Figure 4.10 shows a comparison of the lift-to-drag ratio (L/D) of the normal and the ballooned wing with head on flow. It shows that for the ballooned case the point maximum L/D is shifted to a higher angle of attack by about 1 degree and that the performance of the wing at lower angles of attack is lower than that of the normal wing. The maximum decrease is 13%.

When analysing the characteristics of both wings at a certain angle of attack the drag of the ballooned wing is higher below 7 degrees angle of attack and lower above 7 degrees angle of attack. This is because drag depends very much on the lift coefficient. At low lift the increased wetted area and increased thickness of the ballooned wing create more drag than the normal wing. At high angle of attack the extra drag due to lift becomes dominant over the zero-lift-drag. And because the ballooned wing produces less lift than the normal wing at a given angle of attack the drag is lower. When comparing the two wings at equal lift coefficients the drag of the ballooned wing is generally about 5 to 10% higher. The loss in L/D between 3 and 8 degrees angle of attack is primarily due to the loss of lift of the ballooned wing and not due to an increase in drag.
The drag polars are not shown here because the drag differences are small and therefore difficult to visualize.

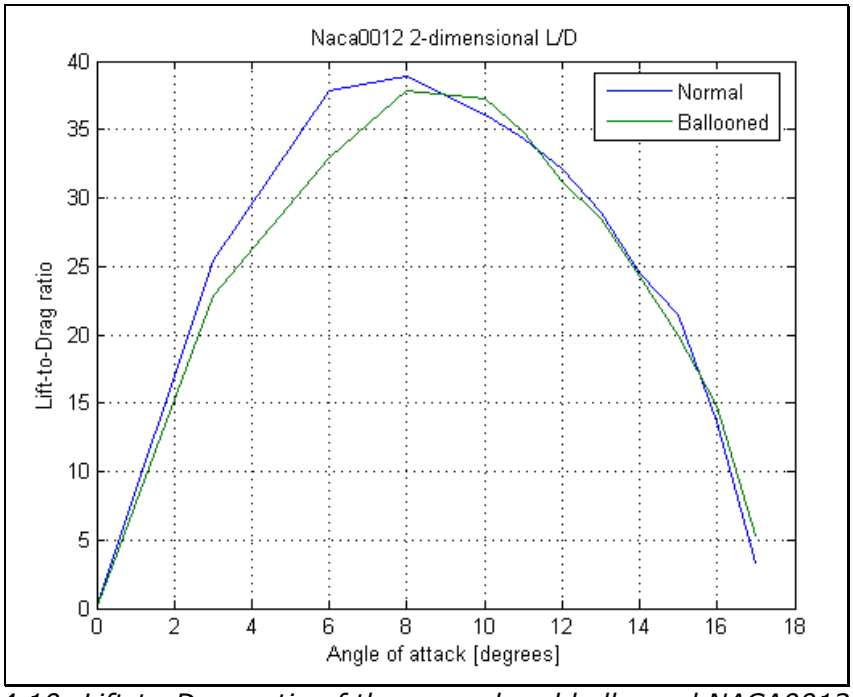

Figure 4.10: Lift-to-Drag ratio of the normal and ballooned NACA0012 wings.

4.4 Typical flow phenomena of a ballooned wing

In this paragraph some typical flow phenoma that occur around a ballooned wing will be shown. These phenomena are studied at an angle of attack of 12 degrees [5]. This is a normal angle of attack for a kite.

Figure 4.11 shows the pressure distribution on both wings. In this figure one can see that for the ballooned wing the under pressure peak on the nose is a bit lower and that on the lower surface there is less over pressure. The smaller pressure peak on the nose of the ballooned wing comes from the decreased curvature at the front of the wing.

The lower pressure on the underside at the back of the wing may come from the increased curvature there, because static pressure and airfoil curvature are strongly related. This extra curvature is not causing a pressure decrease on the upper surface because the flow is already separated at that point.

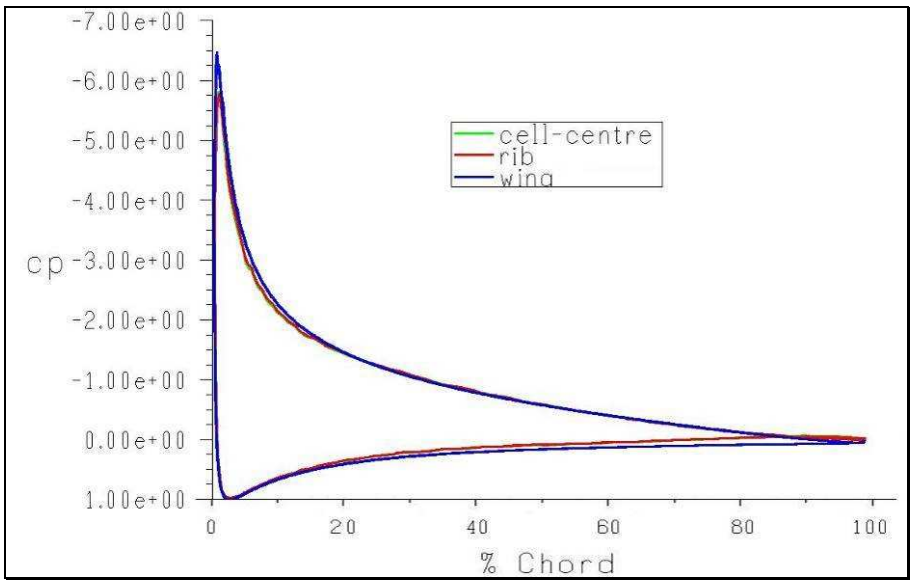

Figure 4.11: Pressure coefficients of the ballooned and normal wing (α = 12^o). "Cell-center" and "Rib" are from the ballooned wing (curves are difficult to distinguish because they are almost identical). "Wing" refers to the regular NACA0012 profile.

Another peculiar thing is that there is hardly any pressure difference between the rib and the cell center of the ballooned wing. Figure 4.12 shows a top view of both wings with the isobars ploted on them. It shows basically the same as figure 4.11 but now as pressure contours on the real geometry. One can see that there is very little spanwise deformation of the isobars on the ballooned wing except for the last 15% of the chord where unsteady flow separation affects the pressure distribution.

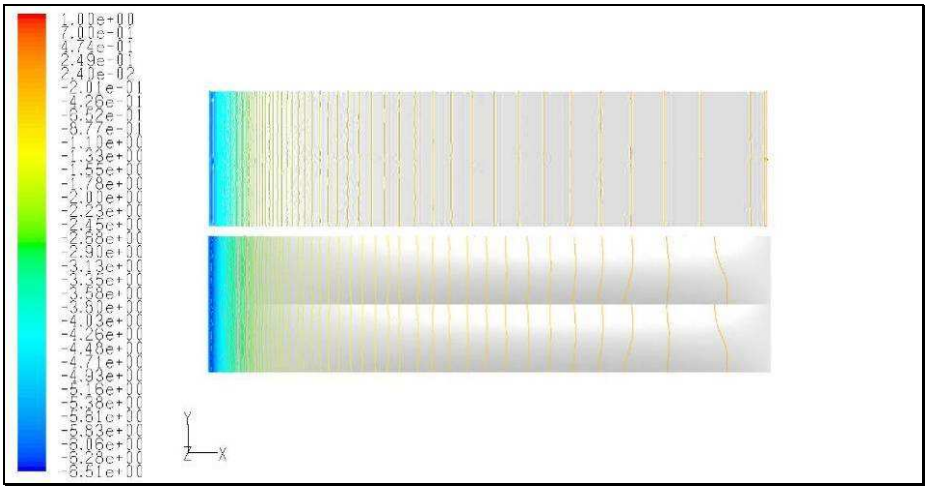

Figure 4.12: Top view of the normal NACA0012 wing (top) and ballooned wing (bottom). Shown are the isobars of static pressure coefficicient. Flow is in the positive X-direction, α = 12^o.

Dispite the fact that the pressure behaves almost as if the geometry were 2D the wake of the ballooned wing shows a clear 3D structure. This can be seen in figure 4.13. It shows an iso-surface of total pressure equal to ½ times the dynamic pressure. This means that on this iso-surface the flow has dissipated the energy of ½ times the dynamic pressure (remember pressure is equal to energy per unit volume).

Usually in CFD the shape of the wake is visualized by an iso-surface of total pressure = 0, which means an energy dissipation of one time the dynamic pressure. But for a 2D wing at a moderate angle of attack this doesn't show very much.

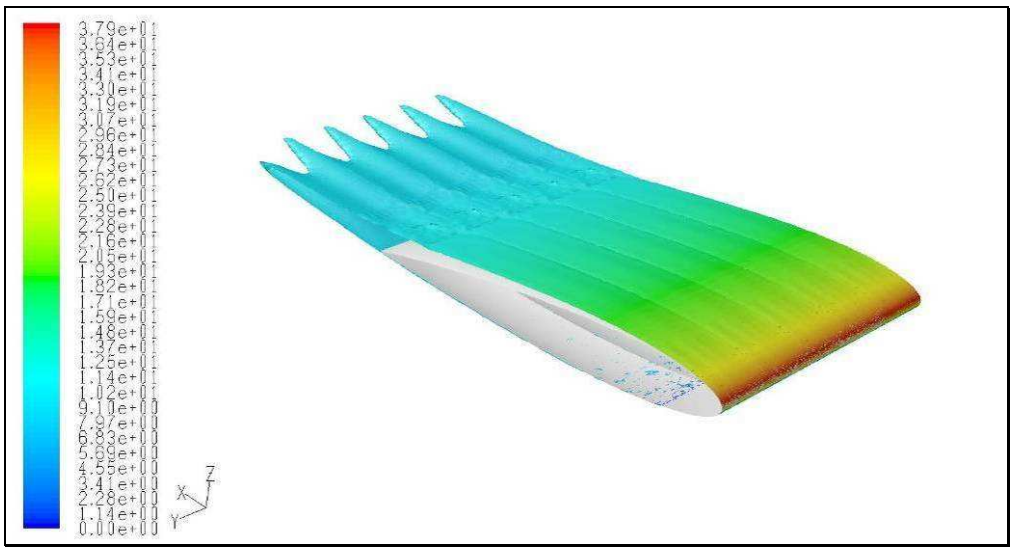

Figure 4.13: Iso-surface of the total pressure = ½ times the dynamic pressure. Colored by velocity magnitude [m/s], $\alpha = 12^o$.

In the grooves an increased amount of turbulence develops and more energy is dissipated then elsewhere. This may come from the interference of the adjacent cell surfaces. Note that the entire surface of the wing is smooth and has no wrinkles. Inside or under this surface more energy is dissipated. Outside the surface less energy is dissipated.

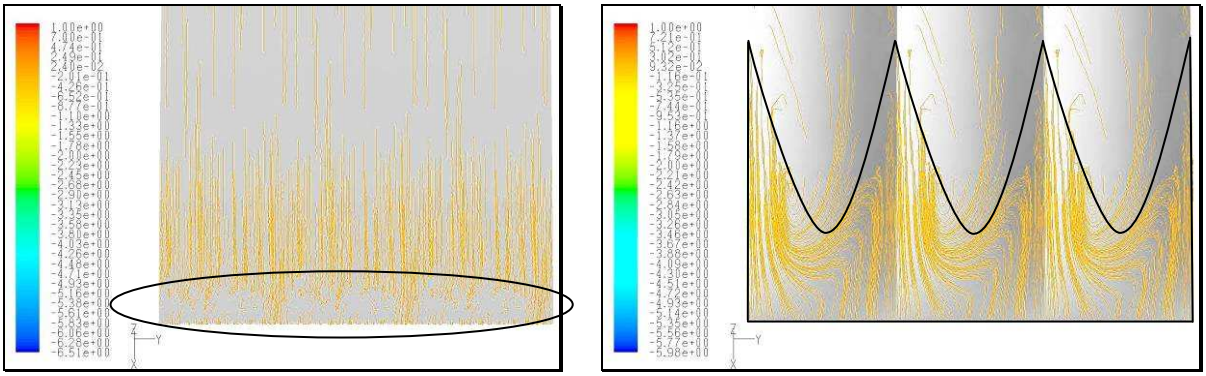

Figure 4.14: Trailing edge oil flow pattern. Left: normal NACA0012 wing with separated flow in the oval region. Right: ballooned NACA0012 wing with the separated region between the black lines. Width of one cell is 12% of the chord length. Colored by pressure coefficient, $\alpha = 12^o$.

Figure 4.14 shows the oil flow pattern (direction of surface shear stresses) near the trailing edge. Both show a chaotic pattern near the trailing edge that indicates separated flow. But for the ballooned wing this area is much larger. In the grooves the seperation is further upstream than in the centers. Note that at 12^o angle of attack the separation pattern on both wings is unsteady. What you see is a snapshot of the unsteady flow. That is why the patterns are asymmetric.

Windtunnel research by Babinsky [3] showed a similar outcome, see figure 4.15. Separation in the grooves of his wing was further forward though. This has most likely to do with the presense of the wrinkles in the cloth adjacent to the ribs of his model.

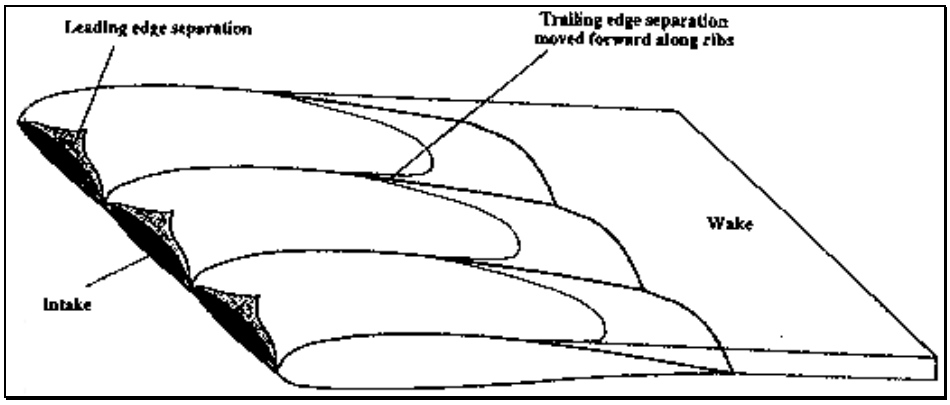

Figure 4.15: Separation pattern on a paraglider model [3].

The same oil flow analysis can be done when the flow is at a certain slip angle with respect to the model. The flow then shows a wavy pattern over the wing. This is shown in figure 4.16.

Apparently the flow right at the surface doesn't flow across the ribs. The flow is bent in the direction of the ribs. This happens until the flow fully separates near the trailing edge. At some point close to the trailing edge the flow component in the direction of the ribs completely disappears and flow is directed perpendicular to the ribs. The flow is fully seperated there.

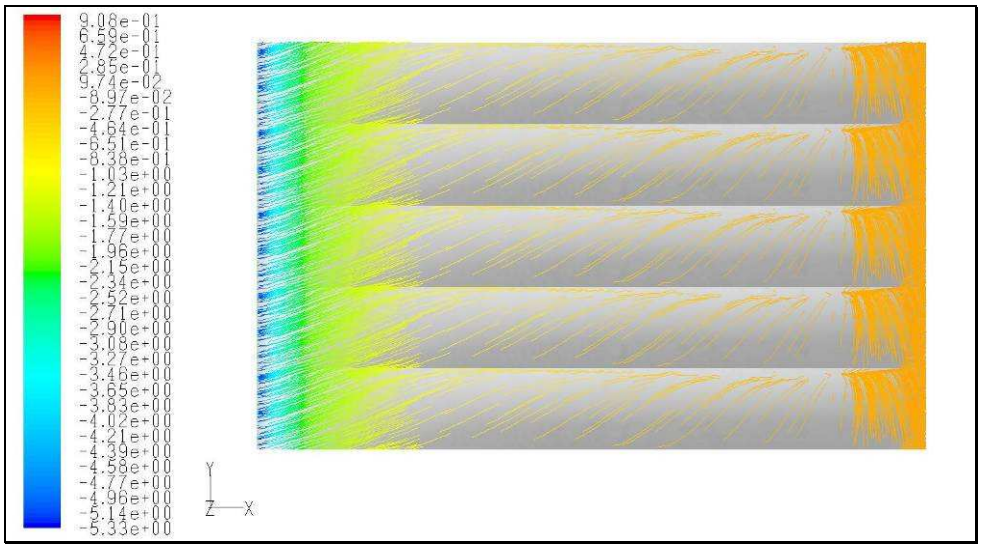

Figure 4.16: Oil flow patterns on the upper surface of the ballooned NACA0012 wing. Side slip angle 20°. Flow is in the positive X- and Y–direction. Colored by pressure coefficient, α = 12°.

Figure 4.17 shows why the flow direction changes when the flow tries to cross a rib. One can see that the isobars are very strongly bent over the width of each cell. This means that, looking in spanwise direction (Y-direction), the static pressure in the grooves is higher than at the cell center.

The reason for this is because to the flow the groove is nothing more than a region with a very strong concave shape. This shape slows the flow down. This gives rise to the pressure increase in the groove. The pressure gradient between the cell centers and the grooves bends the flow away from the grooves. Right at the grooves the flow that is closest to the surface even reverses in Y-direction, creating a very flat vortex that lies in the groove.

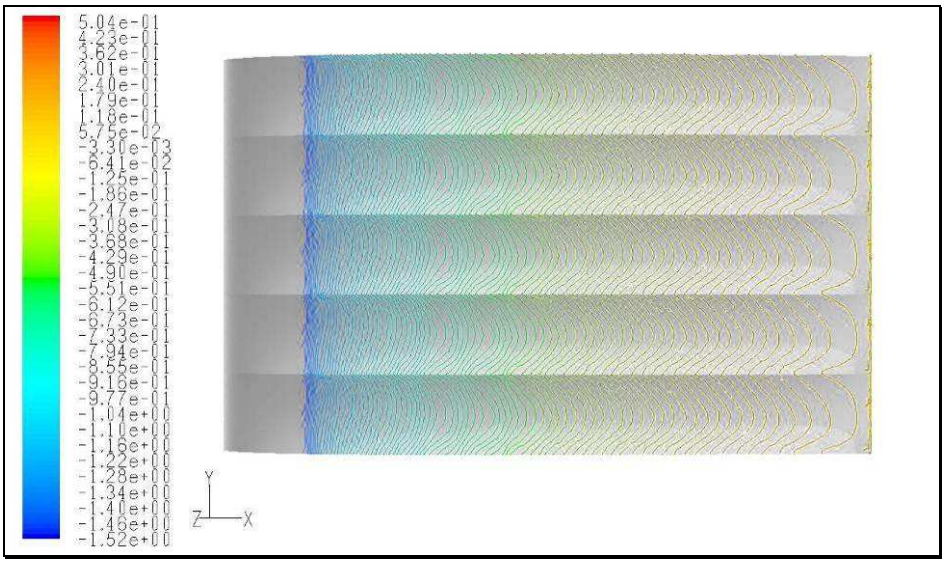

Figure 4.17: Contours of pressure coefficient.
NACA0012 ballooned wing. Side slip angle 20°, α = 12°.
For more detail the contours at the leading edge are left out.

Figure 4.18 is similar to figure 4.13. It shows the energy dissipation in the flow, but now for flow with a side slip angle of 20 degrees. There is clearly an increased dissipation in between the bumps indicating more turbulence there.

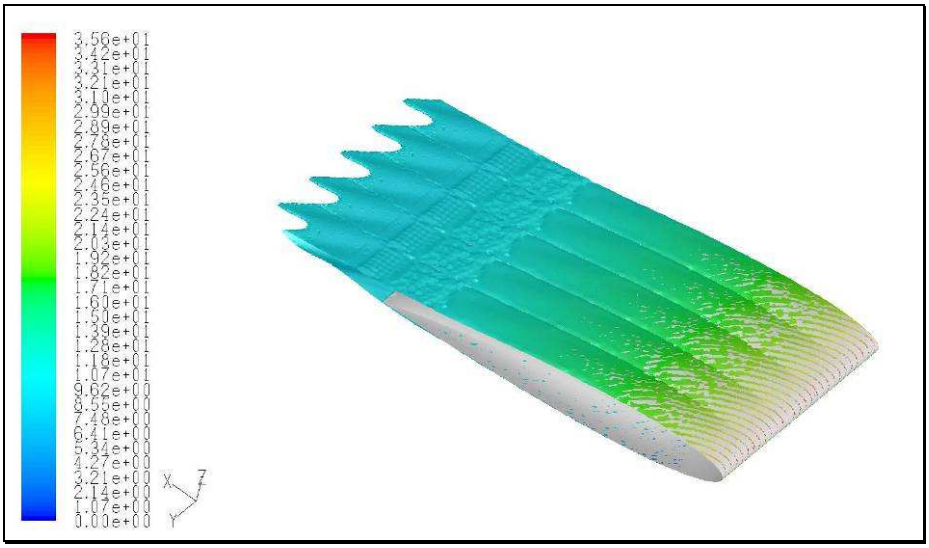

Figure 4.18: Iso-surface of the total pressure = ½ times the dynamic pressure.
Side slip angle 20°. Colored by velocity magnitude [m/s], α = 12°.

In figure 4.16 it was already shown that at the ribs the flow changes direction when the free stream moves at a certain side slip angle. Figure 4.19 shows that this effect extends a considerable distance above the wing. The freestream component in the Y-direction is 5.1m/s. Figure 4.19 shows an iso-surface of Y-component of the velocity of 5m/s. Clearly at the ribs the Y-velocity decreases and the iso-surface is further away from the wing surface. The total velocity magnitude is only affected a little bit by the ribs. So in a way the grooves in the wing act as fences. However, the spanwise force on the ballooned wing is not that much different from the normal wing. It is 26% larger but also the cross sectional area of the ballooned airfoil is 22% larger.

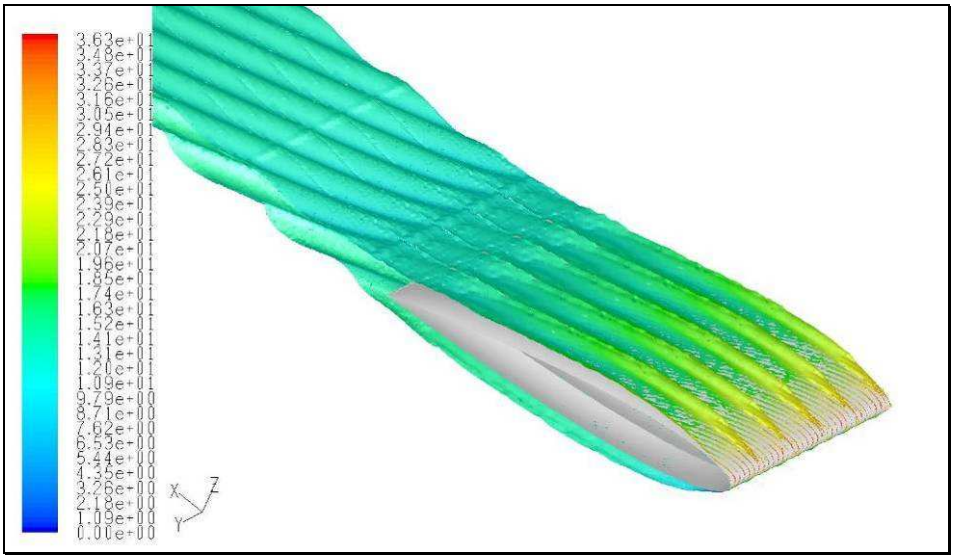

Figure 4.19: Iso-surface Y-velocity = 5 m/s. Side slip angle 20°, α = 12°. Colored by velocity magnitude [m/s].

4.5 Conclusion: Important properties of a ballooned wing

From the CFD analysis of the normal and ballooned NACA0012 wing it can be concluded that ballooning has the following influence on the wing:

- Ballooning reduces the maximum lift coefficient.
- Ballooning reduces the lift slope.
- Ballooning reduces the lift-to-drag ratio.
- Ballooning increases the drag at a given lift coefficient.
- Ballooning causes increased flow separation at the trailing edge.
- There is an increased turbulence production and energy dissipation in the grooves.
- When air flows at a certain side slip angle over the wing ballooning causes a more gradual stall behaviour.
- The grooves in a ballooned wing hinder the spanwise flow and act more or less like fences in case of sideslip.

5 Windtunnel tests

This chapter discusses the windtunnel tests that were performed with the ram-air wing. A Flysurfer Pulse2 ram-air kite was tested in two different windtunnels: the Böenwindkanal of the University of Stuttgart in Germany and the Large Low-speed Facility (LLF) of the German-Dutch Windtunnel Institute (DNW) in The Netherlands. The shape of the kite was measured using two techniques: laser scanning and photogrammetry.
In paragraph 5.4 the results of the load measurements are presented. The results from the laser scanning and photogrammetry have been put seperately in chapter 6.

5.1 Windtunnel test requisites

The purpose of this project is to understand how the ram-air wing deforms and how this influences the aerodynamics of the wing. The first step is then to measure the shape of the wing under controlled conditions. This requires a ram-air wing, a smooth flow of air and a way to measure the shape of the wing.

5.1.1 The ram-air wing

When doing tests on a soft fabric wing one runs into a dilemma straight away. The problem is that until now it has been impossible to scale a fabric wing and proportionally scale the mechanical properties of the fabric.

When a test involves only the aerodynamics of an object and not the structural deformation the object can be scaled. This is convenient because testing a small object in a small windtunnel is significantly cheaper and requires much less energy than testing a large object in a large windtunnel. As long as the Reynolds number and Mach number of the flow are the same the test object will have the same aerodynamic coefficients as the real model. Usually it is not possible to keep both numbers the same. But for low Mach number flows (below Mach = 0.3) the influence of the Mach number is small enough to neglect it and only the Reynolds number must be the same as in the real condition.

The Reynolds number is given by:

$$\mathrm{Re} = \frac{\rho V L}{\mu} \qquad (5.1)$$

where ρ is the air density [kg/m^3], V the freestream velocity [m/s], L is a reference length [m] (for aircraft the mean geometric chord) and μ the dynamic viscosity of air [Pa·s]. With little control over the density and viscosity of air it follows that when the model is half the real size the velocity in the windtunnel must be twice the real velocity.

Given that aerodynamic forces scale with square of the dimensions of the model and with the square of the velocity of the model it follows that the forces on the scale model are the same as on the real object. This is why in aircraft windtunnel testing the models are often made of solid steel.

This is of course not possible when one wants to measure the deformations of a kite. To scale down a fabric wing correctly for windtunnel testing proves impossible with the materials that are currently available. Because the forces on the model are the same as on the real wing a much stiffer and stronger fabric is required. The stitches in the wing must be closer to each other. On the real wing wrinkles will form in the cloth because due to the internal pressure the flat fabric is formed into a double curved surface. To keep these wrinkels in the same proportional size and shape the fabric must be much thinner.

So one needs a material that is much stronger, much stiffer and much thinner than nylon. If that material would be available the next issue would be to fabricate the scale model with the scaled production tollerances of the real wing. Attempts that have been made so far always resulted in wings that behaved very different from the real wing.

More often a section of a wing or quasi 2D model is used. In this way the chord length can be kept the same or close to the chord length of the real wing and the material properties don't need to be scaled. The disadvantage of these models is that the ballooning of a ram-air wing depends on the balance between the internal pressure inside the wing, the pressure distribution on the outside of the wing and the skin tension in the fabric. The skin tension depends on the layout of the bridle lines (the lines that support the wing), the spanwise camber of the wing, the lift distribution and the way in which the manufacturer chooses to distribute the skin tension. By changing the dimension of certain skin panels one can change the tension in the wing between the leading edge, middle section and trailing edge and between bottom surface and top surface. When a quasi 2D model is used it is very likely that the skin tension is affected and that the shape of the ballooning changes.

In other words: making a model of a ram-air wing always results in a different loading and a different construction of the wing and thus different deformations. For these reasons it was aimed for from the start of the project to test an off the shelf kite in a windtunnel without changing any dimensions of the real wing. Of course there are limitations to the size of the available windtunnels and there should be as much clearance with the windtunnel walls as possible to keep wall effects to a minimum. To reduce the the computational effort later on it was chosen not to model the internal flow in the kite. This would mean that the digital model should have a closed leading edge. The easiest way to model this is when the real kite also has a closed leading edge.

Therefore, the chosen kite is a Flysurfer Pulse2 6.0, shown in figure 5.1. The bridle lines are approximately 4.35m long. An important feature of Flysurfer kites is that they have special pantented single slotted flaps built into them, so-called Jet-Flaps. The influence and effectiveness of these flaps has already been investigated by Miller [21]. He found it very time consuming to get a good numerical simulation of the flap. For that reason and because the flaps are not the topic of investigation in this project the flaps are closed during the windtunnel test and in the numerical simulations.

Manufacturer	**Flysurfer**
Model	**Pulse2 6.0**
Manufacturer's specifications	
Area flat	6.0 m^2
Area projected	5.2 m^2
Aspect ratio	3.85
Root chord	1340mm
Cells	20
Mass	1.6 kg
Normal wind range	6.5 – 21 m/s

Figure 5.1: The Flysurfer Pulse2 6.0 kite [Source: Flysurfer]

The kite has two main lines that take most of the load and two brake lines to change the angle of attack and to steer the kite. The brakes don't just influence the trailing edge but via a pulley system all lines except the front lines change length in such a way that the ribs only change shape by a small amount.

5.1.2 The windtunnels

Two different windtunnels were used in this project. One was the Böenwindkanal (BWK) of the University of Stuttgart. The other one was the Large Low-speed Facility (LLF) of the German-Dutch Windtunnel Institute (DNW).

5.1.2.1 The Böenwindkanal (BWK)

The Böenwindkanal or Turbulent Windtunnel is a suction tunnel (the fan is behind the test section) that takes its air directly from the outside atmosphere. The test section diameter is 6.3m and it has a maximum velocity of 17m/s. It was built in the early 1980's to test small windturbines. It was built in particular to test the performance of small windturbines in very turbulent conditions. There were even special vanes installed in front of the test section to generate extra turbulence. Nowadays, the tunnel is used for a variety of objects, amongst other things: boats, sun screens, umbrellas, tents, cars and kites. To test these objects a flow with a much lower turbulence intensity is required than what the windtunnel was originally built for. To improve the air quality the turbulence vanes in front of the windtunnel have been removed and some changes were made to the wall and the inlet of the tunnel.

Figure 5.2: Aerial view [Source: Böenwindkanal] and front view of the Böenwindkanal.

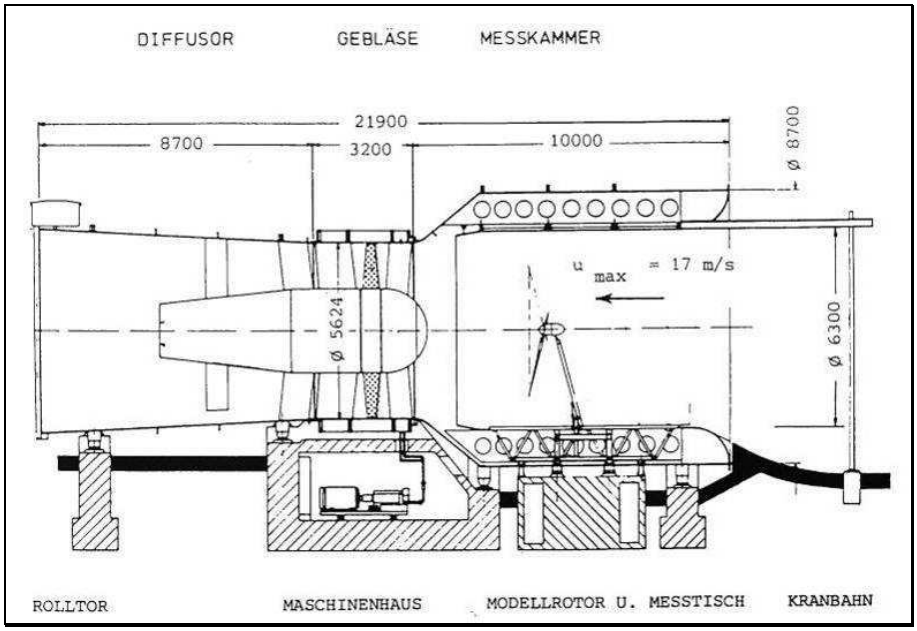

Figure 5.3: Cross-section and properties of the Böenwindkanal (dimensions in mm).

5.1.2.2 The Large Low-speed Facility (LLF)

The Large Low-speed Facility is the largest of the state of the art windtunnels that are operated by the German-Dutch Windtunnel Institute. It has three differently sized test sections: 6 x 6m, 8 x 6m and 9.5 x 9.5m. In the smallest test section speeds of up to 500km/h can be reached. The kite was tested in the 8 x 6m test section. The tunnel has a closed circuit that is around 400m in circumference. In front of the test section is a settling chamber with turbulence screens. These reduce the turbulence intensity to less than 0.1%. The LLF tunnel is mostly used to test large models of airplanes and helicopters and full size cars and trucks.

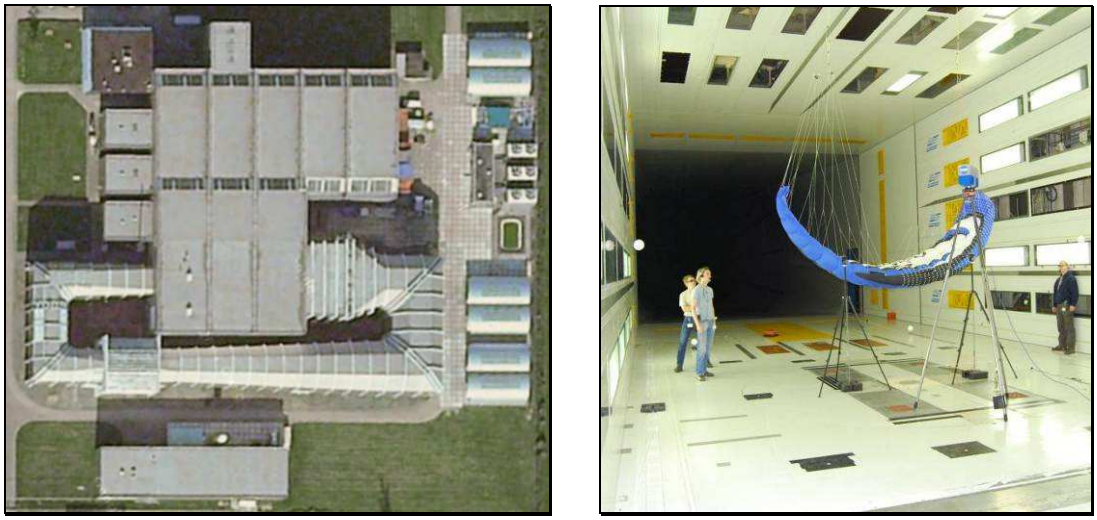

Figure 5.4: Top view of the LLF windtunnel [Source: Google Earth] and view of the 8 x 6m test section with the kite.

One can see in figure 5.4 that the kite is hanging upside down in the test section. The reason is that this makes testing significantly easier. First of all, when the windtunnel is turned on the kite is already in its flying position and it doesn't need to be launched anymore. A second reason is that the kite is held in place by two supports (see also paragraph 5.1.5). The position of these supports needs to be adjusted depending on the attitude of the kite. If the kite would fly normal side up these supports needed to be either very large, but that would also make them more flexible, or they needed to be mounted on the ceiling. That would make it almost impossible to adjust their position.

5.1.3 Shape measurement techniques

Two different measurement techniques were used: laser scanning and photogrammetry. These are common techniques to digitalize a 3D object, but they differ in working principles. Both techniques are briefly discussed in this paragraph.

5.1.3.1 Laser scanning

A laser scanner sends out laser light. A sensor receives the reflection and from this reflection the distance to the object and the position in 3D space can be determined. This can be done in a number of different ways:

- Time of flight: the scanner sends out a laser pulse in a predetermined direction. Then it measures how long it takes to receive the reflection of the pulse. It takes a laser pulse approximately 3.3 picoseconds to travel 1mm. In this way more than 10.000 coordinates per second can be registered.

- Triangulation: a laser and a camera have a fixed orientation with respect to one another. Depending on the distance between the laser and the object the reflection will appear on a different position on the sensor of the camera.
- Structured light: a laser projector and a camera have a fixed orientation with respect to one another. The projector projects a light pattern onto the object. This can for example be a grid consisting of horizontal and vertical lines. From the deformation of the grid the shape of the object is calculated.
- Phase difference: The scanner sends out continuous beams with different frequencies of light. From the phase differences of the outgoing and incoming bundles of light the distance to the object can be calculated. This method is faster than "time of flight" and over 100.000 coordinates per second can be registered.

In principle there are more laser scanning techniques, but these are the most common ones. In this project a phase difference laser scanner was used that was made available by the University's Department Earth Observation and Space systems. This scanner is a Faro Laser Scanner LS420.

Before the windtunnel experiments it was unsure how well the laser scanner would be able to capture the kite in the windtunnel. For this type of laser scanner to work accurately the object shouldn't move at all. But the kite is flexible by nature and can in principle move during a scan because a scan takes approximately one minute. For that reason there was no investment in another or better suitable scanner. The systematic error of the scanner is ±3mm at 20m. To see the kite from all sides it takes seven scans in total. These scans are linked together ("registered") using registration spheres.

Figure 5.5: The Faro LS420 laser scanner. [Source: Faro]

For more information about the particular scanner that was used the reader is referred to Appendix B.

5.1.3.2 Photogrammetry

With photogrammetry first a photo camera is calibrated using a special pattern to correct for lens and sensor distortions. Then photos are taken from different angles from the object. Using special software common points from the different photos are linked to each other. The result is a 3D model consisting of points, lines and camera positions.

The elegance of this technique lies in the fact that even with a simple, cheap digital camera one can get quite good results from a static object. For a moving object also good results can be obtained if either the object is in a rigid body motion (no internal deformations) or if multiple cameras are used that shoot synchronously with a sufficiently short shutter time.

Because there was a chance that the kite would not hang completely still in the windtunnel the key issues were the synchronization of the cameras and the shutter time. Not all cameras are suitable for synchronization. Cameras that can be synchronized as they come out of the box are usually the more expensive models. The shutter time depends on the amount of light in the windtunnel and the light sensitivity of the camera. After consulting professional photographer Max Dereta the Nikon D300 was chosen because D300 cameras can easily be synchronized and can shoot good quality pictures at ISO speeds of 1600 to 3200.

Photogrammetry requires that every point that should be captured in 3D must at least be seen by two, but preferably more cameras. After trails with a single camera it was concluded that to capture one wing half of the kite at least 14 cameras were required. It is thus assumed that the kite is symmetric about the center of the wing.

Figure 5.6: The 14 Nikon D300 cameras.

The fact that 14 cameras were required to capture the kite meant that extra time was was needed in the windtunnel to install and setup all the cameras. The BWK windtunnel was available for two weeks, but the LLF tunnel was only available for one day. At the same time the turbulence intensity in the BWK tunnel would much more than in the LLF tunnel which made it very likely that the kite would move too much to use the laser scanner in the BWK tunnel. Therefore, photogrammetry was the most suitable technique to use in the BWK tunnel and laser scanning was the most suitable technique to use in the LLF tunnel. The accuracy of photogrammetry depends on the constallation of the cameras, the number of markers, the placement accuracy of the markers and how well the object fills the images. Using the current setup the error was less than 3mm. For more information about photogrammetry the reader is referred to Appendix C.

The targets on the kite are regular 12mm round stationer's stickers. Because of the slippery coating of the kite's fabric the stickers don't stick to the kite. It was found that styrofoam glue (UHU por) works well to glue the stickers on. Each cell was covered with five rows of targets and around 200 targets per cell. The targets were spaced closer together in regions with a large surface curvature at the leading and trailing edge. In total the kite was covered with approximately 2000 targets as shown in figure 5.7.

Figure 5.7: It took 3½ days to glue the 2000 targets to the kite.

5.1.4 Load cells

Load cells that were used to measure the forces on the kite. These were two 300lbs (1325N) load cells (Transducer Techniques MLP-300), shown in figure 5.8. They were calibrated on a load bench.

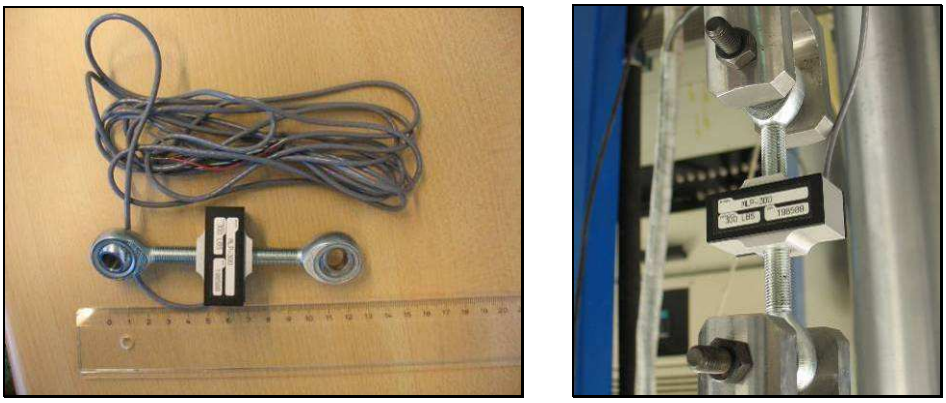

Figure 5.8: The load cells that were used to measure the forces on the kite were calibrated on a load bench.

5.1.5 Kite fixation

One of the major issues before the windtunnel tests was how to make sure that the kite would be hanging stable in the windtunnel. The problem is that except for a few exceptions all surf kites are unstable. This means that when a kiter doesn't touch the brake lines of the kite after a few seconds it will automatically steer towards the ground and crash. With a kite flying on 20 meter long lines this is normally not a problem because the kiter can intervene before the kite actually crashes. But when the kite is just flown on its bridle lines it will almost instantly go into a sort of dutch roll motion: a combined yawing and rolling motion. This motion gets very violent after a few oscillations and it makes it impossible to measure lift, drag and deformations. Because the purpose of the test was to measure deformations it was of paramount importance that the kite would hang still in its equilibrium position. The only suitable option is then to rigidly support the kite in this position. Tests on the beach showed that attaching two rigid supports to the attachment points of the front suspension lines gave the kite enough support to keep it in place. As long as the kite deviates little from its equilibrium point there will be very little force between the kite and the fixation and the fixation has little effect on the shape of the kite.

Figure 5.9: Testing the kite fixation on the beach.

The fixation was then adapted for use in the windtunnel. Two photo camera tripods were modified in such a way that they could be lashed to a line attachment point on the kite. The tripods were then lashed to the windtunnel floor to keep them in place, as shown in figure 5.10.

Positioning of the tripods followed a fixed scheme:

- Before the flow was turned on the tripods were placed such that the kite would have a 'reasonable' angle of attack
- The tunnel was brought up to speed
- The horizontal pointing rods were uncliped from the tripods and by feel the equilibrium point of the kite was determined
- The tripods were repositioned
- Again the rods were unclipped and it was double checked if the kite was in its equilibrium position
- Then from a distance, with everyone out of the vicinity of the kite it was checked if there were no unnatural wrinkles around the attachment points that would indicate a significant reaction force between the tripods and the kite (because the camera man was standing in front of the kite you can see these wrinkles in figure 5.10)

Figure 5.10: The fixation tripods lashed to the line attachment points.

The camera tripods had a three axis joint of which one axis was free to move and the other two were fixed. This allowed the lines of the kite to stretch in the vertical plane but the joint didn't allow the kite to move in the horizontal plane.

5.2 Windtunnel test Böenwindkanal (BWK)

In the BWK tunnel the shape of the kite was captured in different flight conditions using photogrammetry. Two load cells were used to measure the loads on the kite in each flight condition. Also the air data was registered: velocity, pressure, temperature and humidity.

In preparations for the test a CAD model was made of the windtunnel, see figure 5.11. This model was used to determine a correct position for the kite, the tripods and the 14 cameras.

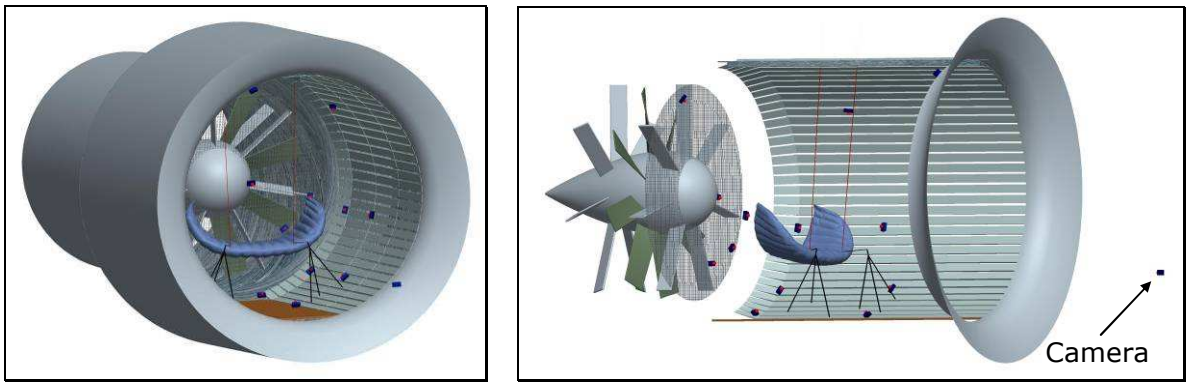

Figure 5.11: The CAD model of the Böenwindkanal with the kite, tripods and cameras.

Figure 5.12 shows the kite suspended in the windtunnel during one of the late evening tests. Testing in the evening when the winds and thermal activity outside were less usually gave the best results.

Figure 5.12: The kite suspended in the Böenwindkanal. [Source: Max Dereta]

Photos were taken from twelve different flight conditions, shown in tabel 5.13. However, it was not intended to process all the photos into digital models in this project since that would be too time consuming. Due to the closely spaced target, the complex 3D shape and a minimum amount of cameras the photogrammetry software is unable to reference the points automatically. This means that linking the photos together is time consuming handwork.

Unlike an airplane, a kite does not have one well defined angle of attack. As the brake lines of the kite are pulled or released the whole kite twists, the planform changes and even the airfoils may deform. Furthermore, the attitude and the angle of attack that the kite will fly at depends on its lift-to-drag ratio and the lift-to-drag ratio depends on the wing loading and hence on the dynamic pressure and the brake setting. The angle of attack depends on the lift-to-drag ratio because when the lift-to-drag ratio decreases the resultant aerodynamic force is pointing more in the direction of the free stream velocity. This pulls the kite further back with respect to the bridle points (the points where the bridle lines of the kite are attached to the windtunnel). The pitch angle of the kite increases and at the same time the angle of attack increases. For that reason, in this chapter, the attitude of the kite will be referred to with a certain brake line position. That is the distance that the brake lines of the kite are pulled or released with respect to the main lines. A pull on the brakes is taken as positive, a release of the brakes as negative and zero is taken as the position where the attachment point of the brakes is right next the the attachment point of the main lines. Table 5.13 shows the test scheme and the total aerodynamic force that was measured:

Table 5.13: Total aerodynamic force [N] ±3% vs. brake position and dynamic pressure.

		Dynamic pressure [Pa]		
Brake position [mm]		33.3 (~8m/s)	75.2 (~12m/s)	132.8 (~16m/s)
(min AoA)	-124	102	285	483
	-42	132	335	654
(max C_L)	39	163	410	719
	86	187	436	748

The reason that there are no nicely rounded numbers for dynamic pressure and brake position in table 5.13 is because measurements were taken over several days. On the first day the kite was tested at 8, 12 and 16m/s. These velocities gave the dynamic pressures as shown in table 5.13. Over the next days the air density changed a few percent and because the shape of the kite is very likely more dependent on the dynamic pressure than on the Reynolds number it was chosen to keep the dynamic pressure constant. For convenience, in the rest of the report the different test velocities will be referred as 8, 12 and 16m/s. Also some changes had to be made to the system that controlled the position of the brake lines. After those changes the kite was tested at the shown brake line positions.

During one series of tests the attitude of the kite was measured using a digital inclinometer. From the measured angles and loads lift and drag could be calculated. The average standard deviation of the attitude measurements was less than 0.4 degrees.

Also flow vizualization was used to gain a better understanding of the flow around the kite. Some pictures of the visualisation are shown in figure 5.13.

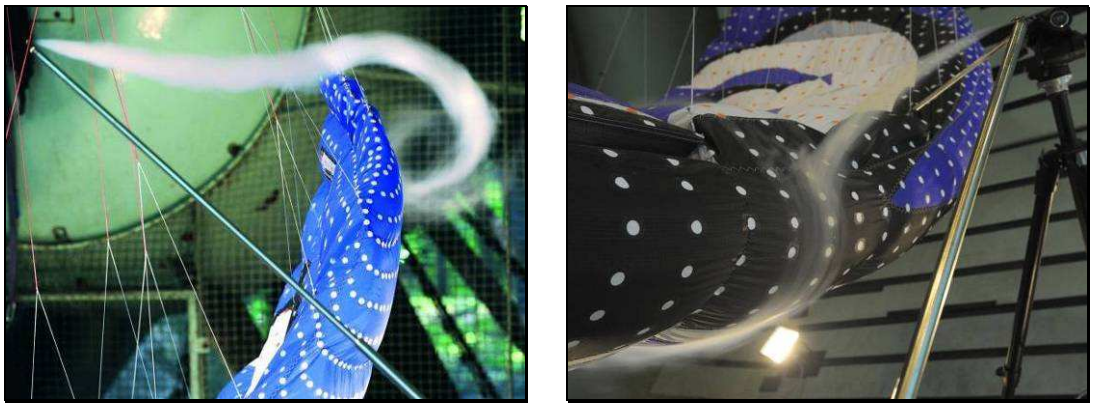

Figure 5.13: Flow visualization using smoke: the tip vortex and the stagnation point [Source: Max Dereta].

In total there were ten days of testing and in those days 101 test runs were made.

5.3 Windtunnel test Large Low-speed Facility (LLF)

The purpose of the tests in the LLF windtunnel was to use the laser scanner to scan the kite in different flight conditions. Per flight condition a total of seven scans was needed to capture the kite from all sides. During each scan the scanner made a complete 360° point cloud of its surroundings.

The LLF windtunnel is equiped with very sensitive air data instruments. These allowed that the dynamic pressure in the tunnel was regulated down to 0.1Pa. After each scan the scanner was moved to its new position. Then the test section was closed again and the dynamic pressure was regulated back to the desired value. Because of this a series of seven scans would take approximately one hour. In total four series of scans could be made that day.

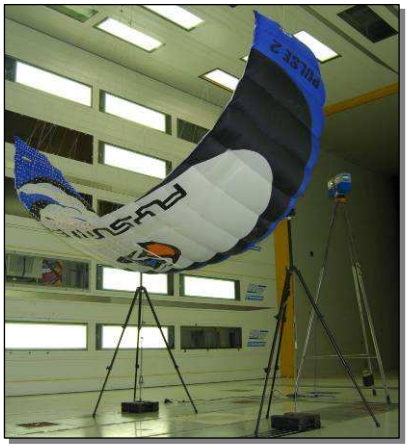

Figure 5.15: The kite in the LLF tunnel with the laser scanner on a tripod.

To get the right viewing angle in some positions the scanner had to be positioned within 1.5 to 2 meters from the kite. Especially with the scanner positioned on the floor there was a visible interference between the scanner and the kite. Mostly when the scanner was rotated about 45° with respect to the free stream the vortices shed by the scanner caused the kite to vibrate. This also happened when the scanner was on the floor down stream of the kite. Because every motion of the kite is directly translated into scan noise this can increase the noise from a few millimeters to a few centimeters.

Each scan consisted of approximately 5.6 million points. When all scans were then combined in the post-processing a point cloud was generated of almost 40 million points. Figure 5.16 shows to raw scans as they are transferred from the scanner to the laptop.

Figure 5.16: Raw laser scans. The black circle on the windtunnel floor is the 'shadow' below the laser scanner. Behind the kite you can also see the 'shadow' of the kite.

5.4 Aerodynamic performance of the kite

From load measurements (as shown in table 5.13) and attitude measurements the lift and drag of the kite were calculated. Table 5.13 gives the measured total aerodynamic force. Using the inclinometer data the total aerodynamic force is decomposed into lift and drag. Using the air data to calculate the air density and the photogrammetry data to calculate the projected wing area (the wing area projected onto the horizontal plane that is parallel with the free stream velocity) the lift and drag coefficients were calculated. Figure 5.17 shows the lift polar as a function of brake position (as described is paragraph 5.2) and lift-drag polars for the three different velocities.

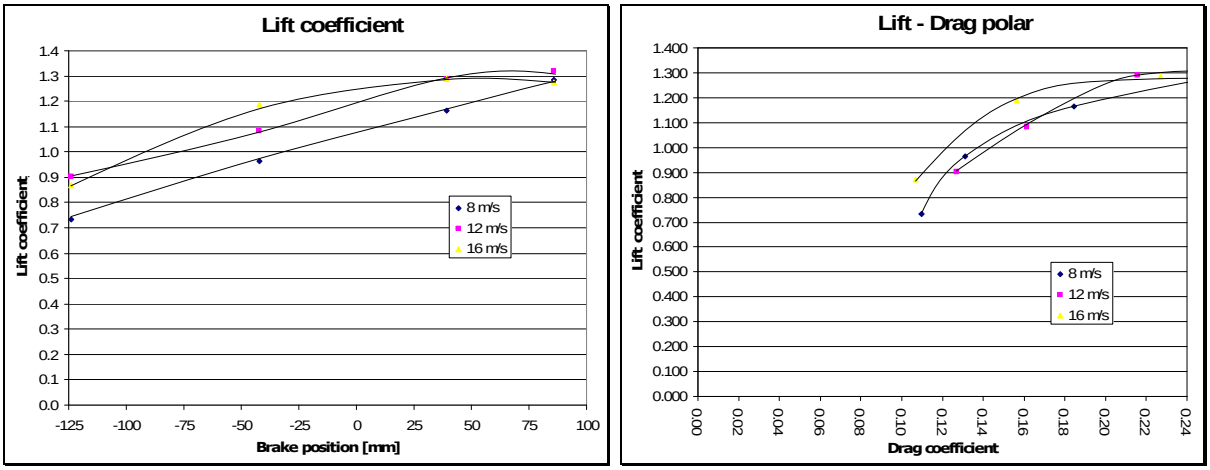

Figure 5.17: Lift coefficients of the kite as a function of brake position.

The first thing to notice is the high lift coefficients that the kite operates at. At a brake position of -125mm the brake lines are already competely slack. Figure 5.18 shows that in this situation large dents appear in the nose of the kite. Clearly the kite is designed to fly at a higher angle of attack. When the brake lines are released very far the angle of attack is decreased so far that the leading edge stagnation point moves above (in figure 5.18 below) the air intakes. The pressure inside the wing then becomes lower than the stagnation pressure and the wing dents inwards at the leading edge stagnation point. Dispite these very large dents the kite obtains its best L/D with this shape at 12 and 16m/s, as shown in figure 5.19. Apparently the production of lift beyond $C_L \approx 1$ degrades the L/D more than the deformation of the nose at lower C_L.

Figure 5.18: Dents appear in the leading edge when the angle of attack becomes small.

The fact that at 8m/s the kite doesn't reach its best L/D at the lowest brake setting is likely due to the fact that at this low velocity the kite has such a low wing loading that the kite is hardly flying. Because of this the kite doesn't get the shape that produces the highest L/D. Intially in the test program some tests were made with the kite flying at 5m/s. The tension in the fabric is then so low that the wing doesn't behave like a solid wing but it is constantly deforming.

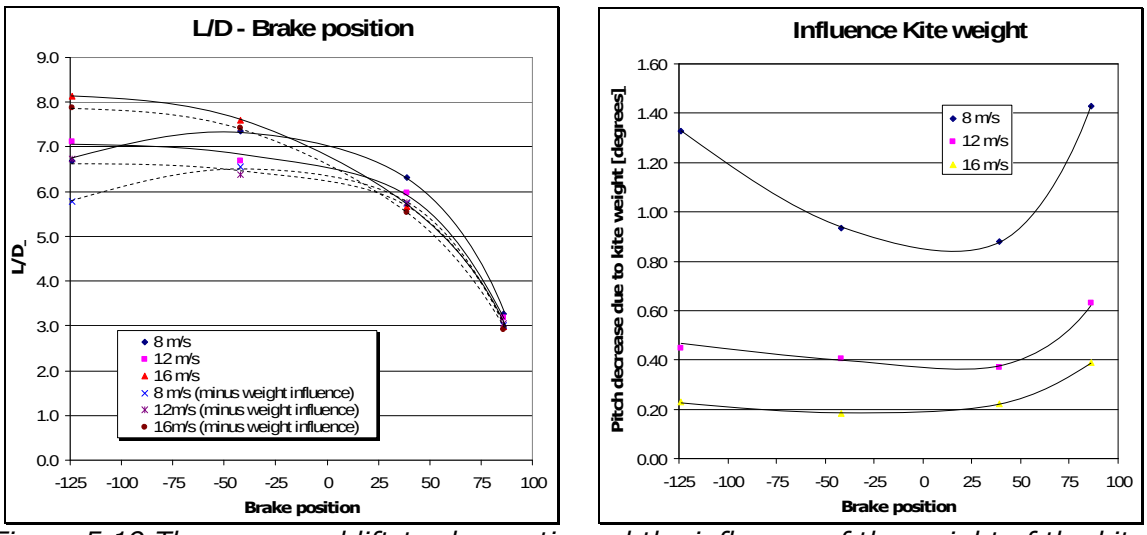

Figure 5.19 The measured lift-to-drag ratio and the influence of the weight of the kite.

The choise to hang the kite upside down makes testing much easier and more practical. But this has also an influence on the results, especially the L/D. The kite weighs around 16N. Before each test the load cells are zeroed so there is no direct effect on the load cells. However, this weight wants to center itself directly under the suspension point of the kite. In other words: the kite is rotated a bit forward to a position with a lower pitch angle and a lower angle of attack. So compared to the case where the kite would be hanging normal side up the kite has a better L/D, a lower lift and a lower drag in the upside down situation. Estimating the change in lift and drag is very difficult because the rotation of the kite is a pure rotation and that is not the same as the rotation of the kite that is caused by pulling the brakes. In that case the whole wing twists and warps. What is shown in figure 5.19 is the L/D that the kite would have given that the lift and drag would be the same, but the weight of the kite is subtracted from the equilibrium.

This is done in the following way (see figure 5.20). When you approach the problem in reverse order you see that if the kite would have no weight the load cells and inclinometer would just measure the magnitude and direction of the resultant aerodynamic force R_a. When the kite has a certain weight W, W is vectorially added to R_a. The effect of zeroing the load cells before the test is subtracting the magnitude of W from the vectorial sum of R_a and W. The resulting vector F is what the load cells and inclinometer measure in the windtunnel. By adding $\Delta\theta$ for each flight condition to the inclinometer measurements the measured L/D can be corrected to a situation where the kite would have no weight. In real flight however, gravity can point in almost any direction with respect to the flight vector. Figure 5.19 shows that the influence of the weight of the kite is the most when the kite is lightly loaded (low free stream velocity and low angle of attack) and when the kite is at a very high pitch angle (close to stall). The maximum difference is one point in L/D at the lowest velocity and lowest brake position. Because this is still not the L/D that the kite would have when it flies normal side up the comparison shown in figure 5.21 is based on the measured data and not the corrected data.

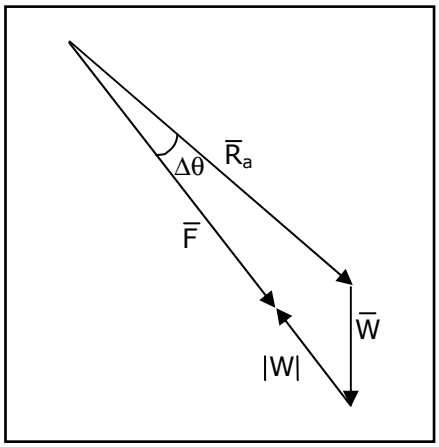

Figure 5.20: Calculating the influence of the weight of the kite on the L/D.

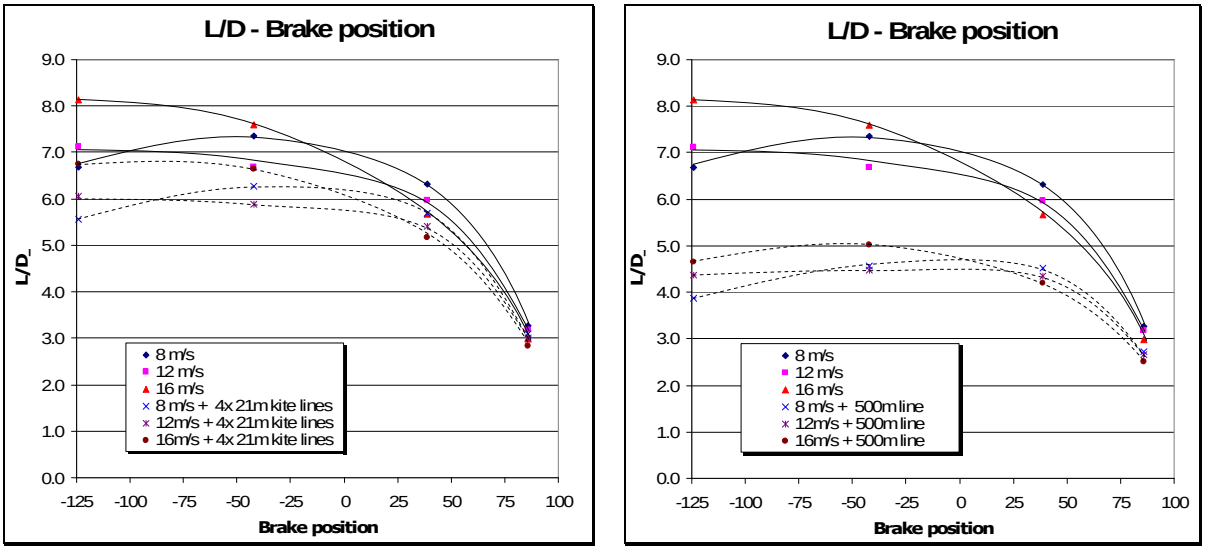

Figure 5.21: The influence of adding extra line the kite on the lift-to-drag ratio.

When extra length of line is added to the kite to fly it outside the windtunnel this adds drag. The consequence is that the whole L/D polar shift and that the optimum L/D moves to a different brake position. When this kite is used by a kite surfer it is flown with four lengths of 21m line. The two main lines have a thickness of 1.5mm and the two brake lines have a thickeness of 1.25mm. The lines are assumed to have a drag coefficient of 1 based on Hoerner [11]. Furthermore it is assumed, as is quite common in kite surfing, that the kite and the lines move together throught the air as one. So the kite is not pivoting around the kiter. One can see that the L/D of the system reduces by around one point when the brakes are released and the further the brakes are pulled, the larger the drag of the kite and the less significant the drag of the lines is. The point of best L/D shifts to a higher brake position (the brakes should be pulled more to attain the best L/D).

A realistic scenario for the Laddermill would be that the kite is flown on a single line of 500m length and 2.5mm thickness. The kite pivots around a fixed point on the ground, which gives a linear distribition of the velocity that the line experiences along its length. This reduces the L/D by two to three points for released brakes. The point of best L/D, which is most interesting for power production, shifts significantly to the right. For the speed of 8 and 12m/s the optimum L/D lies almost at the brake position that corresponds to the maximum lift coefficient (see also figure 5.17). This means that as more and more line is added between the kite and the ground it becomes more beneficial to pull the brakes very far and not fly the kite at its own best L/D. Eventually a high maximum lift coefficient becomes more important than a high L/D of the kite. The trade off is then to fly the kite with a high L/D at low altitude where windspeeds are also lower or fly the kite with low L/D at high altitude where the windspeeds are also higher.

A way around this problem is called 'dancing kites' (see figure 5.22) [8]. The idea is to have two kites fly on a single line. The kites fly a pattern by which they don't collide with one another and the point where they connect to the main line is almost static. In this way you can reach high altitudes without the drag of the main line slowing the kites down.

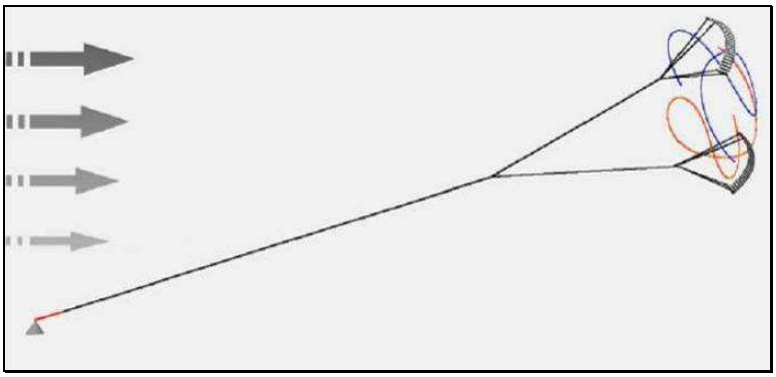

Figure 5.22: The concept of 'dancing kites' [8].

5.5 Thermography

A high quality infra-red camera (Thermo Tracer TH 7102, NEC San-ei Instruments Ltd.) was used in the BWK windtunnel in Stuttgart for thermographic analysis of the boundary layer development on the kite. This technique is based on the principle that due to increased turbulent mixing a turbulent boundary layer will draw more heat from the surface of a hot object than a laminar boundary layer. Thermography is normally applied in a way that the steel windtunnel model is heated up a few degrees. When the windtunnel is turned on hot zones, indicating laminar flow, and cold zones, indicating turbulent flow, appear on the thermal image. In theory this technique can also work on the kite if it is heated up form the inside.

The heat capacity of the nylon fabric and the air inside the kite is very small. For that reason the kite needed a continuous supply of heat, in this case a hair dryer. It was found that the best way to heat up the kite was to put the hair dryer inside the kite and let it recirculate its own warm air at the lowest power setting. Dispite the cross ports in the ribs the heat was very well contained in the single cell with the hairdryer. But to achieve this all possible air leaks that could cause a cross flow through the kite (the over-pressure valves, the tip drains and one of the two air intakes) were closed with tape.

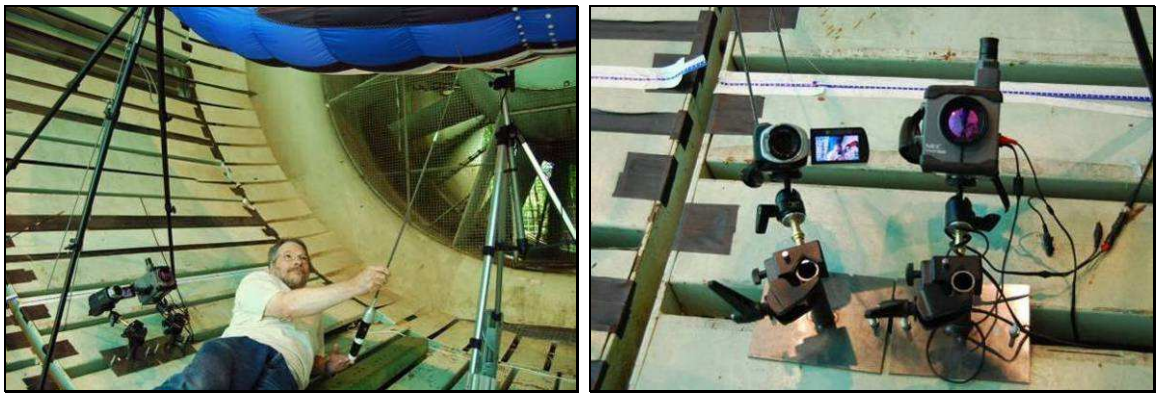

Figure 5.23: The thermography setup with the two cameras and the microphone. The hairdryer is inside the kite.

Figure 5.23 shows the test setup. An HD camera records a normal film. The IR camera is connected to another camera to record the IR images. A microphone was used to listen for turbulence and confirm that the temperature differences that were seen with the IR camera were really also indicating turbulent flow. The sound of the microphone was recorded together with the IR images. Later the sound was separated from the movie, filtered with a noise filter and recorded again with the IR images. With video software the images form the HD camera and the IR images were edited and synchronized. The result can be found in the movie "Kite Thermography" on Youtube [34].

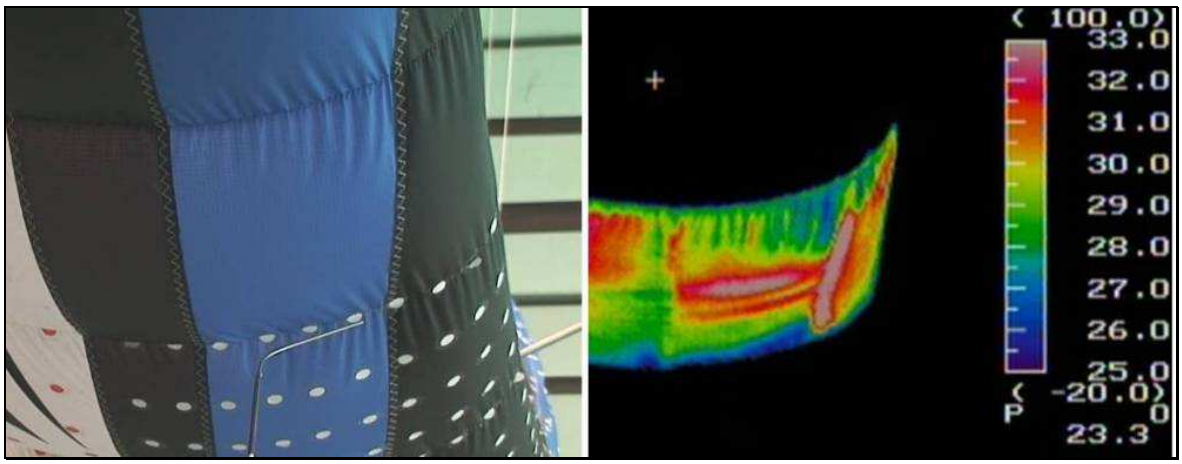

Figure 5.24: Hot spots and cold spots on the nose of the kite show the laminar and turbulent regions respectively.

The thermal image, shown in figure 5.24 clearly shows the development of hot spots and cold spots on the surface. Clearly the area around the wrinkles and downstream of the seams is colder than the other areas. In principle these hot and cold zones could also come from non-uniform mixing of the hot air inside the wing. To rule this out two checks were performed:

- One was, as described before, using a microphone to listen for turbulence. The resemblence between what was seen and what could be heard was striking and indicated very clearly that thermography can be used on this type of kite.
- The second check was to put a turbulator on the wing. This would trip the flow and make it turbulent. Behind the turbulator a cold zone should appear. The result can be seen in figure 5.25.

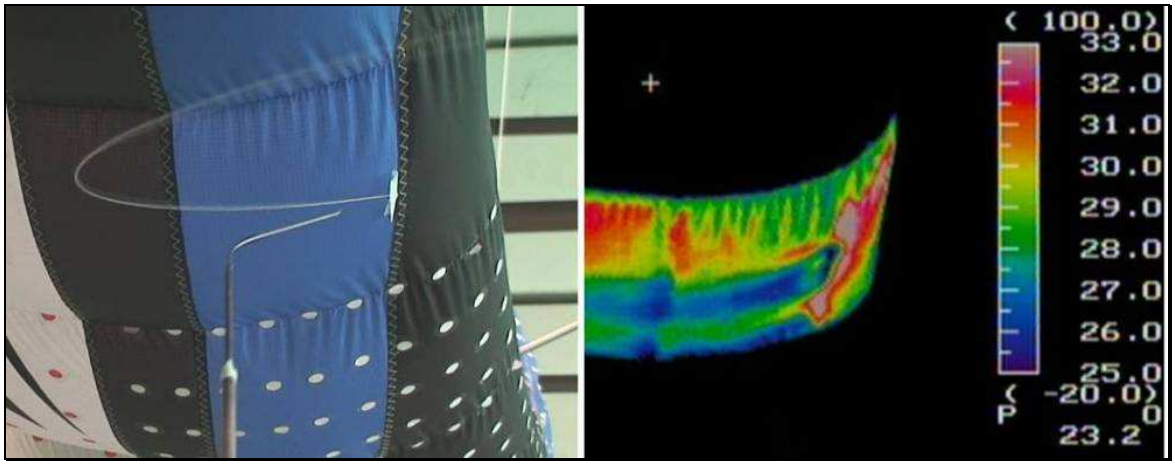

Figure 5.25: A cold turbulent wedge can be seen on the infra-red image when a little turbulator is stuck onto the wing.

6 Kite geometry analysis

In this chapter the different shapes of the kite that were measured in the windtunnels are discussed. Five different CAD models are compared. The consequence of these different shapes for the aerodynamics of the kite will be discussed in chapter 7.

Three of the five models are reconstructed from the photogrammetry data:

- Maximum lift coefficient (high angle of attack) at 8m/s (shown in green)
- Maximum lift coefficient (high angle of attack) at 16m/s (shown in red)
- Minimum angle of attack (low angle of attack) at 16m/s (shown in light yellow)

One model is reconstructed from the laser scanner data. Only one unsmoothed surface mesh was made because it was soon very clear that the photogrammetry data yielded better results than the laser data. The laser data model is:

- Minimum angle of attack at 16m/s (shown in brown (3D) and white (2D))

And the fifth model is the original CAD model from the manufacturer:

- Designed at an intermediate angle of attack (shown in blue)

For an explanation about how these surface models were constructed from the photogrammetry and laser scan data the reader is referred to Appendix D. The surface reconstruction of the point data is a time consuming process. This allowed that only three of the photogrammetry photo series were converted into surface models. Most interesting for the Laddermill application are the minimum and maximum pull that the kite can produce at high speed. The low speed case was processed to see what the influence of the dynamic pressure on the deformation of the wing is.

To be able to discuss the geometry of the wing each cell and rib is named, see figure 6.1. Since the kite has an even number of cells it has a central rib exactly in the middle of the wing (the root). This rib is called rib1. Further towards the tip the ribs are numbered rib2, rib3, etcetera…
The cell in between rib1 and rib2 is called cell1 and further towards the tip the cells are numbered cell2, cell3, etcetera…

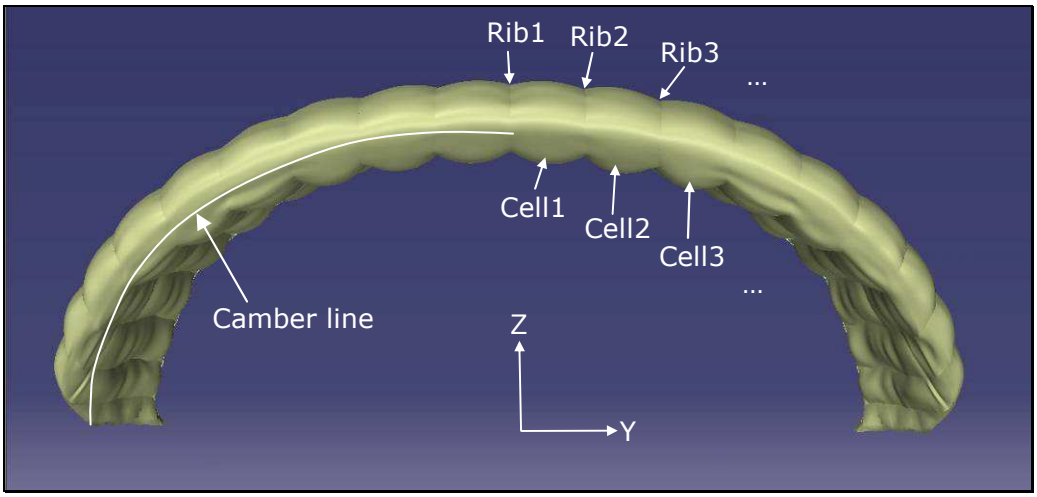

Figure 6.1: Definitions.

Figure 6.1 also shows the term "camber line". In aerodynamics camber line usually refers to the deviation of the middle line of an airfoil from the chord line. In the theory of non-planar wings the term camber is also used for the out-of-plane curvature of the wing planform. Hence, a non-planar wing can have a certain "wing camber" and the airfoils of the wing can have a certain "airfoil camber". In the remainder of this report airfoil camber is not discussed. Every reference to camber is used to indicate the wing camber: the out-of-plane curvature of the wing planform.

Lift is the aerodymic force that an object produces in a direction perpendicular to the free stream direction. With that in mind one can say that a significant amount of the lift that a kite with such a highly cambered wing planform produces is directed in the spanwise or sideways direction (Y-direction). This lift doesn't contribute to the pulling force of the kite (force in Z-direction). To distinguish between these two, lift (any aerodynamic force perpendicular to the free stream direction) will just be refered to as lift and the pulling force of the kite (in Z-direction) will be refered to as projected lift, because it is a projection of the lift distribution in Z-direction.

Similarly, the kite has a flat area (the area the kite would have if it was lying flat on the ground) and a projected area (the shadow of the kite on the ground when it is flying). And with the same reasoning the kite has a flat wing span and a projected wing span.

6.1 Ballooning

In chapter 4 the numerical simulation of a ballooned wing profile was discussed. The ballooning that was superimposed on the NACA0012 profile, as shown in figure 4.2, was taken from windtunnel research on a quasi-2D section of a paraglider. Using the photogrammetry data from the windtunnel tests the ballooning of the kite can be analyzed in the same way. Figure 6.2 shows the airfoil of rib1 and cell center1.

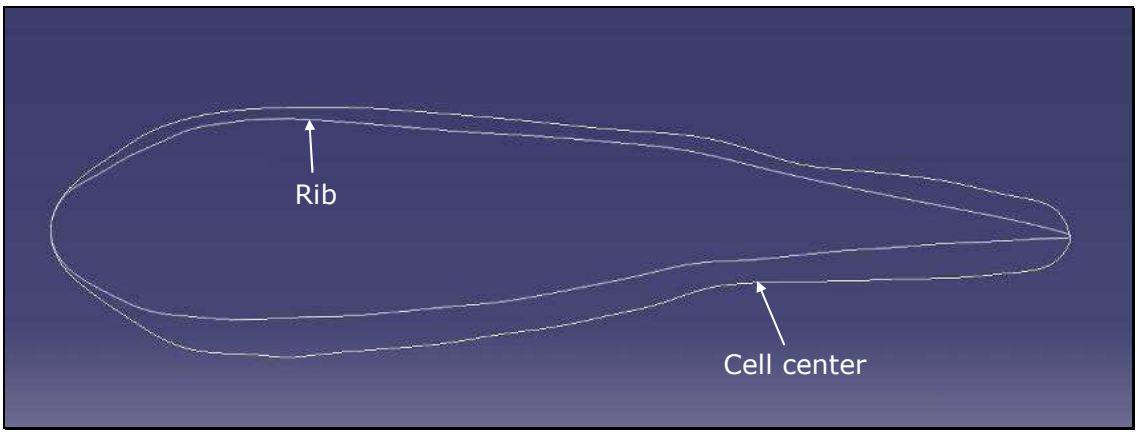

Figure 6.2: Cross section of the kite at rib1 and cell center1 of the case with maximum lift coefficient at 16m/s.

One can see that there is a huge thickness increase of the cell center profile, especially on the bottom surface. Figure 6.3 shows this deformation in graphs. The left graph shows the thickness increase of the profile as a function of the chord length. It shows that the the maximum thickness increase in the forward part of the airfoil is 5.3% of the chord length. Given that the design airfoil is almost 18.9% thick this means a relative thickness increase of 28%. The point of maximum thickness has moved from 20% to 30% of the chord length.

The right graph of figure 6.3 shows how the thickness increase of the cell center is devided over the top and bottom surface. More than 1 means more thickness increase at the bottom. The graph shows that on the largest part of the chord the thickness increase at the bottom surface is more than two times the thickness increase at the top surface. This happens because the manufacturer tries to keep the airfoil shape on the top surface as close as possible to the design airfoil. By making the skin panels on the top surface narrower and on the bottom surface wider more tension is built into the top surface, which results in less ballooning.

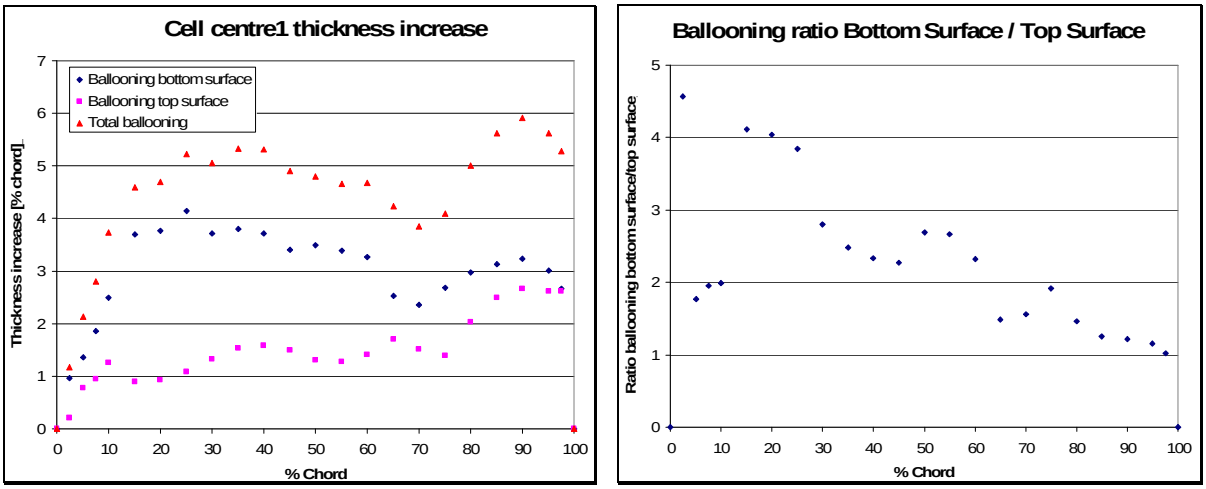

Figure 6.3: Left: Thickness increase at the cell center as a percentage of the chord length. Right: The ratio between ballooning at the bottom surface and top surface.

When comparing figure 6.3 with figure 4.2 one can see that the Babinsky's model must have had more tension at the leading and trailing edge compared to the middle section of the kite. His model shows a much smoother increase and decrease of the ballooning in those areas. Looking back at the decision to distribute the ballooning evenly between top surface and bottom surface in the analysis of chapter 4 it can be concluded that for future analyses there should be more ballooning at the bottom surface. The data from figure 6.3 could be used as a guideline.

6.2 Angle of attack

A kite surfer has control over the kite by pulling lines that are connected to the trailing edge of the kite. Via a pulley system also the lines that are attached further towards the leading edge are pulled down by a certain amount. By pulling the brake lines rib1 makes an almost clean rotation, so with very little defomation of the airfoil. More towards the tip, where the wing is cambered downwards (anhedral) the ribs not only change angle of attack but they also yaw with respect to the free stream direction. Cell10, the tip cell, is at approximately 90 degree anhedral angle with respect to cell1. However, this doesn't mean that it only makes a yawing motion when the brakes are pulled. The brake line cascade is made in such a way that when the brakes are pulled the angle of attack at the tips increases significantly. Because cell10 has an almost perpendicular orientation with respect to cell1 a lift increase on cell10 contributes very little to the projected lift. The reason that the tips are designed to have a large increase in angle of attack when the brakes are pulled is to steer the kite. The tips act as drag flaps that cause a strong moment around the top axis (Z-axis) of the kite.

Figure 6.4 shows the angle of attack distribution of the kite for the three photogrammetry cases. The angle of attack is measured by projecting the free stream velocity vector in the plane of a rib and measuring the angle between the chord line of the rib and the projected free stream vector. This is shown in figure D.4i of Appendix D. A number of things immediately catch the eye:

- The angle of attack of the ribs progressively increases towards the tip (wash-in)
- In the high angle of attack situation the angle of attack at the tips is without a doubt far beyond the stall angle of the airfoil
- At higher wind speed the kite is flying at a higher angle of attack
- The angle of attack change at the tip is much larger than at the root

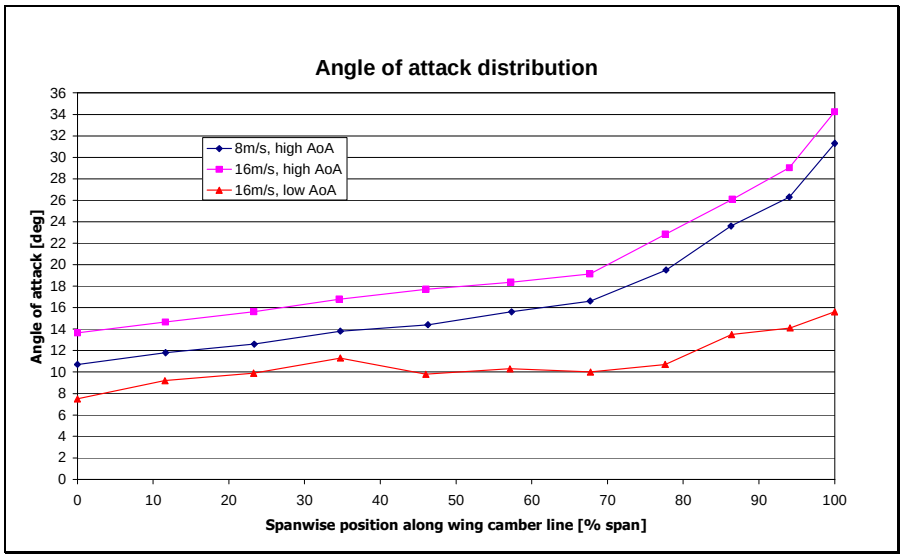

Figure 6.4: Angle of attack distribution on the flat span.

The extremely high angle of attack at the tips is beneficial for the steering performance of the kite. This allows the kite to make sharp, aggressive turns. However, when both brake lines are pulled symmetrically to increase the pull of the kite, the stalling tips will likely slow down the kite very fast and stall the whole kite.

The fact that the angle of attack increases with increasing wind speed in the high angle of attack situation corresponds with the data shown in figure 5.19. The lift-to-drag ratio decreases with increasing wind speed and this increases the pitch angle and angle of attack of the kite.

The strong angle of attack increase at the tips probably comes from the short chord of the tips cell. Only a small amount of line pull on the rear lines causes a large rotation of the airfoil there.

6.3 Leading edge deformation

As shown in figure 5.18 the kite undergoes a significant shape change at the leading edge when it is flying at minimum angle of attack. These dents that appear in the leading edge can also be seen very clearly in the CAD model of figure 6.5. As discussed in paragraph 5.4 they come from the fact that the leading edge stagnation point is not directly over the air intake valves anymore. The kite looses internal pressure.

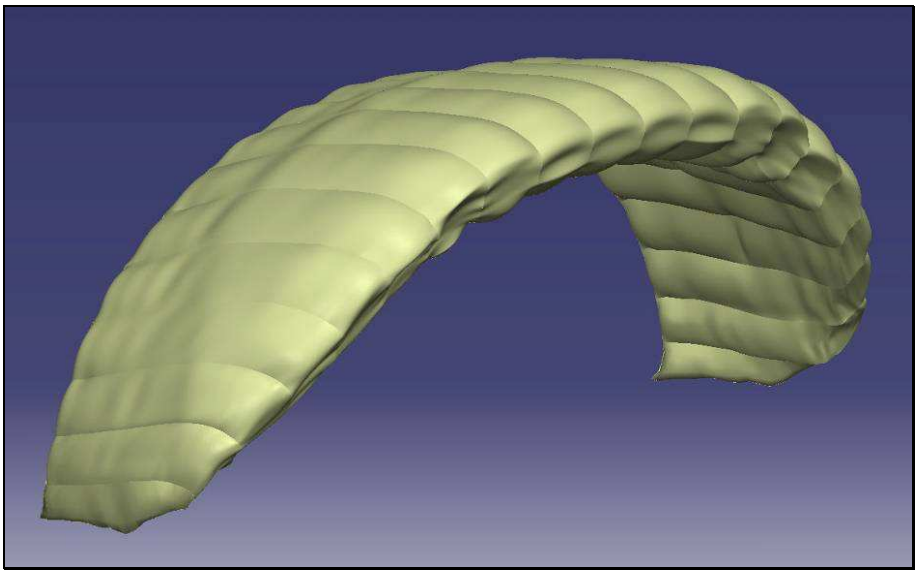

Figure 6.5: Dent in the leading edge at low angle of attack.

Another deformation that appears at the leading edge is caused by the load introduction and the line attachment points. There is a strong stress concentration where the suspension lines connect to the ribs. From the attachment point the load should spread in the rib and be distributed along the top surface.

Figure 6.6 shows rib 1 thru 4. Right in line with the orientation of the most forward lines (a-lines) one can see a flattening of the profiles at the upper surface.

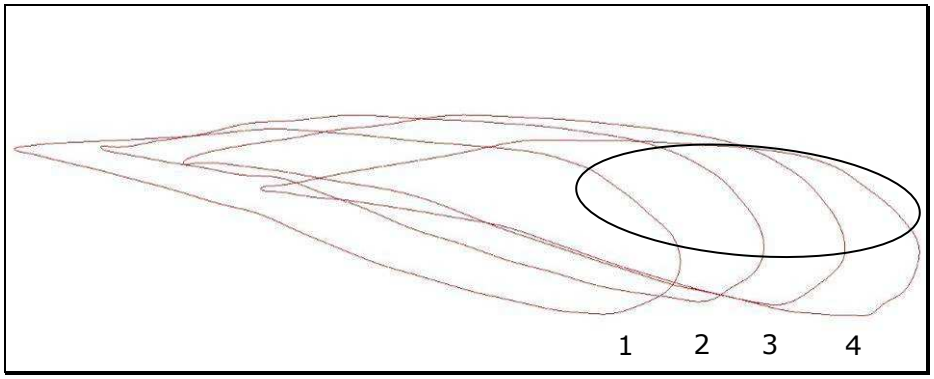

Figure 6.6: Leading edge deformation of ribs 1 thru 4.

This flattening is most pronounced at ribs 1 and 4. This can be explained in the following way: apparently the load doesn't spread very well in the rib fabric. Due to the flexibility of the fabric the load is transferred to a concentrated spot on the top side of the rib. Because of this the lines at the bottom side of the ribs pull dents in the top side of the ribs. The fact that this is more pronounced at rib1 and 4 can be explained by the fact that these two ribs are not supported by lines but by V-tapes, as shown in figure 6.7 (see also figure 3.2). The V-tapes connect at the line attachment points of the neighboring ribs and then run diagonally through the cell and attach to the rib just below the top surface. Because they are connected so close to the top surface there is no space for the load to spread in the rib and the V-tape just pulls a dent in the top surface.

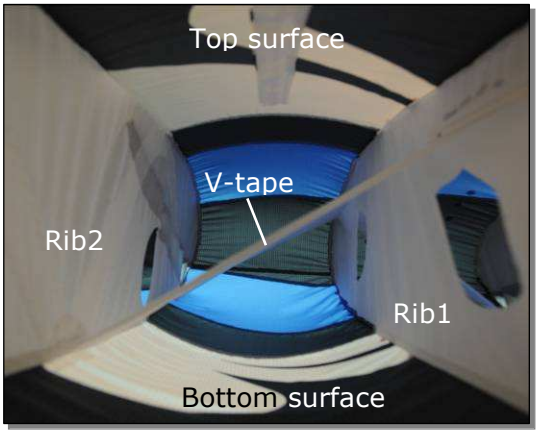

Figure 6.7: Looking inside the kite from the trailing edge towards the leading edge one can see a V-tape in cell1.

The severity of this dent can be quantified by comparing the shape of rib1 with the shape of the airfoil as it is designed for this kite (see figure 6.8). On the top side the surface is pulled down by almost a centimeter. Also at high angle of attack there is still a dent at the stagnation point. At that point the pressure on the inside and on the outside of the kite is equal. The fabric doesn't balloon at that point and there is no tension in the bottom surface fabric there to pull the rib into shape.

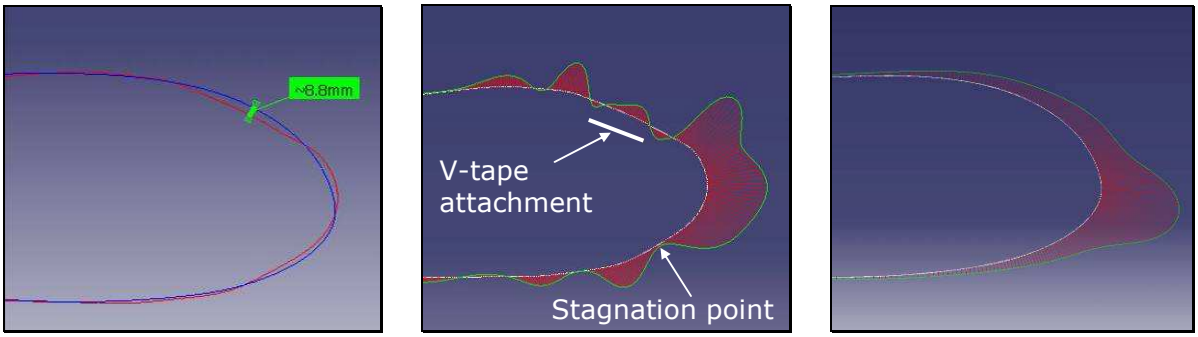

Figure 6.8: Leading edge deformation rib1. Left: in blue the design shape, in red the flying shape at high angle of attack. Middle: curvature analysis of the flying shape. Right: curvature analysis of the design shape.

By analysing the curvature of both the design airfoil and the flying airfoil the distortion of the profile becomes even more apparent. There is a significant reduction in curvature near the leading edge stagnation point, but much more important a reduction of curvature at the top surface. The region on the top surface where the curvature is reduced is a very important part of the airfoil. This is normally the region on the airfoil where most lift is produced. Since the static surface pressure is directly related to the local curvature of the airfoil, a reduction of the curvature in this region can have serious implications for the lift. Figure 6.9 shows that at the second V-tape also a dent in the profile and a decrease in curvature exist. Further discussion about the aerodynamic effects of these dents will follow in chapter 7.

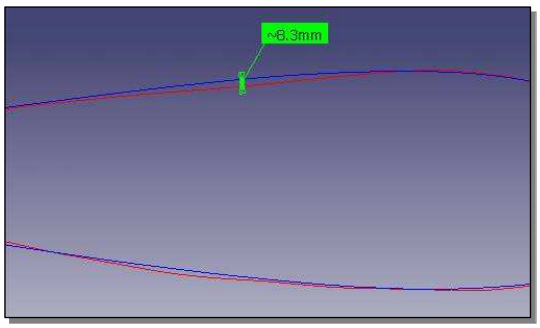

Figure 6.9: Dent caused by the second V-tape attached to rib1.

Figure 6.10 shows that flattening that is present at the rib airfoils of figure 6.6 is also present at the cell centers. The cell centers are already very much deformed compared to the ribs. But with the right curvature also a thick airfoil can be capable of generating good lift values.

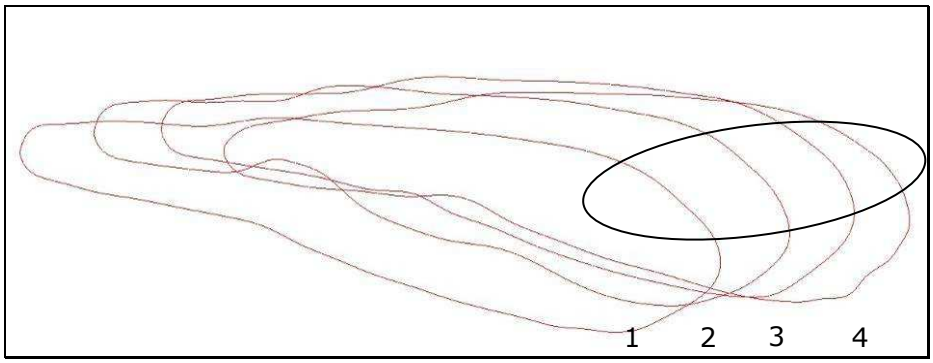

Figure 6.10: Leading edge deformation of cell centers 1 thru 4.

The deep hollow on the bottom surface of cell center2 comes from fabric that was used to close the flaps of the kite. The tension in the fabric was locally higher there than in the neighboring cells and because of that there is very little ballooning.

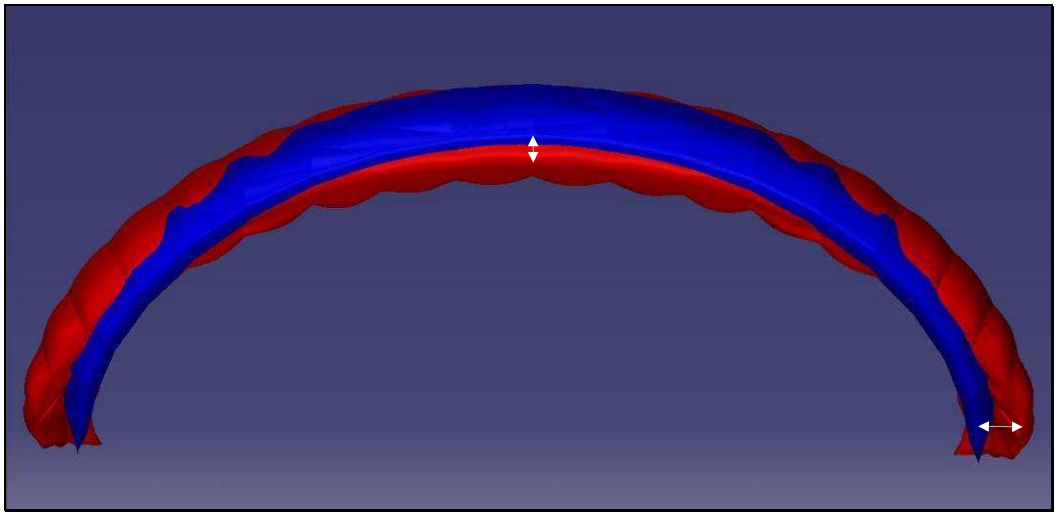

Figure 6.11: Difference in the leading edge wing camber between the design shape the flying shape at high angle of attack.

The kite not only experiences such local effects as ballooning and dents in the profiles. Looking at the global geometry of the kite there are also clear differences. Compared to the design shape (blue) of the manufacturer the spanwise camber of the leading edge of the flying kite is quite different (see figure 6.11). The design shape is more or less the average shape that the kite will fly at. So the fact that at the tip the leading edge is pointing much further outwards in figure 6.11 is not very strange. But that the leading edge at the center of the wing is further down is remarkable, because the most forward suspension lines (a-lines) don't shorten when the brakes are pulled. When both models are put on top of each other with the leading edges matching then the tips of the design shape point much further back compared to all three measured models. One reason could be that there is an error in the mirror plane of the flying shapes.

But because rib1 is taken as the mirror plane an error larger than one or two tenths of a degree is unlikely. This doesn't result in the large differences that are observed in figure 6.11. The most likely reason that the leading edge of the flying kite is further down compared to the one of the design shape is because of the built in tension in the kite. After the initial design the fabric panels at the leading edge are made narrower to increase the spanwise tension in the nose. So the cell width at the leading edge is reduced in that way. This decreases the ballooning at the nose and it increases the bending stiffness of the wing in the "sweep forward/aft" direction. It also makes the leading edge come down. Apparently these changes haven't been incorporated in the manufacturer's 3D model.

6.4 Trailing edge deformation

In figures 6.2 and 6.10 it was already very clear that the trailing edge in between the ribs is very thick and rounded. Theoretically this is disadvatageous to the airfoil in different ways. First of all the basic principle by which an airfoil works is the fact that it has a sharp trailing edge. This fixes the trailing edge stagnation point, because the air can't flow around a sharp trailing edge. This forces a faster flow over the top side of the airfoil. When the trailing edge is rounded air is allowed to flow upwards across the trailing edge. This reduces the flow over the top surface of the airfoil and that reduces the lift. Secondly, a thick trailing edge causes a wider wake behind the airfoil. The flow vizualization in figure 6.12 shows that the smoke accumulates at the trailing edge. This indicates a thick separated wake behind the wing.

Figure 6.12: Smoke accumulates at the thick trailing edge.

Another deformation that occurs at the trailing edge is a change of shape of the trailing edge spanwise camber line. The trailing edge is reinforced with a strong and stiff tape. This allows very little stretch in the trailing edge. The consequense is that when the trailing edge of the tip moves outboards the trailing edge at the center of the wing will move downwards. This can be seen in figure 6.13 and 6.14. What is most important about this change is that when the brakes of the kite are released and the angle of attack is decreased the trailing edge at the tips move outboards, shown in the right picture of figure 6.14. This then pulls the trailing edge of the center part of the wing down, visible in both figure 6.13 and 6.14. Generally, the center of pressure of a wing moves towards the trailing edge when it extends a flap downwards. This means in this case that when the angle of attack of the kite is reduced that the center section of the wing may get an unwanted nose down moment. It would be much more beneficial for the design if the kite would have a reflexed airfoil shape when it is flying at low angle of attack. This reduces the risk of collapse of the kite in turbulent conditions. This is also the intention of the manufacturer but apparently the reinforcing tape in the trailing edge prevents this.

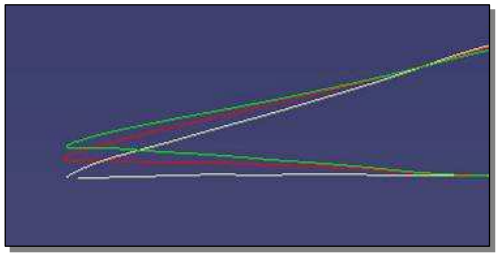

Figure 6.13: Rib1 trailing edge pull down due to trailing edge camber line change.

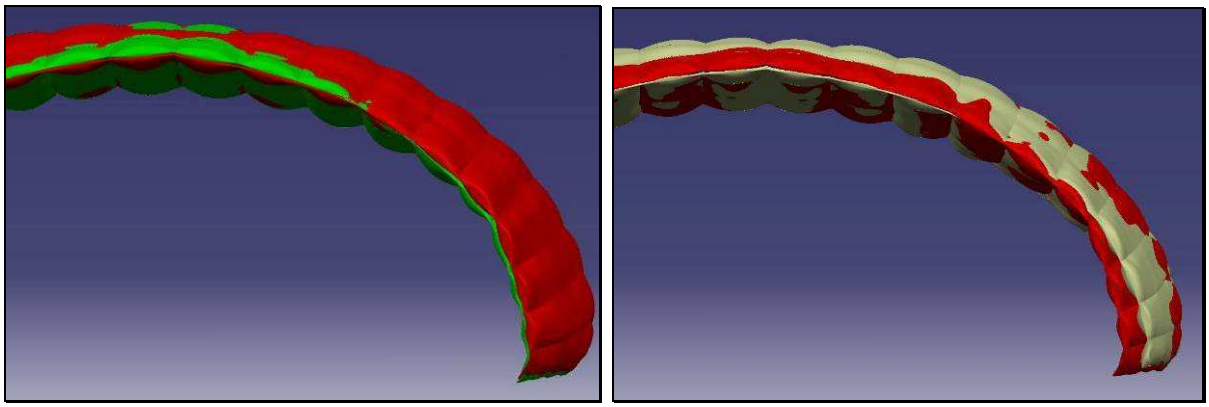

Figure 6.14: Deformation of the trailing edge camberline. Green: high angle of attack 8m/s; red: high angle of attack 16m/s; light yellow: low angle of attack 16m/s.

A similar effect is caused by by the flaps that are built into the kite (figure 6.15). To give these flaps their shape extra tension is built into the kite at the chordwise position where the flaps are located. The photogrammetry data reveals that this tension causes a "kink" in the in the wing. While flying the kite outside, this kink is hardly visible because the cloth is very tranparent to light and there is very little contrast. The kink is not caused by the fact that the flaps were closed for the windtunnel tests because photogrammetry results that were taken when the kite was flying at the beach with the flaps open also reveal the kink. By shining light right along the surface of the CAD model the kink in the wing becomes very clear (figure 6.16).

Figure 6.15: The jet-flaps in the kite.

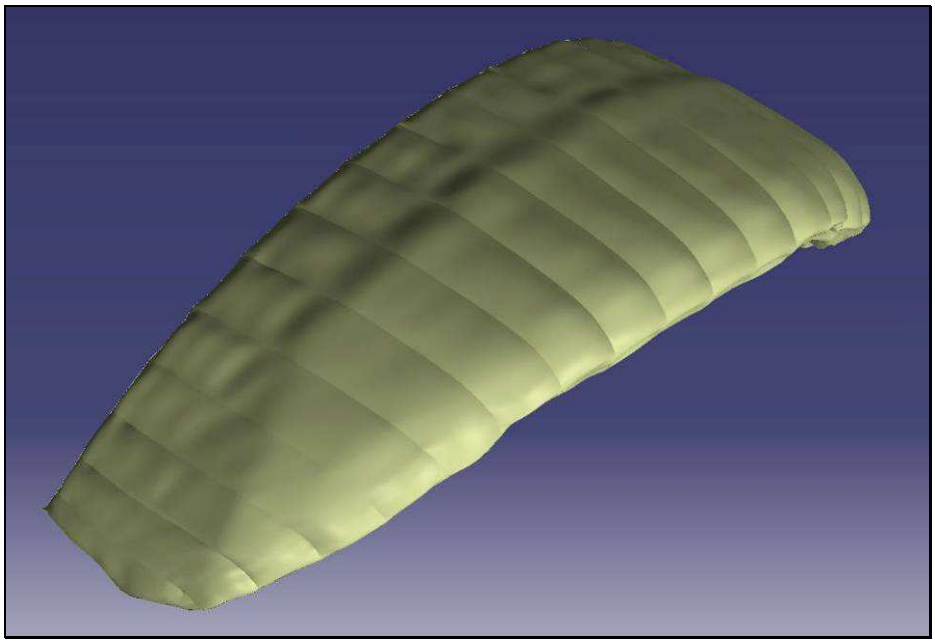

Figure 6.16: The kink in the wing near the position of the jet-flaps.

6.5 Wing camber

By taking a cross section of the different models in spanwise direction one can see how the different loads change the position of the tips with respect to the center of the wing (figure 6.17). The difference between the green and the red line is the difference between flying the kite at 8m/s or at 16m/s, or roughly a quadrupling of the load (4.4 times larger according to table 5.13). The tip displaces by 38mm. When the brakes are released at 16m/s (the difference between the red model and the light yellow model) the tip displaces by approximately 20mm. The exact change is difficult to quantify in this situation because the whole tip also rotates. That's why the difference in figure 6.17 seems larger. Generally speaking, the shape change of the spanwise camber and the ballooning due to a change in wingloading is small compared to the deformation due to a different brake position.

Clearly the projected span of the flying shapes is larger than that of the design shape. However, except for a very small difference the projected area of the design shape is the same as that of the flying shapes. This is because the chord length of the design shape is significantly larger than that of the flying shape. Why this happens will be explained in the next paragraph.

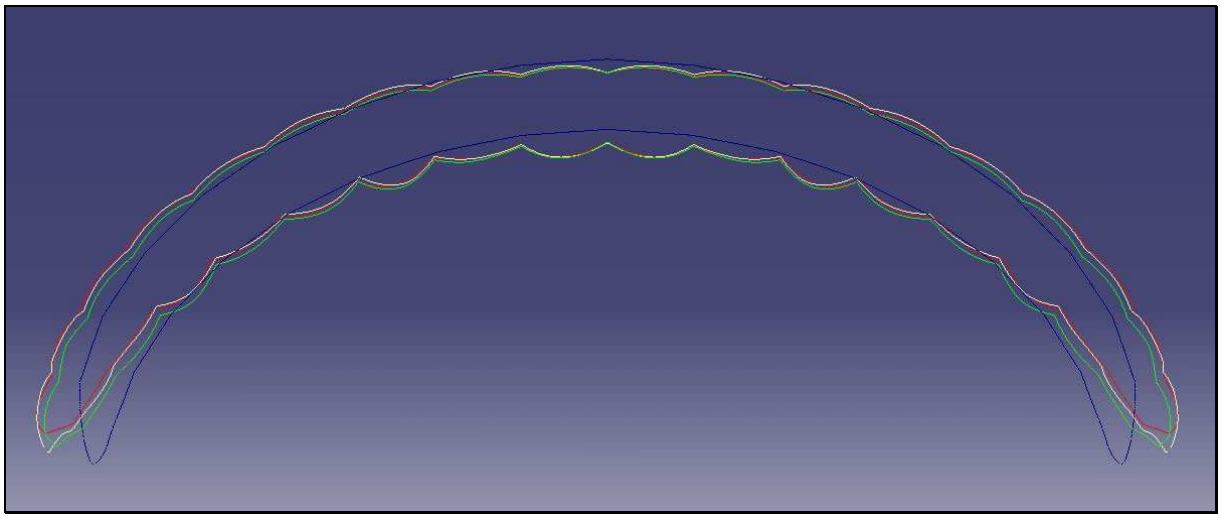

Figure 6.17: Spanwise cross sections at 40% of the root chord.

6.6 Wrinkles

In a large part of the kite's surface area wrinkles develop when the kite inflates. This happens because of the simple fact that pieces of two dimensional fabric are formed into a three dimensional shape. When a cell balloons the cross section at the cell center has a longer curve length than the cross section at the rib. For example, the airfoils shown in figure 6.2 have a difference in curve length of 63mm. The fabric is not flexible enough to stretch that distance at the cell center. As a consequence the fabric at the rib is compressed. Fabric can't withstand compression and as a result wrinkles form near the ribs (figure 6.18). Because the outer surface is sewed to the ribs this means that if the outer surface wrinkles around the ribs the ribs themselves must also wrinkle.

Figure 6.18: Wrinkles in the fabric.

In figure 6.7 the wrinkles in the ribs are visible, but by removing the colors and enhancing the contrast of the image the wrinkles become even more clear, see figure 6.19.

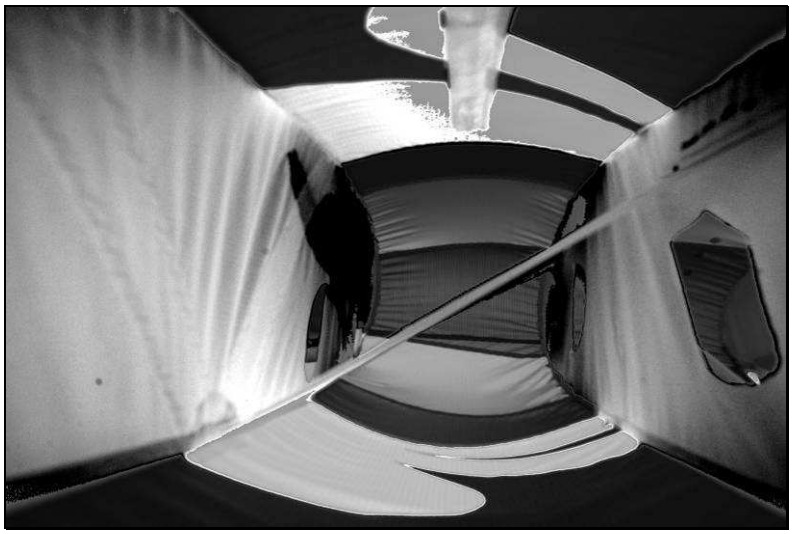

Figure 6.19: Wrinkles from the top and bottom surface continue in the ribs.

When the ribs wrinkle they must become shorter. Table 6.20 shows the root chord length of the different models. It shows that the ribs become approximately 3.5% shorter. At low angle of attack the center rib becomes even shorter. But this happens because of the dent in the leading edge (as shown in figure 6.5) and not because of wrinkling. The shorter ribs cause a reduction in wing area. Because they only shorten in chordwise direction and not in thickness direction the ribs become effectively thicker.

Table 6.20: Chord lengths of rib1.

Model	**Rib1 chord length [mm]**
Manufacturer/design (blue)	1340
High AoA, 8m/s (green)	1290 (-3.7%)
High AoA, 16m/s (red)	1296 (-3.3%)
Low AoA, 16m/s (light yellow)	1272 (-5.1%)

In principle the number of wrinkles could be reduced by making the wing out of more panels that are cut to give it a more three dimensional shape, but this would probably increase the design and production cost of the wing significantly.

6.7 Laser scans

Up to now the laser scans that were made in the Large Low-speed Facility were not discussed. The reason that they have been given little attention is that the photogrammetry gave better data than the laser scans. The kite moves too much to obtain accurate data from the laser scanner. The problem with the laserscanner is that one basically works with two reference frames. One is fixed to the scanner and one is fixed to the kite. Both the kite and the laser scanner produce turbulence in the windtunnel and dispite the fixation this makes the kite move as much as a few centimeters. Because the scanner takes about one minute to make a scan every motion of the kite with respect to the scanner is directly translated into an error.

In the case of photogrammetry recording of the targets is almost instant. Besides that there is only one reference frame because the position and orientation of the cameras is determined from the targets on the kite and not from some external reference.

Lee and Li [16] used laser scanning to scan a scale model of a ram-air wing. They used a triangulation scanner that scans the deformation of a line. It scans the model line by line. Their 3D models show ripples in the surface where the kite changed position in between the line scans.

Figure 6.21 shows a mesh of one of the point clouds. The seven raw scans together consisted of approximately 40 million points. By cutting the windtunnel from the point cloud approximately 20 million points remained. To reduce memory consumption the point cloud was then filtered and reduced to 4 million points.

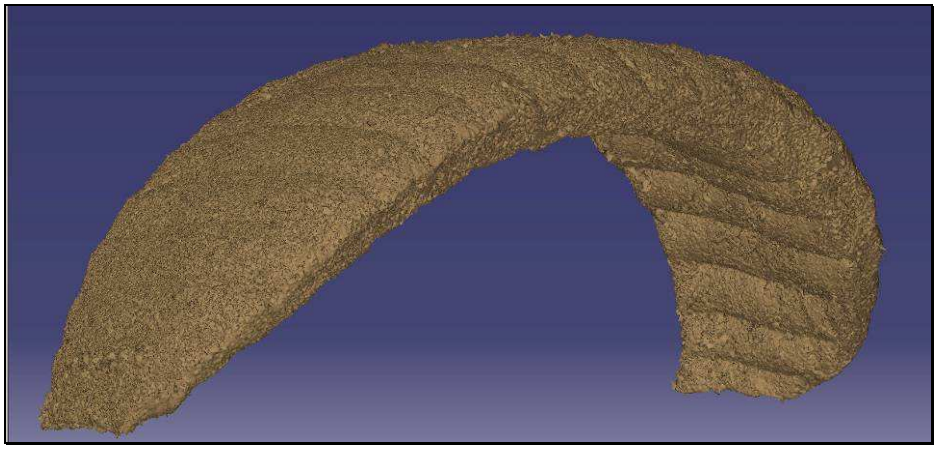

Figure 6.21: Meshed point cloud from a series of laser scans of the kite flying at minimum angle of attack at 16m/s.

Data from a laser scanner is always noisy to a certain extend. The data needs to be smoothed to get a smooth surface. The problem with smoothing algorithms is that they first smooth the sharpest corners. In case of the kite the tips and trailing edge loose their shape when the surface is smoothed. To avoid this problem it was planned to use the same method as in photogrammetry to reconstruct the surface: to create cross sections of the point cloud and blend these together.

However, the suction side of the wing consisted of a 2 to 3cm thick crust of points. This was simply too noisy to make any reasonable approximation of the data.

Figure 6.22 shows a cross section at rib1 of all models. Although the laser data on the bottom side is not too bad on the top side the basic shape of the airfoil can be recognized but to determine the exact airfoil shape from this cloud of points doesn't make very much sense.

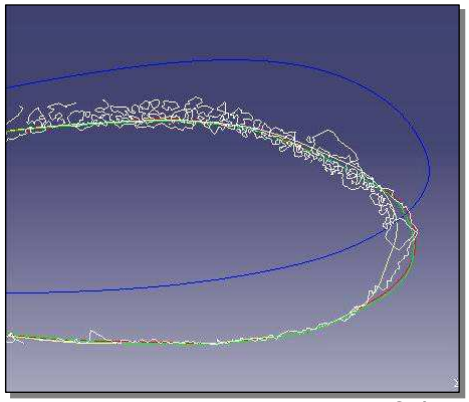

Figure 6.22: Cross section of the leading edge of all models at rib1.

Although the laser data is too noisy to be processed into a smooth surface like for the photogrammetry, after meshing (as shown in figure 6.21) it is possible to compare the overall geometry of the laser data and the photogrammetry. The case that is compared is that of low angle of attack flying at 16m/s. Other cases could not be compared because the high angle of attack case stalled in the LLF windtunnel. That means that with the brake setting of high angle of attack (+39mm according to table 5.13) the kite would immediately pitch to a 90 degree angle. This difference in behaviour may have been caused by the different turbulence intensities in the tunnels and the different wall effects. These two may have changed lift and drag in such a way that this could happen.

The most obvious difference between the two low angle of attack cases is the reduction in span of the kite in the LLF windtunnel (figure 6.23). This change in shape may have been caused by the different wall effects of the tunnels.

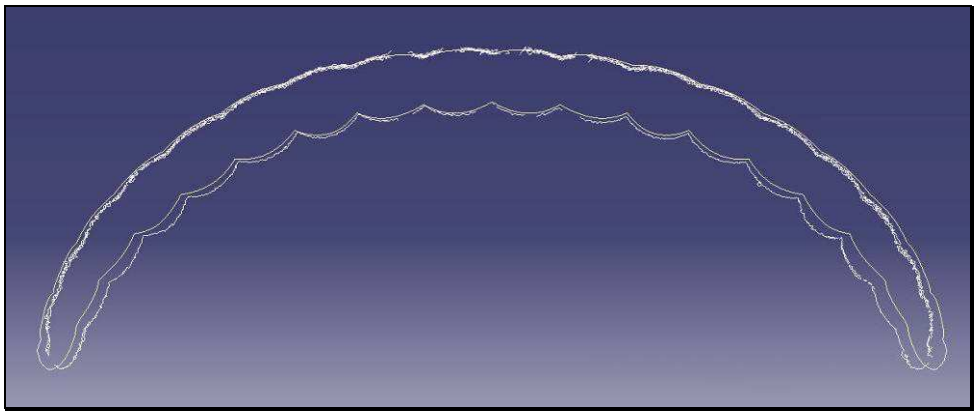

Figure 6.23: Spanwise cross section at 50% of the root chord of the low angle of attack case. The scribbled line is the laser data.

Wall effects change the lift and drag of a wing. A wall in the vicinity of a wing reduces the induced flow. This means that the tip vortices have less effect and that the local angle of attack along the span increases. The result is more lift and less drag. This is comparable to the ground effect that aircraft experience when they fly very close to the ground.

In the BWK windtunnel the walls were much closer to the kite than in the LLF windtunnel. This should cause then that the kite in the BWK tunnel experiences more lift and less drag. This was confirmed by the load cells: the kite had approximately 10% more lift in the BWK windtunnel. It was also confirmed by the fact that the high angle of attack case flew normally in the BWK tunnel but stalled in the LLF windtunnel.

The effects should be most noticable near the tips because the BWK tunnel had a round test section and the LLF tunnel a rectangular test section. So the distance from the wall to the wing had the largest difference at the tips. With CFD a case was made of the kite flying at high angle of attack in the BWK windtunnel and one case with the walls of the domain so far away that wall effects were negligible.

As said before, theoretically there should be a reduction of force on the tips. However, the CFD data showed an increase of force on the outer four cells when the walls were taken away. This seems confusing, but there is strong suspicion that this has to do with the fact that the effect of the walls was checked on the high angle of attack case. As can be seen in figure 6.4 in the high angle of attack case the local geometric angle of attack of the outer four cells is more than 20 degrees. This is beyond the stall angle of the airfoil. According to X-foil the design airfoil form the manufacturer stalls at 19 degrees. Post stall the lift reduces with an angle of attack increase. This means that when the windtunnel walls are taken away the change in induced flow causes a local decrease in angle of attack and because the outer four cells are stalled this causes an increase in lift. Also the center of the wing, where the local airfoil is not stalled, showed a decrease in lift. To prove this point completely another CFD case should be run with the low angle of attack case without wall effects. Unfortunately, there was no time to run this case within this project. But given the data form the load cells, the stall of the high angle of attack case in the LLF windtunnel and the CFD data, it is very likely that the difference in spanwise camber between the photogrammetry data from the BWK and the laser data from the LLF is caused by a difference in force on the tips that was caused by the wall effects.

6.8 Conclusion from the geometry analysis

Probably the most important conclusion that can be drawn from the analysis in this chapter is that photogrammetry is a very powerful and useful tool to analyse the geometry of a flexible structure. Most of the geometric deformations that were discussed are known by ram-air wing designers. By being able to quantify the deformations also appropriate measures can be taken. Most of the data shown in this chapter focussed on the deformation of the center of the wing. But in principle every rib and every cell can be analysed in detail to find more points for improvement in the design.

Looking back at the decision to distribute the ballooning evenly between top surface and bottom surface in the analysis of chapter 4 it can be concluded that for future analyses there should be more ballooning at the bottom surface. The data from figure 6.3 could be used as a guideline.

Other conclusions are:

- Over most part of the chord length the ballooning on the bottom surface is more than twice as much as on the top surface. If the analysis of chapter 4 were repeated the results from this chapter could be used as a guideline to devide the ballooning over the top and bottom surface.
- Looking at the angle of attack showed a very strong wash-in of the tips (increase of angle of attack towards the tips)
- The lines attached near the nose and especially the V-tapes in the nose cause a significant flattening of the top surface just behind the leading edge
- This flattening of the nose of the wing is also visible at the cell centers
- Also the b-lines (attached to the middle of the chord) cause a curvature decrease on the top surface
- The spanwise camber of the flying wing differs from the design shape in a way that the leading edge of the flying shape is further down and the tips are spread futher apart.
- Releasing the brakes of the kite pulls the trailing edge at the center of the wing down. This may make the kite more prone to collapsing. This effect is probably a consequence of the stiff reinforcing tape in the trailing edge.
- An increase of the dynamic pressure and the load on the kite slighly reduces the spanwise camber of the wing. But other than that there were no significant changes in the geometry observed.
- The tension that is built into the wing to give the jet-flaps their desired shape causes a kink in the wing over most of the span.
- The wrinkles in the cloth extend into the ribs. The rib at the center of the wing becomes approximately 3.5% shorter. This decreases the wing area and effectively increases the relative thickness of the ribs.
- Laserscanning is not a very suitable technique to analyse the shape of the kite. The kite moves too much due to its own turbulence and turbulence from the scanner. A technique is needed that instantly captures the shape.
- Noticable wall effects were experienced in the windtunnel. These wall effects affect the load distribution of the kite. This in turn also changes the shape of the kite. To obtain consistent data between windtunnel tests and CFD also the windtunnel geometry should be incorporated in the CFD analysis.

7 Kite computational fluid dynamics analysis

This chapter deals with the computational fluid dynamics (CFD) analysis of the three different kite geometries. The three geometries were reconstructed form the photogrammetry data that was gathered in the Böenwindkanal. Chapter 4 gave an introduction about how ballooning may in general affect the flow over an infinite wing. In chapter 6 it was described how the kite deviates from the intended design shape. With CFD it is possible to analyse how ballooning and other deformations affect the flow around the real kite.

7.1 Geometry of the CFD model

For a good comparison between the windtunnel measurement and the CFD results the geometry of the windtunnel must be incorporated in the CFD model. However, the geometry of the BWK windtunnel is very complex because the wall of the tunnel consists of approximately 250 beams. In between the beams are slits that allow air to pass throught the wall. At the end of the test section there are vanes where the tunnel contracts to a smaller diameter. The vanes and the slits in the wall are left out to keep the geometry simple and keep the number of CFD cells down.

The CFD model of the kite was built based on the same settings that were used for the model that was discussed in chapter 4 and shown in table 4.5 but with a few differences: all cells were scaled up by 30% because the chord length of the NACA profile was 1m and the chord of the kite is 1.3m. To improve the resolution in specific areas the cell size in the grooves was reduced to 2.5mm and on cell10 to 10mm. For simplicity it is assumed that the flow is symmetric, that the kite is symmetric and that the kite was centered in the windtunnel. As in chapter 4 the velocity inlet is placed 2.5 chord lengths in front of the wing. The pressure outlet is placed at the grid that guards the fan of the windtunnel. This doesn't allow a full development of the wake but in the real windtunnel the wake also can't develop completely because it is chopped up by the fan.

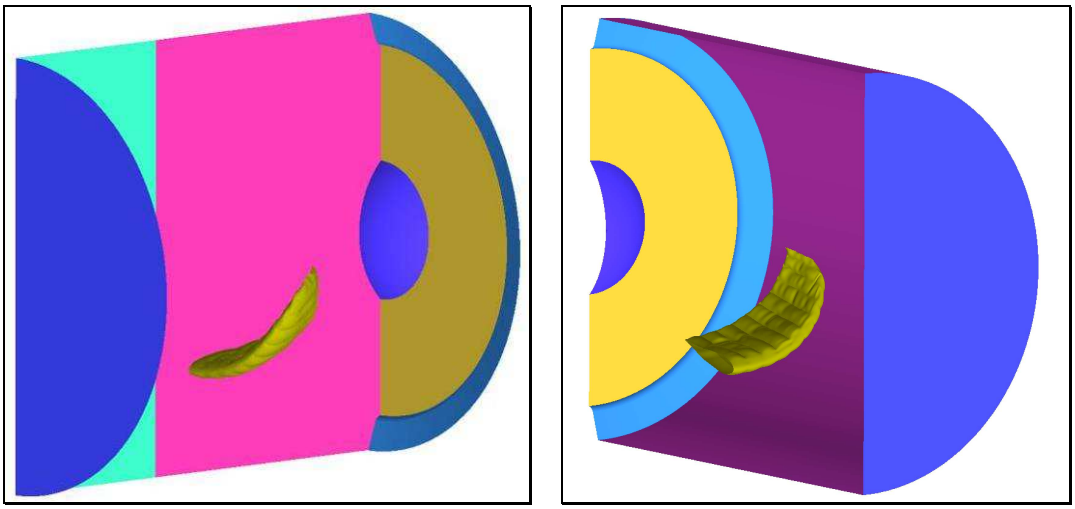

Figure 7.1: Geometry of the kite in the turbulent windtunnel in Stuttgart. See figure 5.03, 5.11 and 5.12 to see the real geometry of the windtunnel.

For the same reasons that were discussed in paragraph 4.2 the wrinkles that occur on the surface of the kite are not modelled. Also the suspension lines of the kite are left out.

Figure 7.2 shows the grid around the wing in the symmetry plane. At the wing's surface there is a boundary layer grid consisting of prism elements to capture the steep velocity gradient there.

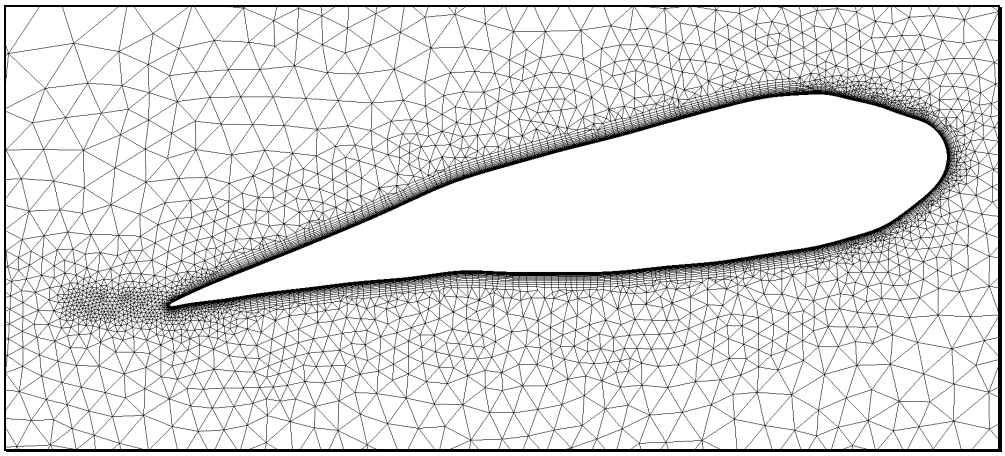

Figure 7.2: Grid around the wing in the symmetry plane.

In the wake of the wing the the mesh density is increased to capture the turbulent flow there. Near the trailing edge the wake mesh is very fine. Further behind the wing the mesh is coarser but it is still much finer than elsewhere, see figure 7.3.

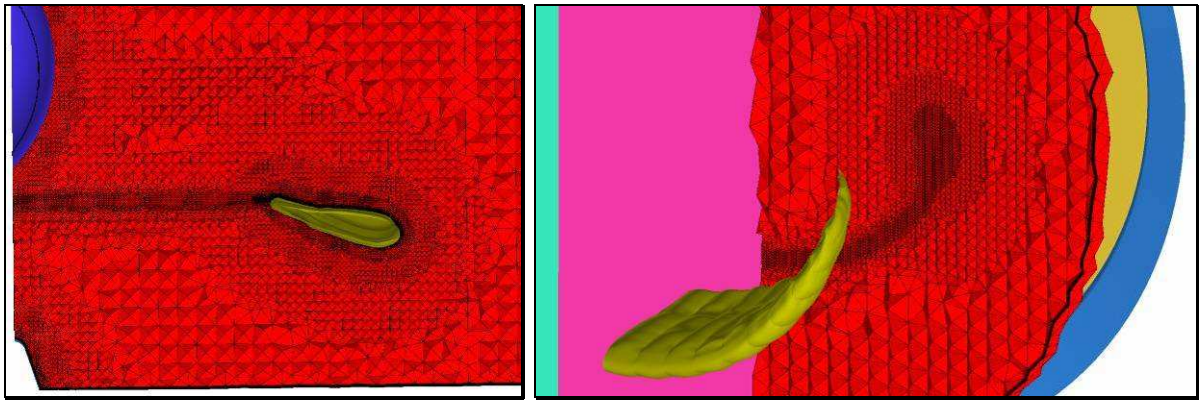

Figure 7.3: Increased mesh density around and behind the wing.

The boundary layer on the windtunnel wall was also taken into account. As on the wing there is also a boundary layer mesh on the the walls of the windtunnel.

To be able to quantify the influence of the windtunnel walls on the measured and calculated lift and drag one model was made with symmetry walls on all sides with at least 5 chord lengths of clearance on all sides, see figure 7.4. The maximum pressure change on the walls due to the presence of the wing was around $C_P = 0.03$.

All models consisted of in between 17 million and 21 million cells. For better accuracy inside the boundary layer two mesh adaptions with respect to y^+ were performed in every case.

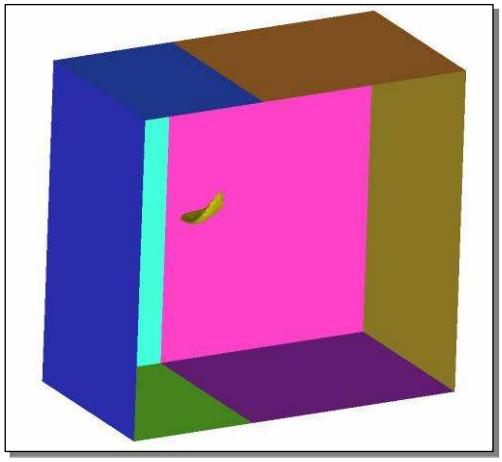

Figure 7.4: CFD domain with with walls far from the wing.

7.2 Effects of ballooning

In paragraph 4.4 it was shown on the NACA0012 wing with ballooning that when the flow is aligned with the ribs there is very little spanwise pressure difference between the ribs and the cell centers. When the flow moves across the cells at an angle with the ribs a region of high pressure forms at the ribs and a region of low pressure forms at the cell centers (figure 4.17). This pressure difference bends the flow away from the ribs making the ribs act more or less like flow fences.

On the kite in the windtunnel the same should happen with the difference that the cross flow is caused by flow that is leaking around the tips. Thus, the cross flow on the top and bottom surface is in opposite direction.

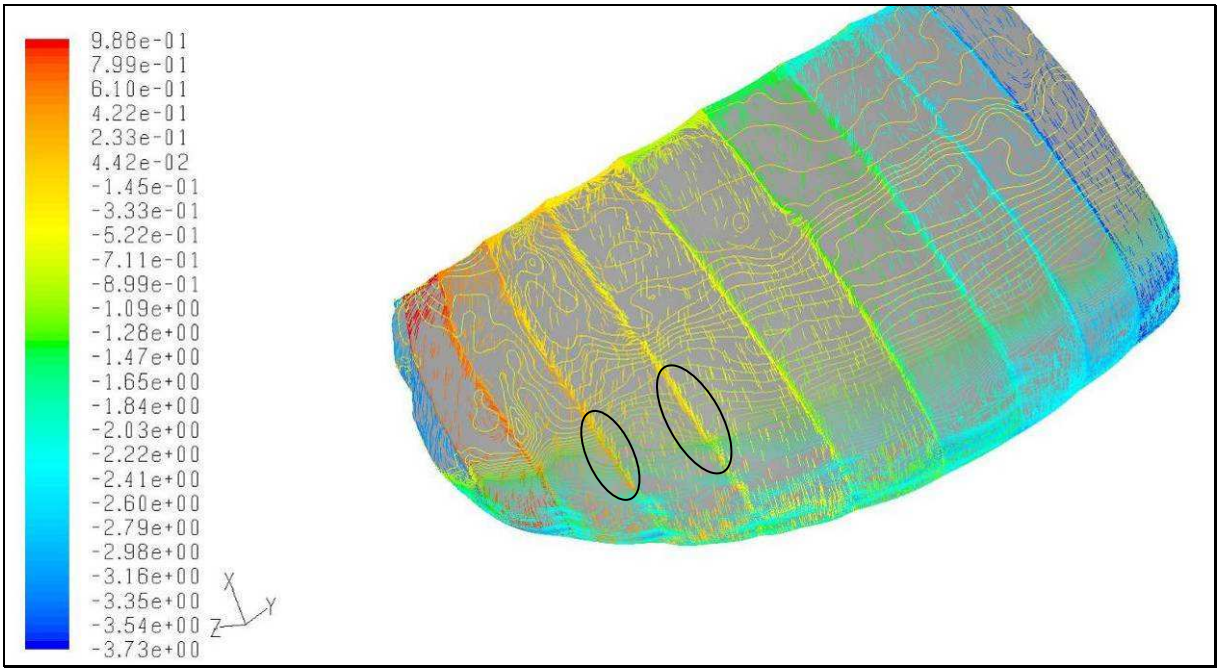

Figure 7.5: Oilflow (stripes) and pressure coefficient countours (lines) on the kite at high angle of attack at 16m/s. The "flow fence effect" of the ribs is only visible on parts of ribs 7 and 8. See also figure 4.16 and 4.17.

Looking at figure 7.5 one can first of all see that the pressure isobars on the real wing are much more chaotic than on the wing in chapter 4. The uneven distribution of the surface curvature leads to this erratic pattern. The "flow fence effect" is only visible on parts of ribs 7 and 8. Further inboard the flow is already well aligned with the ribs. Further outboard the flow is separated. The aft 30% of the wing is also covered with separated flow. In the low angle of attack case the pressure difference between top and bottom is less which results in less cross flow. There is less separated flow at the tip. In that case the regions where the "flow fence effect" can be found are of the same size but they are now on ribs 8 and 9.

On the bottom side of the wing the pressure gradient towards the tip is much smaller than on the top surface. Because of that the flow on the inner nine cells is well aligned with the ribs and the whole flow fence effect is absent. All in all the effects that the flow experiences when it crosses the ribs at a large enough angle are less than what was expected from the results in chapter 4. This is mainly because the angle between the flow and the ribs is not large enough or because the flow is separated. In chapter 4 the angle where the effect was clearly visible was 20 degrees. When the side slip angle was 10 degrees the effect was already much less pronounced.

Another thing that was mentioned in chapter 4 was that when the flow is aligned with the ribs there is very little pressure difference between the ribs and the cell centers. In other words: the pressure on the wing is as if the wing has a uniform shape. Figure 7.6 shows the isobars on the top surface.

A number of things catch the eye:

- First of all, the chaotic isobar pattern near the leading edge. This can be attributed to the non-uniform curvature on the nose.
- In figure 6.8 it was shown that ribs 1 and 4 have a dent in the upper surface just behind the leading edge where the V-tapes attach to the ribs. Figure 7.6 shows now that this local decrease in curvature results in a zone of relative high pressure and a loss of lift.
- Between 20% and 50% chord the isobars run nearly straight across the wing. There is very little deformation of the isobars that can clearly be attributed to the different airfoil shape at the ribs and the cell centers.
- On the aft 1/3rd there is a region of relatively high pressure where the isobars are spread wide apart. This is the region behind the kink in the wing that was shown in figure 6.16. It confirms that the flow is separated in that region. When the flaps of the kite would have been open the area of this region should be reduced.

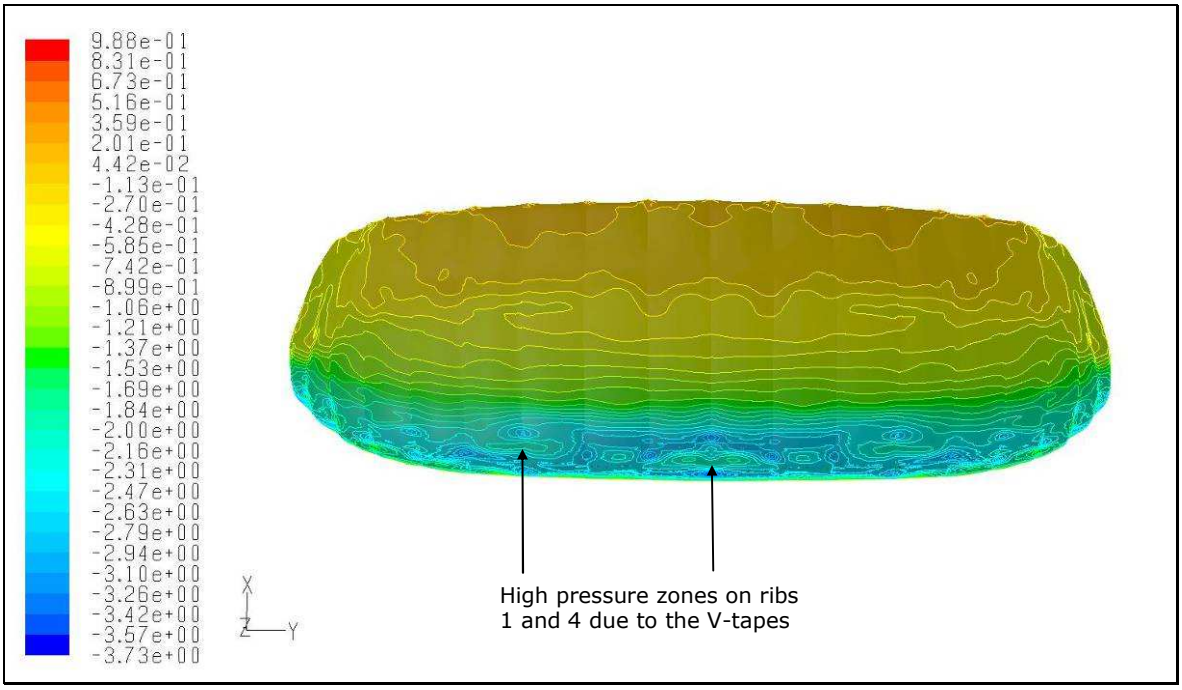

Figure 7.6: Isobars (pressure coefficient) on the top surface of the wing at high angle of attack at 16m/s.

From figure 7.5 and 7.6 it can be concluded that there will only be a spanwise pressure gradient between the ribs and the cell centers when the flow crosses the ribs at a sufficiently large angle or when there is a sufficiently large difference in surface curvature between the rib and the cell centers. A topic for further research can be how large this curvature difference must be to cause an appreciable difference in pressure. Another interesting point is what the 'average' pressure distribution is that the wing will experience compared to the 2D pressure distribution of a cell center airfoil and a rib airfoil.

7.3 Effects of the leading edge deformation

In the last paragraph it was already briefly mentioned that the non-uniform curvature near the leading edge of the kite, which was also discussed in paragraph 6.3, leads to a very chaotic isobar pattern just behind the nose of the kite. The pull of the suspension lines on the lower side of the ribs and the especially the V-tapes, where they connected to the upperside of the ribs, cause a reduction of the curvature on the nose of the wing. This decrease in curvature causes a local pressure increase at that point of the kite where it normally produces the most lift.

Taking a cross section of the pressure contours at rib1 and cell center1 gives the pressure plot shown in figure 7.7. A large dent in the under pressure is present in between 5 and 15% chord.

Looking at figure 7.6 and 7.7 one can see that there is a loss in pressure along the entire leading edge with high pressure spots on the nose of every cell. With a rough estimate one can say that C_P increases by 1 on about 10% of the chord length. If there is an increase of 1 in the Cp value that means an increase of 1x the dynamic pressure. If this happens on 10% of the chord length along the entire span of the wing this means reduction in lift of:

10% x projected wing area x dynamic pressure = 0.1 x 4.15 x 132.8 = 55N

On the total lift of 708N this is a loss of almost 8%. It would be safe to say that more than 5% of the lift is lost here.

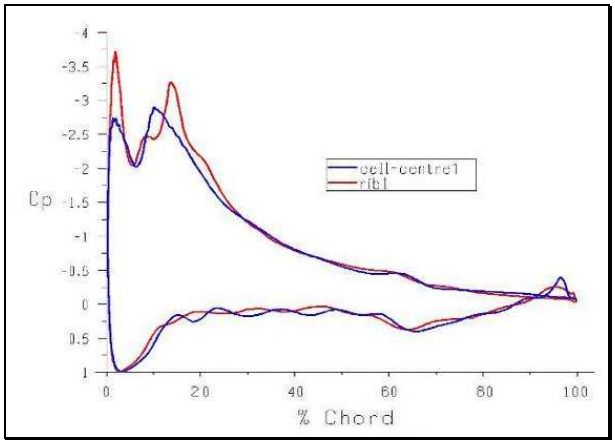

Figure 7.7: Pressure distribution on rib 1 and cell center1 of the kite at high angle of attack at 16m/s.

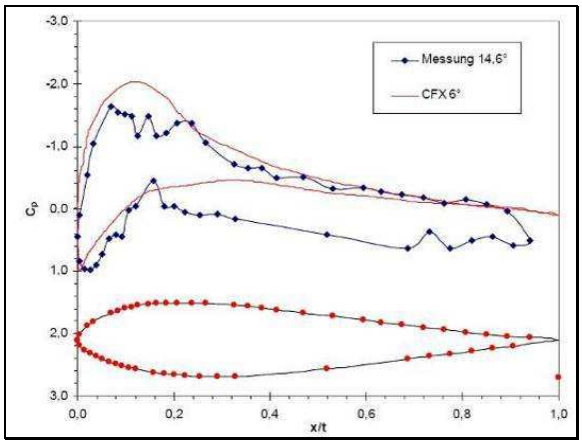

Figure 7.8: Measured and calculated pressure distribution on a kite airfoil. [21]

Such a loss of lift on the nose was also measured by Miller [21] with pressure taps on a similar kite in the windtunnel. His CFD calculations were based on an undeformed geometry. That is why he noticed a significant difference in pressure distribution between the CFD model and the real kite, see figure 7.8. Even though the airfoil shape and CFD results in figure 7.7 and the pressure measurements in figure 7.8 are obtained from different kites, there is more similarity between those two than between the pressure measurements and the analysis of an 'ideal' airfoil shape in figure 7.8. It is to be expected that by taking both pressure measurements and doing a CFD calculation with a measured shape of a kite a much better agreement between CFD and windtunnel data can be obtained than the result shown in figure 7.8.

In the low angle of attack case the loss of lift at the nose is also present, see figure 7.9. In principle a reduction in lift is not bad in this situation because when the brake lines of the kite are released the kiter wants to feel a reduction in lift. The important point is where the lift reduces on the kite. A reduction of lift on the nose of the kite or a larger nose-down moment may make it more prone to collapsing. If the kite would experiences a local negative lift force on the nose, the leading edge would fold down and the kite would collapses.

A cheap and light solution to the problem of the flattening near the nose could be to increase the thickness of the wing locally by adding material to the top side of the rib to bring it back into its original shape. Right now the ribs have a very good shape when they are unloaded and a very bad shape when loaded. By using local finite element analysis or by analyzing the shape of a prototype kite the ribs can be made such that they have a very bad shape when unloaded but that they take their desired shape when loaded in a certain flight condition.

The low angle of attack causes also more suction at the bottom of the airfoil. In the high angle of attack case the minimum C_P value on the bottom surface is around 0. In the low angle of attack case this is around -0.5. This also causes a reduction in lift, especially on the nose. As shown in figure 6.13 the trailing edge of the center of the wing is bent down in the low angle of attack case. The effect of that is that there is a 30% increase in pressure difference between the top and bottom surface at the kink. This, combined with the reduction in lift on the nose, may lead to an unwanted nose down moment on the kite.

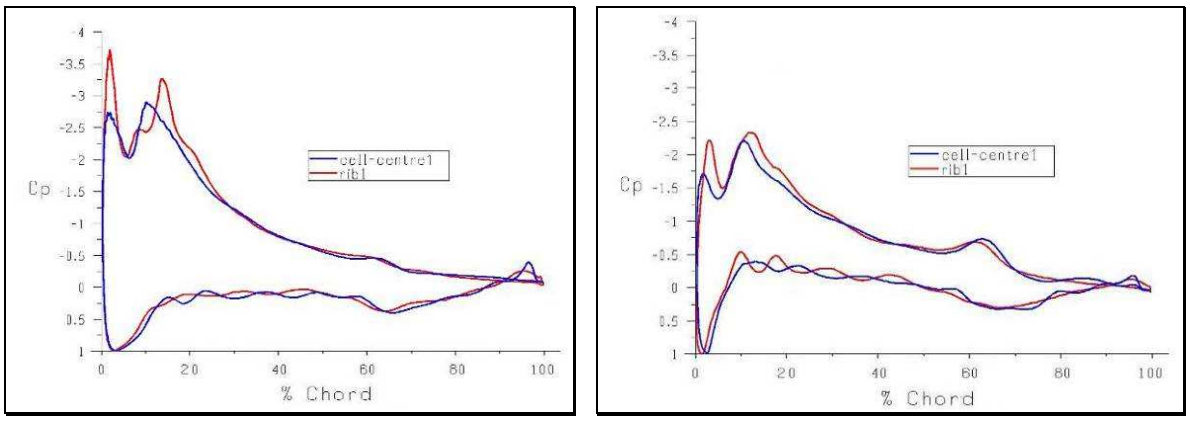

Figure 7.9: Left: Pressure distribution on rib 1 and cell center1 of the kite at high angle of attack at 16m/s (same as figure 7.7). Right: distribution on rib1 and cell center1 of the kite at low angle of attack at 16m/s.

7.4 Lift distribution for minimum induced drag

Figure 6.4 showed the angle of attack distribution of the three different cases. It was noted that in the high angle of attack case the outer four cells cells of the kite are at an angle of attack that is likely beyond the stall angle. The reason that this angle is so high is because the drag that the stalled tip cells is used to steer the kite. Figure 7.10 confirms the suspicion that the outer cells are stalled. It shows a large volume on the outer four cells where the energy in the flow is dissipated. This indicates very turbulent air that is the result of flow separation.

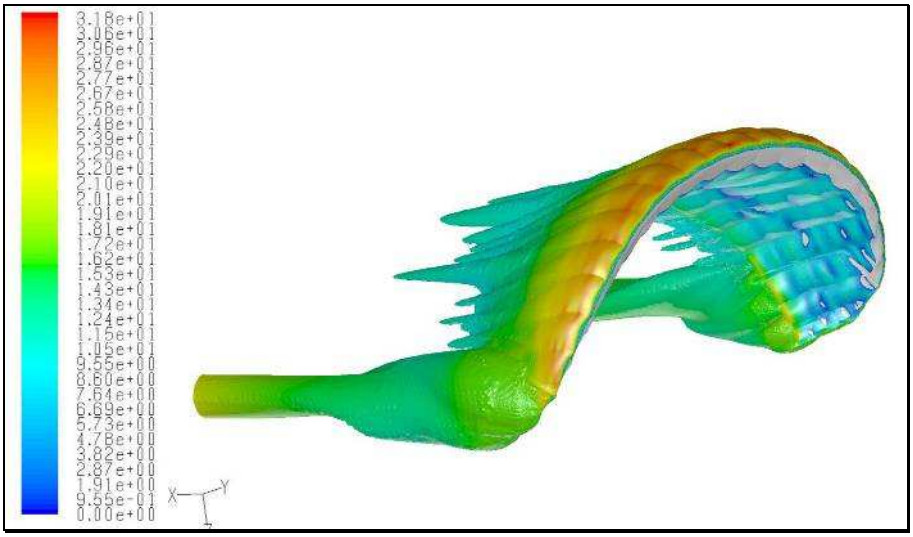

Figure 7.10: Iso-surface of the total pressure = ½ times the dynamic pressure. Colored by velocity magnitude [m/s]. High angle of attack at 16m/s.

Figure 7.11 shows the same situation for comparison, but then for the case of minimum angle of attack. The energy dissipation at the tip is much less.

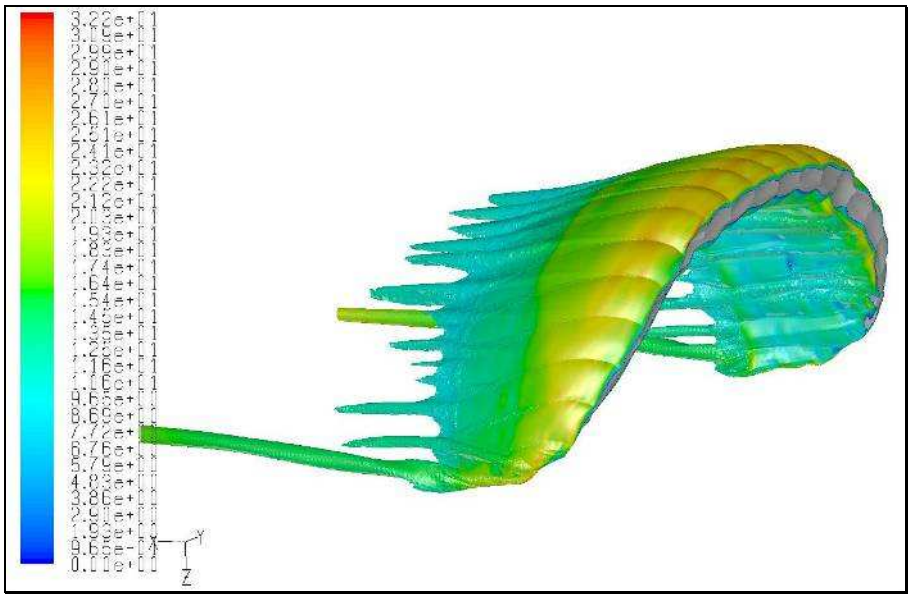

Figure 7.11: Iso-surface of the total pressure = ½ times the dynamic pressure. Colored by velocity magnitude [m/s]. Minimum angle of attack at 16m/s.

Because the kite geometry in the CFD model consists of ten individual cells the lift and drag of each cell can be computed individually. The first point of interest is to see how the local angle of attack of each rib corresponds with the local lift coefficient of each cell.

This relation is plotted in figure 7.12a, b and c. The blue/diamond line shows the angle of attack distribution of all the ribs as plotted in figure 6.4. The magenta/square line shows the local lift coefficient of each cell. The area of a cell is the plane that connects the two chord lines of the two bounding ribs of a cell. The span is measured along the camberline of the wing. The green/triangle lines shows the local projected lift coefficient of the cells. This is the Z-component of the lift coefficient. The projected areas of the cells are the areas of the magenta/square line projected in the XY-plane. The span is measured along the projected span.

The figures show that the lift coefficient is relatively constant along the span. In the high angle of attack case the lift coefficient drops near the tips. This can be attributed to the high angle of attack that stalls the wing tip. The lift coefficient projected in Z-direction is much larger near the tip. This happens because the surface area of the tip cell is taken as the plane that connects the chord of rib10 with the tip. The projected area of this plane onto the XY-plane is very small. This makes the lift coefficient seem larger than expected.

In classic aerodynamics it is always taught that an elliptical lift distribution causes the least amount of induced drag. Given that the kite operates at relatively high lift coefficients, the induced drag will probably form a major part of its drag. So an interesting question is: how close is the lift distribution of the kite near the elliptical lift distribution?

The next question is then: what should be elliptical with respect to what? Figure 7.13 shows a dotted line that represents a quarter ellipse. Also plotted is the total lift: the lift force on each cell plotted against against the distance measured along the wing camber line. The next line shows the Z-projection of the lift force plotted against the distance measured along the projected span. Both result in nearly the same distribution that is also very close to the elliptical distribution. But the theory of the elliptical lift distribution was developed for planar wings.

In 1962 Clarence Cone of NASA [7] wrote a report about the induced drag of non-planar wings based potential theory. In his definitions he plots the total lift, but measured along the projected span. The same graph is given in figure 7.13 by "Total lift on projected span". This shape is quite different from the elliptical distribution.

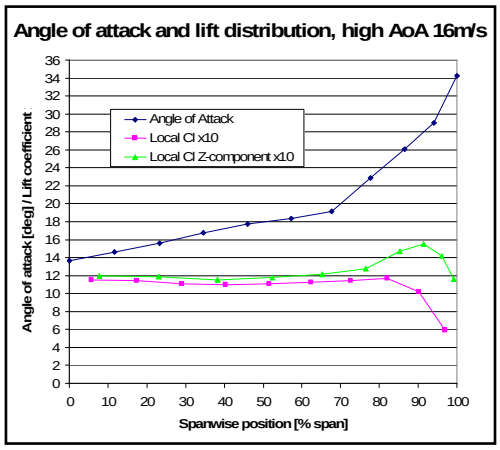

Figure 7.12a: Angle of attack of the ribs and lift coefficient of the cells.

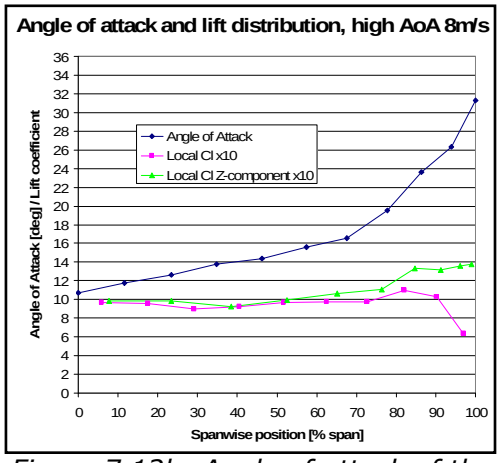

Figure 7.12b: Angle of attack of the ribs and lift coefficient of the cells.

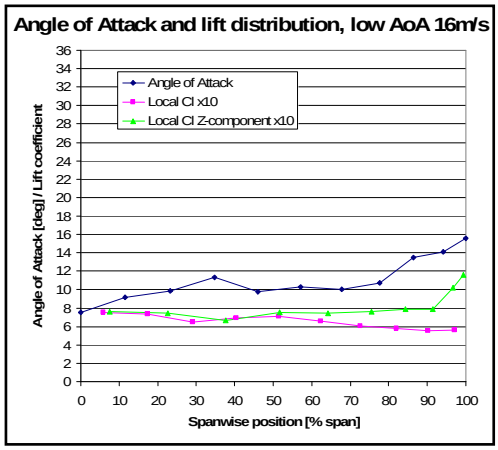

Figure 7.12c: Angle of attack of the ribs and lift coefficient of the cells.

Cone found that every non-planar shape has its own lift distribution that results in minimum induced drag. Two shapes are well documented in his paper: the circular arc and the semi-elliptical camber line. He shows the induced drag of these wings compared to the induced drag of a planar wing with an elliptical lift distribution. The ratio between these two depends on how far the non-planer wing is bent out of plane. This is defined by the camber factor: the ratio between the out of plane deflection and the semi-projected span of the wing (see figure 7.15). For the kite this is 0.73. The shape of the camber line of the kite is something in between a circular arc and a semi-ellipse.

Figure 7.14 shows the lift distribution, represented by the circulation, of the three kite models together with the ideal lift distribution according to Cone for a wing with a camber factor of 0.73. For completeness also the elliptical distribution is shown.

For minimum induced drag the lift distribution of the kite should be in between the distribution of the circular arc and the semi-ellipse. In the low angle of attack case the lift is too low in between 20% and 50% span and too high from 60% to 100% span. In the high angle of attack case the lift is too high from 45% to 100% span. This means that the induced drag can be reduced by changing the lift distribution.

One thing that stands out very clear is the dip in the lift on cell3 in figure 7.14. Looking back at figure 6.17 one can see that there is extreme ballooning on the lower side of cell3 compared to the other cells. Apparently, cell3 deforms more than the other cells at the cell center. This may cause the decrease in lift.

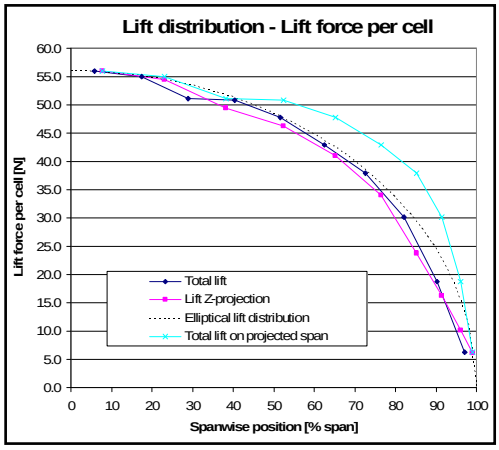

Figure 7.13: Lift per cell as a function of span. High angle of attack at 16m/s.

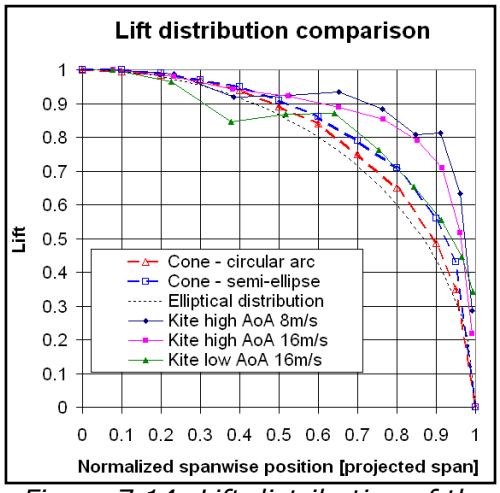

Figure 7.14: Lift distribution of the kite compared to the "ideal" lift distribution according to Cone [7].

Cone also presents the efficiency of the circular arc and the semi-ellipse (represented by the efficiency factor k, which is in fact the Oswald factor) as a function of the camber factor β. This is shown in figure 7.15. It shows that, given that the kite has a camber factor of 0.73, the efficiency factor of the elliptical arc is 0.15 higher than that of the circular arc, an increase of 11.7%. This holds when both wings have the same projected span and produce the same projected lift (the force in Z-direction).

Because Cone's theory is based on potential theory it treats only the induced drag and not the profile drag. When two wings have the same projected span and camber factor but one wing has a circular camber and the other a semi-elliptical camber then the wing with the semi-elliptical camber has a longer arc length. This increased arc length adds to the profile drag of the wing. The difference in arc length of a circular arc and a semi-ellipse is 2.7% when the camber factor is 0.73.

From the foregoing it seems that when induced drag is the dominant drag factor of a wing it is beneficial to have a semi-elliptical camber instead of a circular camber. The shape of the kite is something in between a circular arc and a semi-ellipse. Based on Cone's theory it can be expected that when the spanwise camber is changed into a pure semi-ellipse that the induced drag of the kite decreases.

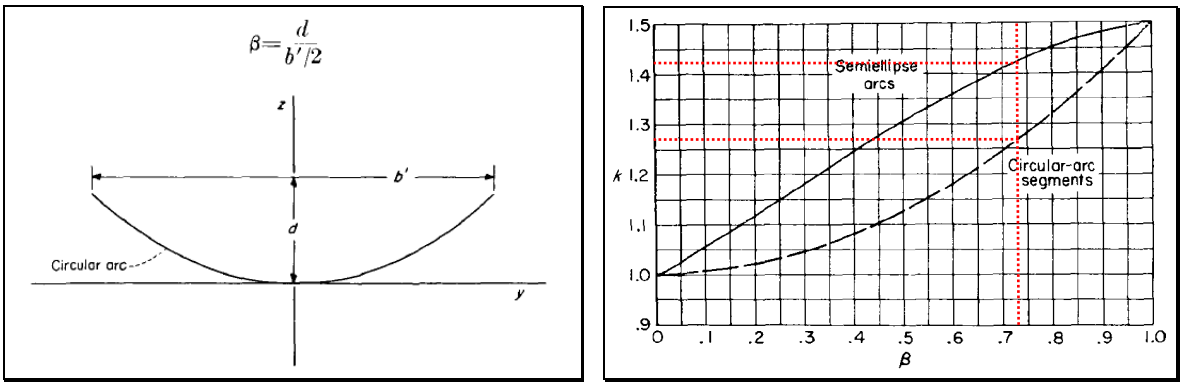

Figure 7.15: Maximum efficiency factor or Oswald factor (k) for different camber factors (β) for wings having circular or semi-elliptical camber. [7]

The maximum efficiency that is shown in figure 7.15 assumes that there is an ideal distribution of the wake normal velocity behind the wing. According to Cone the normal velocity in the wake must be proportional to cos(τ), where τ is the local anhedral angle (camber angle) of the wing.

The shape of the wing is very non-uniform due to the ballooning. This has consequences for the shape of the wake. Figure 7.16 shows the magnitude of the velocity component normal to the freestream velocity directly behind the wing. It shows a very non-uniform distribution of this velocity. This ragged wake shape deviates from the ideal distribution. Because of that it can be expected that the ballooned wing can't reach the maximum efficiency factor of figure 7.15, apart from the other assumption of the potential flow model.

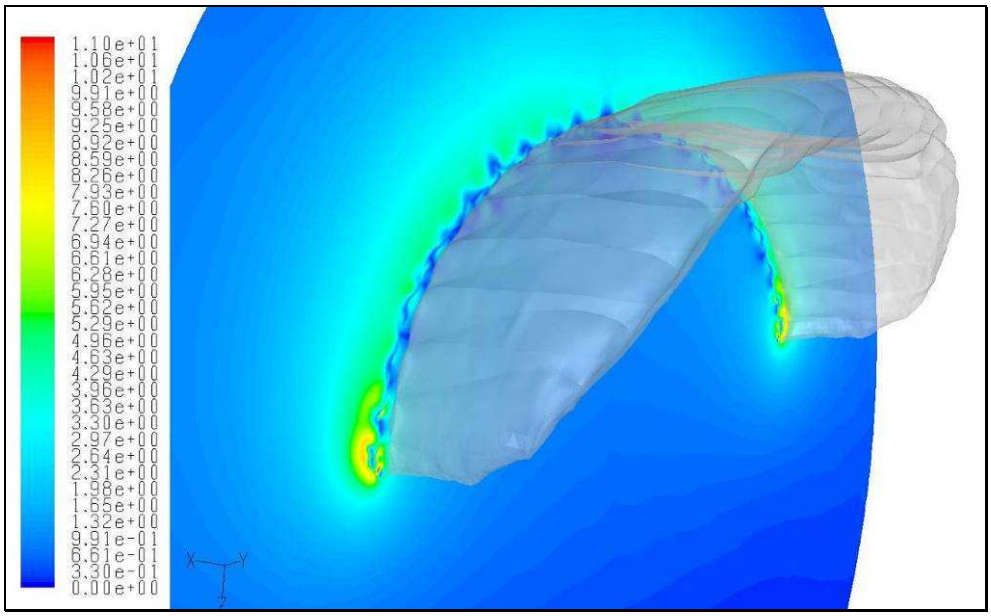

Figure 7.16: Velocity magnitude [m/s] of the velocity component normal to the freestream velocity. The normal velocity is very non-uniform behind the wing.Wing at low angle of attack at 16m/s.

7.5 Drag distribution

As is common with CFD and as was shown in chapter 4 drag is usually over estimated by CFD, especially when larger areas are covered with separated flow. However, looking at the measured and calculated drag in table 7.17 one can see that the drag of the kite with CFD is lower than in the windtunnel. This could be expected because both the wrinkles in the fabric and the line cascade were left out of the numerical simulation. They would significantly increase the drag.

The lift values are much more realistic. Given that the kite model was surrounded by a simplified model of the windtunnel and that there were no wrinkles in the fabric and no tripods standing in front of the kite to fix it, a maximum error of 12.9% is not an unexpected result.

Tabel 7.17: Measured and calculated lift and drag.

	Lift [N]		
Case	Windtunnel	CFD	Difference %
High AoA - 8m/s	163	144	12.9
High AoA - 16m/s	708	675	4.9
Low AoA - 16m/s	479	425	12.6

	Drag		
Case	Windtunnel	CFD	Difference %
High AoA - 8m/s	28	21	32.1
High AoA - 16m/s	125	105	18.6
Low AoA - 16m/s	59	47	26.1

	L/D		
Case	Windtunnel	CFD	Difference %
High AoA - 8m/s	5.8	6.8	17.0
High AoA - 16m/s	5.7	6.4	13.1
Low AoA - 16m/s	8.1	9.1	12.0

Figure 7.18 shows the drag coefficient of each individual cell based on the projected area of the kite. This shows first of all that the pressure drag is much larger than the viscous drag. Viscous drag, or friction drag, has mostly to do with attached flow and the formation of a thin wake. It depends mostly on the area that is exposed to the airflow. That is why the viscous drag has a more or less elliptical distribution like the surface area of the wing. Pressure drag is mostly associated with separated flow and a very thick wake. A very slick aerodynamic design such as a sailplane experiences mostly viscous drag. A more blunt object like a passenger car experiences mostly pressure drag.

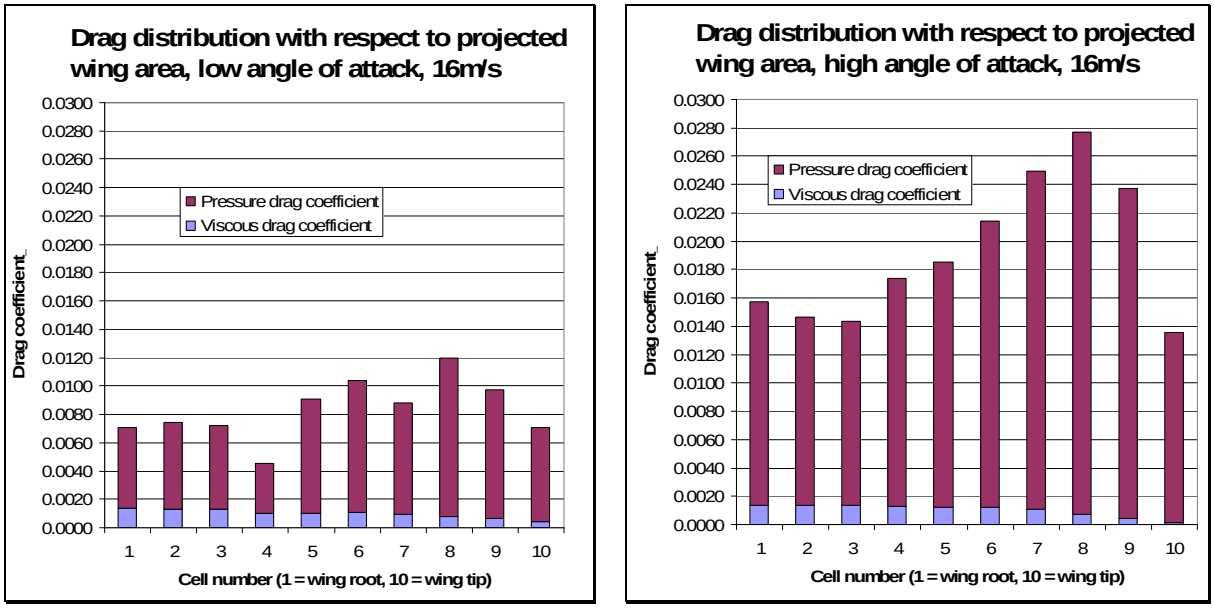

Figure 7.18: Drag coefficient per cell based on the projected area of the wing. Drag coefficients can be added to obtain the total drag coefficient.

Even at low angle of attack the pressure drag on the kite is several times larger than the viscous drag. This shows that the kite has a very crude aerodynamic shape. The ratio between viscous drag and pressure drag is more like that of blunt body than that of a high performance wing.

Figure 7.18 also shows that the drag on cell8 is the largest. The cells further inboard have a lower angle of attack and lower lift coefficient. This translates directly into a lower drag. The two cells further outboard are much smaller and thus have a proportionally smaller drag.

The high drag on the tips is useful for steering the kite. But when the angle of attack of the kite is increased symmetrically to increase the pulling force, the stalling tips cause the kite to slow down unnecessarily, as if the kite is being choked. In the right graph of figure 7.18 47% of the drag is caused by the outboard four cells while they only represent 25% of the wing area. If the action that changes the angle of attack would be controlled separately from the steering action the kite could fly faster, and in that sence more efficiently, at high angle of attack. This can be an important point when such a kite is used for power generation, but it could also give kite surfers a stronger pull and higher jumps.

7.6 Conclusion form the CFD analysis

The most important conclusion form the analysis in this chapter is that CFD is a very useful tool for analysing the aerodynamics of a ram-air wing. It is invaluable for identifying sources that negatively affect the aerodynamic performance of the wing. The results shown in this chapter show just a fraction of all the data that can be gathered from CFD.

The absolute lift and drag values of the CFD simulations differred mostly more than an exceptable 5% error from the measured values in the windtunnel. But this was expected based on the assumptions of the CFD model.

Other conclusions about the aerodynamics of the ram-air wing are:

- The "flow fence effect" of the grooves in the wing when flow crosses from one cell to another is less than expected. At low angle of attack the crossing angle is mostly too small to generate the effect. At high angle of attack large parts of the flow are separated and this prevents the development of the flow fence effect.
- There will only be a spanwise pressure gradient between the ribs and the cell centers when the flow crosses the ribs at a sufficiently large angle (>10 degrees) or there must be a sufficiently large difference in surface curvature between the rib and the cell centers.
- The uneven curvature on the nose of the wing is likely to cause more than 5% loss of lift compared to a situation where the nose would have the curvature as intended by the designer. Major sources of the curvature change on the nose are the attachment points of the lines on the under side of the nose and the attachment of V-tapes inside the wing.
- Changing the shape of the ribs in the nose area could bring back the desired curvature. This requires an extra iteration in the design process where the shape of the ribs in flight is analysed. Where dents in the wing profile appear in flight the shape of the ribs can be adapted to change the local surface curvature.
- The kink that is present in the wing at around 60% chord causes unwanted lift and an unwanted nose-down moment at low angle of attack.
- The global spanwise lift distribution of this wing deviates from the theoretical optimal lift distribution that minimizes induced drag.
- The spanwise camber of the wing is something in between a circular arc and a semi-ellipse. By changing the spanwise camber of the wing into a pure semi-ellipse a reduction of the induced drag of several percent may be expected. Because the kite operates at high lift coefficients where induced drag is a dominant factor also a reduction in the total drag may be expected.
- The drag comprises mostly of pressure drag and only a small amount is viscous drag. This is similar to the drag ratio of a blunt body. That means that flow separation is an important source of drag on the wing.
- The stalling tips limit the speed that the kite can develop at high angle of attack. Separating the steering control from the angle of attack changing control can give the kite more speed and a stronger pull at high angle of attack.

8 Conclusions and recommendations

To recapitulate from the introduction:

The goals of this thesis were to be able to point out where a ram-air wing departs from the intended design shape, to investigate how well the kite performs, to understand how the deformations affect the airflow and to make suggestions for possible improvements of the design.

This report presented a method to analyse the shape and the aerodynamics of a ram-air kite. The kite was tested in the windtunnel. Its shape was captured using two techniques: photogrammetry and laser scanning. Using the geometry data the structural deformation of the wing was dissected. With computational fluid dynamics the aerodynamics of the deformed shape was analyzed. These were the first steps of a reverse-engineering process with which the shape and aerodynamics of a ram-air wing can be improved. The last steps of this process, actually making changes to the construction of the kite and testing the effects, was not part of this thesis. An extra result of this study was the comparison of photogrammetry and laser scanning in terms of their suitability to capture the 3D shape of the ram-air kite.

Chapter 5 showed how the kite performed in the windtunnel in terms of lift and drag. In chapter 6 four different geometries of the kite in the windtunnel and the designed geometry of the manufacturer were compared with one another. Chapter 7 showed the results of computational fluid dynamics (CFD) analysis on the kite and several suggestions were given that can improve the aerodynamics of the kite.

As a method for reverse-engineering a ram-air wing the process that is described in this report works very well up to the CFD analysis. Specific deviations from the intended design shape are clearly visible. The entire design cycle can be completed by applying the proposed changes to the geometry of the kite and by testing the kite. But this is left for future work.

The following conclusions were drawn from the geometry analysis and the CFD analysis of the five different kite models:

- The CAD model form the manufacturer contains no ballooning. The real kite has a maximum deformation at the cell center of around 5% of the chord length. This is a relative increase of the profile thickness ratio of 28%.
- On most of the chord length this thickness increase is more than twice as much on the bottom surface as on the top surface.
- Theoretically the grooves in between the ballooning can prevent the flow from moving at an angle with respect to the tips, as was shown in chapter 4. In practice this effect only happens by a small amount on the outboard cells. The effect is only clearly visible when crossing angle is well over 10 degrees.

- The manufacturer's model is an 'average shape' of the kite that it has when the brake lines are not fully pulled but also not fully released. Between maximum and minimum pull there is a large change in angle of attack of the ribs (more than 4^{o} at the root), especially near the tips (more than 10^{o}).
- The kite is designed to fly at high angle of attack (above 10 degrees). Below that angle the stagnation point is not on the air intakes in the nose. Because of that the kite looses internal pressure and large dents appear in the nose of the kite.
- Dispite these dents the kite obtains its best lift-to-drag ratio when the brake lines are completely released.

- At the top surface the wing profile flattens at spots that are directly above the attachment points of the bridle lines on the lower surface or above the attachment points of the V-tapes. This is most pronounced just behind the leading edge.
- The flattening is also present at the cell centers.
- The decreased curvature on the nose results in a decrease in total lift of more than 5%.
- The flattening of the profile is also present near the lines that are attached to the middle of the chord.
- By not trying to stiffen the ribs but by adding material to the place where they flatten the upper surface curvature can be restored in a relatively simple way. This should remove the high pressure spots in the flattened areas.

- The tension that is build into the leading edge by narrowing the fabric panels there pulls down the leading edge and changes the shape of the spanwise camber line.

- A stiff tape in the trailing edge causes a deformation of the trailing edge camber when the brake lines are released. The consequense is that when the angle of attack is reduced the aft part of the center of the wing is pulled down like a flap.
- The flap like motion causes a 30% increase in pressure difference across the top and bottom surface at the hinge point at round 60% chord. This causes an unwanted upward force and nose-down moment.

- There is a kink in the wing at around 60% chord. This kink is hardly visible in real flight but it is very well visible in the photogrammetry models.
- The kink is most likely caused by increased surface tension in the fabric at that location because of the flaps that are built into the wing.
- Flow separates at the kink.

- The spanwise camber of the wing and the shape of the ballooning of the cells only undergo a minor deformation when the wing loading is quadrupled. Much more important is a deformation due to a change in the brake position.

- Wrinkles in the top and bottom surface compress the ribs in chordwise direction. This compression and wrinkling makes the ribs approximately 3.5% shorter. This reduces the area of the wing and it makes the airfoils effectively thicker.

- At low angle of attack the lift distribution of the kite is quite close to the ideal lift distribution that minimizes induced drag. At angles of attack higher than the minimum angle of attack the lift distribution is far from the ideal angle of attack. Changing the lift distribution can reduce the induced drag of the kite.
- Changing the kite's spanwise camber into a pure semi-ellipse could further reduce the induced drag.

- The stalling tips limit the speed that the kite can develop at high angle of attack. Separating the steering control from the angle of attack changing control can give the kite more speed and a stronger pull at high angle of attack.

- Noticable wall effects were experienced in the windtunnel. These wall effects affect the load distribution of the kite. This in turn also changes the shape of the kite. This change is mainly found in a slight change of the spanwise camber of the kite. To obtain consistent data between windtunnel tests and CFD also the windtunnel geometry should be incorporated in the CFD analysis.

- Laserscanning is not a very suitable technique to analyse the shape of the kite. The kite moves too much due to its own turbulence and turbulence from the scanner. This causes noise in the scanner data of several centimeters. A technique is needed that instantly captures the shape.
- Photogrammetry can do exactly that: it captures the shape of the kite in an instant. With the right setup photogrammetry can reach the same accuracy or better when capturing a moving object compared to laser scanner capturing a static object.

9 Future work

As said in the introduction the number of publications about ram-air wings is still quite scarce. But as shown in chapter 3 there is an ever growing industry that specializes in designing and building these wings. Also power production could be a possible application of ram-air wings. All applications require better handling and better performing ram-air wings for the future. The basis for that is to better understand how these wings deform and how their aerodynamics can be improved.

9.1 Reseach opportunities

Further work based on the data that was gathered in this thesis could be:

- First of all, the amount of data that was processed for this thesis was only a fraction of all the data that was gathered in the windtunnel. Out of the twelve cases that were measured with photogrammetry only three were processed, because generating a 3D model is a time consuming job.
- The outer cells of the 3D models can be studied in more detail. The focus of this thesis has been mainly on the center section of the wing. But the cross section and curvature analysis can also be done on the outboard cells.
- To confirm that the difference in camber between the laser scan and the photogrammetry is indeed due to wall effects a new CFD case must be run with the kite at low angle of attack and no walls near the kite. This should confirm that at low angle of attack the tips of the kite experience a lower loading when the walls are further away from the kite.
- Adapt the real wing based on the data from this report and measure the difference in performance of the original kite and the adapted kite.

More in general, research that can be done in the field of ram-air wings is:

- Determining what the "average shape" is that the air sees when it flows past a ballooned ram-air wing. Is the static pressure on a balooned wing more like the pressure of the 2D rib or of the 2D cell center or of the average shape of the rib and the cell center?
- Examples of computational fluid-structure interaction (FSI) on ram-air wings are still scarce. As computer clusters become more and more powerful better opportunities appear for using FSI on ram-air wings. One could start with a very simple model consisting of a crude FEM model and a potential flow model. This could already yield acceptable results.
- Futher work out Cone's theory on induced drag of non-planar wings and include viscous drag and pressure drag effects. Develop a tool that can quickly compare the total drag of different wing planforms based on the used airfoils, angle of attack and wing camber.
- Further develop the photogrammetry technique and explore the use in real flight outside the windtunnel. Being able to use this technique outside the windtunnel can save expensive windtunnel time.
- Redo the analysis of chapter 4 for a range of different airfoils, that are used in kites with different ballooning, cell widths, reynolds numbers, etc…
- Further develop thermography for ram-air wings
- A fundamental study of the influence of wrinkles on the boundary layer. This can also include the influence of sewed, glued and welded seams and surface texture.

9.2 Improvements in methodology

With hindsight certain aspects of the methodology could be changed or improved:

- The analysis of chapter 4 could be done with an airfoil that is more common in ram-air wings. For example an MH-91, 92 or 93 are airfoils that are designed for ram-air wings.
-
- The ballooning of non-planar ram-air wings is mostly not equal on the top and bottom surface. Instead of assuming a an even distribution between top and bottom surface the data of chapter 6 can be used as a guide line

- The lift-to-drag measurements of the kite in the BWK windtunnel were based on measuring the total aerodynamic force with a load cell and the attitude of the kite with a digital inclinometer. The accuracy of the lift-to-drag ratio measurements can be improved by using a 3-axis load cell that measures loads in X, Y and Z-direction.

- The accuracy of the photogrammetry can be improved by using different lenses on the cameras. The aim is that the targets on the kite fill the entire image. This improves the quality of the project, but it requires that every lens is calibrated separately. This means more work.

- The system that fixes the kite in the windtunnel can be further developed to minimize to influence of the tripods on the aerodynamics of the kite. There was a standard 3-axis camera head on top of the tripods that must have influenced the aerodynamics on part of the kite. Perhaps this head can be made smaller or a different/better solution can be found.

Literature

[1] Abbot I.H., *"Theory of wing sections"*, McGraw-Hill, 1949

[2] Babinsky H., *"Aerodynamic improvements of paraglider performance"*, AIAA-99-3148/A99-33386, 1999

[3] Babinsky H., *"The aerodynamic performance of paragliders"*, The Aeronautical Journal Vol. 103 Num. 1027, 1999

[4] Benelol S. et al., *"The FASTWing project, parafoil development and manufacturing"*, 18th AIAA Aerodynamic Decelerator Systems Technology Conference and Seminar / AIAA-2005-1639-646, 2005

[5] Boermans L.M.M., Private communication, Aerodynamicist at Low Speed Aerodynamics Laboratory Delft University of Technology, August 2008

[6] Breukels J., Ockels W.J., *"Past, present and future of kites and energy generation"*, 2007

[7] Cone Jr. C.D., *"Theory of induced lift and minimum induced drag of nonplanar lifting systems"*, NASA Technical Report R-139, 1962

[8] Diehl M., *"1st International Workshop on Modelling and Optimization of Power Generating Kites, KITE-OPT 07"*, K.U. Leuven, 2007

[9] Furfaro J. et al., *"An experimental study of parafoil sections"*, AIAA-1997-1527-` 632 / A97-31352, 1997

[10] Harich A., Private communication, Chief designer Flysurfer kiteboarding, August 2008

[11] Hoerner S.F., *"Fluid-Dynamic Drag, theoretical, experimental and statistical information"*, Hoerner Fluid dynamics, 1965

[12] Ibos C. et al., *"Fluid-structure simulation of a 3D ram air parachute with SINPA software"*, AIAA-1999-1713-716 / A99-30935, 1999

[13] Johari H., Desabrais K.J., *"Stiffness Scaling for Solid-Cloth Parachutes"*, Journal of Aircraft Vol. 40 No. 4 / AIAA-3166-891, 2003

[14] Kallinderis Y. et al., *"Hybrid Prismatic/Tetrahedral Grid Generation for Viscous Flows Around Complex Geometries"*, AIAA Journal Vol. 34 No. 2 / AIAA-13063-414, 1996

[15] Lazos B.S., Visser K.D., *"Aerodynamic Comparison of Hyper-Elliptic Cambered Span (HECS) Wings with Conventional Configurations"*, 24th Applied Aerodynamics Conference 2006 / AIAA-2006-3469-968, 2006

[16] Lee C.K., Li P., *"Geometric Properties of Parachutes Using 3-D Laser Scanning"*, Journal of Aircraft Vol. 44 No. 2 / AIAA-18387-413, 2007

[17] Loyd M.L., *"Crosswind kite power"*, Journal of Energy Vol. 4 No.3 Article No. 80-4075, 1980

[18] Luhmann T. et al., *"Close Range Photogrammetry, Principles, Methods and Applications"*, Whittles Publishing, 2006

[19] McCroskey W.J., *"A Critical Assessment of Wind Tunnel Results for the NACA 0012 Airfoil"*, NASA Technical Memorandum 100019, 1987

[20] Menter F.R., *"Improved Two-Equation k-ω Turbulence Models for Aerodynamic Flows"*, NASA Technical Memorandum 103975, 1992

[21] Miller A., *"Numerische Untersuchung der aerodynamischen Kräfte an einem Flügelelement mit unterbrochenem Hinterkantenschlitz*", Universität Stuttgart, 2006

[22] Santos A., *"Superbus Crosswind Sensitivity Analysis",* Delft University of Technology, 2008

[23] Simpson A. et al., *"Flight Control of a UAV with Inflatable Wings with Wing Warping"*, 24th Applied Aerodynamics Conference 2006 / AIAA-2006-2831-682, 2006

[24] Simpson A. et al., *"Aeroelastic Behavior of Inflatable Wings: Wind Tunnel and Flight Testing"*, 45th AIAA Aerospace Sciences Meeting and Exhibit 2007 / AIAA-2007-1069-771, 2007

[25] Wachter de A., *"Design of a spoiler system for paragliders, a new way to descend"*, Delft University of Technology, 2007

[26] Werff van der D., *"Numerical Analysis of the Aerodynamic Improvements for the Spyker C8 Spyder"*, Delft University of Technology, 2007

[27] White F.M., *"Viscous fluid flow"*, McGraw Hill, 2005

[28] *"Fluent 6.2 User's Guide"*, Fluent Inc., 2005

[29] *"Photomodeler Pro 5 Help"*, Eos Systems Inc., 2004

[30] *"Faro Laser Scanner LS product brochure"*, Faro Europe GmbH&Co.KG, 2005

[31] *http://www.cfd-online.com/Wiki/Turbulence_length_scale*

[32] *http://en.wikipedia.org/wiki/Laser_scanning*

[33] *http://www.maxdereta.com*

[34] http://www.youtube.com/watch?v=PmpGeEK8uFc

Appendix A: Introduction to Computational Fluid Dynamics

The intention of this appendix is to give a brief introduction into the working principle of computational fluid dynamics (CFD) for people who are unfamiliar with the technique. By no means does it serve the purpose of giving a complete course, simply because the whole process and underlying theory is too much and too complex to put in this report. Detailed information can be found in the various literature on CFD [14], [20], [26] or one of many others, numerical analysis and in the extensive manuals of CFD software, for example [28].

CFD is solving the mathematical equations that discribe or approximate real flow of fluids or gasses (also referred to as fluids) with computers. Before the actual fluid calculation the geometry that is to be analysed and then the fluid domain around it must be defined first.

Not every geometry can be put in CFD software. A geometry can be too complex and need simplification. Reasons can be that the calculation would be too computationally intensive or because it is impossible to define a fluid domain around the geometry that satisfies the requirements for a good quality fluid simulation. In that case the geometry needs to be simplified or changed to accommodate the CFD analysis. For example, in the study presented in this report the surface wrinkles of the kite and the supporting line cascade were left out the analysis. Also the detailed wall structure of the windtunnel was simplified. To calculate the flow with sufficient detail would require an unrealistic amount of computer speed and memory, at least much more than the available resources permitted.

Once the geometry is completed the volume in which the flow equations will be solved is defined. The viscous fluid flow equations that the CFD software solves are the Navier-Stokes equations. These equations are solved numerically. This means that the domain is devided into small blocks. By taking into account the boundary conditions on the edges of the fluid domain and by balancing what goes in, what goes out and what is produced in every block the final solution, the simulated flow field, is obtained. These blocks of fluid are called cells (these CFD cells have nothing to do with the ten cells that make up the geometry of the wing) and together these cells form a grid or mesh. The surface of the geometry, which is the boundary of the fluid domain, is covered with 2D boundary cells. The volume of the domain is filled with 3D cells. There are different types of cells, shown in figure A.1, that have their own advantages and disadvantages.

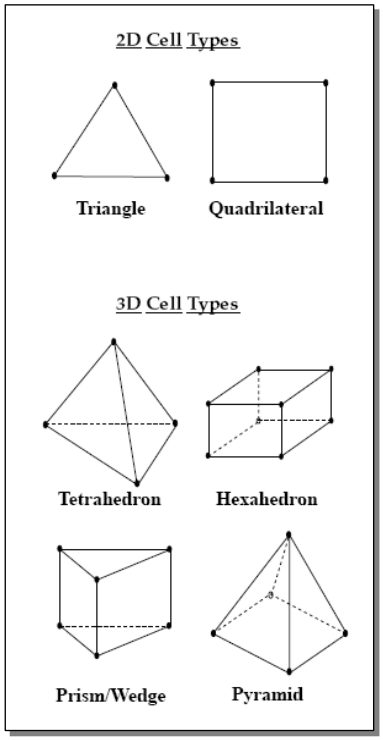

Figure A.1: Different types of CFD cells. [Source: Fluent User's Guide]

The quadrilateral, prism and hexahedron elements form a so-called structured mesh. They are stored in the computer memory in an ordered IxJxK array. The result is relatively little memory consumption and a fast computation time per element compared to the other elements. The trucation error that arises from treating the equations numerically is smaller when the flow is alligned with the structured cells compared to flow through the other types of cells. Another advantage is

that when these cells are used with a very low height to base ratio the truncation error is smaller than for the other elements. On the other hand, a structured grid allows less control over the density of the grid. In case of a complex geometry this may result is much more cells than necessary. This can offset the advantage of reduced computation time per cell by far.

The other types of cells, triangle, tetrahedron, and pyramid, are called unstructured elements. They can be placed with more flexibility around a geometry and with better control over the grid density. The direction from which the flow exits and enters the cells is less relevant. But the trucation error of these cells increases as they become more asymmetric. Also, because the location of the elements is stored in an unstructured way they require more memory and processor time per cell than structured elements.

A combination of structured and unstructured cells is also possible. This is called a hybrid mesh. With a hybrid mesh it is possible to take the advantages of both the structured and unstructured cells. In locations where there are large gradients and the flow direction is known, for example in a boundary layer, structured elements are used. Outside the boundary layer where the grid density can be reduced unstructured elements are used. This results in the typical grid as shown in figure 7.2.

Once the type of grid has been chosen the grid is generated with special grid generation software, in this project ICEM CFD 11. First, the geometry is loaded into the software and it is devided into parts. For each part the cell size and type, structured or unstructured, is prescribed and the place where the volume cells must be made is given. The mesh is generated. In some areas the quality of the mesh may be very low. Running a low quality mesh in the solver program can give large truncation errors and problems with finding one final solution (convergence). For these reasons the quality of the grid must be improved. This is mostly done with grid quality checking and quality improvement options in the grid generator. Once the grid is ready it is exported to a mesh file that can be read by the solver. The mesh file contains only information about the cells. The original geometry is lost and is replaced by 2D boundary cells.

The mesh file is imported in the solver program, Fluent 6.3 in this case. In the solver the individual parts that were defined in the grid generator are recognised. They can now be assigned a certain boundary conditions. Commonly used boundary conditions are: walls, mirror planes, velocity inlets, pressure outlets, fans, porous media and periodic boundary conditions. All of these are described in detail in the Fluent User's Guide [28]. Besides the boundaries also the properties of the fluid are prescribed. Density and viscosity are the most important options.

The basic procedure of any numerical calculation is that it starts with an initial guess of the solution. From this initial guess it results that there is an imbalance in the variables of the equations: the flow velocity and turbulence parameters. From this imbalance a required change of the variable follows. The solution progresses one numerical step by applying the change to the variables. After several of these iteration steps the required change per iteration should decrease. Finally, the solution converges to a point where the changes are negligible.

Before the first iteration step the solver needs an initial guess of the solution to start from. For flow simulations around wings or cars it is often sufficient to assume a uniform flow field that has the same magnitude and direction as the flow that enters through the inlet of the domain. This will result in extremely high lift and drag values for the first few iterations, but they will soon come down and converge to normal values.

Different numerical schemes are available to do the numerical iterations. The most commonly used schemes are 1^{st} order upwind and 2^{nd} order upwind. For a detailed discussing the reader is advised to read any good book on numerical schemes. The largest difference between the two schemes is the round off error. In the 1^{st} order scheme the round off error is one order larger than in the 2^{nd} order scheme. This round off error is also called numerical diffusion in CFD. This is because the round off error has

the same effect as an added diffusion term to the flow equations. The physical consequence of this is that boundary layers become much thicker and that turbulence is dissipated much quicker. Usually this results in unrealistic lift and drag values. The use of the 1st order scheme lies in that this high diffusion also damps the initial wiggles in the solution that are due to the large changes in the solution in the first iterations. Once the solution is past the large changes of the first iterations the numerical scheme is switched to 2nd order. By running the first 5-10% of the iterations with a first order scheme the convergence speed is most of the time increased.

More often than not the change that Fluent proposes for the next iteration overshoots the solution that will lead to convergence by far. The result is that the solution keeps overshooting and never converges. To avoid this problem the program uses so-called under relaxation factors (URF). This allows the user to tell the program which percentage of the proposed change of the solution should really be added in next iteration step. The chosen magnitude of the URFs is a trade off between stability and convergence speed. The higher the URFs the faster the convergence and the sooner the solution is obtained. But this works only up to a certain value. If the URFs are too high the solution "explodes" and diverges to infinity. If the URFs are unnecessary small it will take very long to reach a converged solution. The URF value for minimum convergence time differs from case to case. But generally the more complex a case is the lower the URFs must be.

Once a case is converged it consists of two files. One is the case file, which contains the mesh and all the software settings. The other is the data file, which contains calculated values inside the cells of velocity and turbulence parameters. With these two files a project can be post-processed. This means that all required data is looked up in the data file. Data that is commonly extracted from CFD files are lift, drag, streamlines, cross sections of flow velocity and turbulence intensity, surface pressure and iso-surfaces of total pressure, velocity and turbulence intensity.

Already at the stage where the geometry is created it is good to think about the data that one wants to extract at the end. For example, in case of the kite the kite geometry itself consisted of ten separate cells. This allowed Fluent to give the lift and drag value of each cell separately and that resulted in the graphs of spanwise lift and drag distribution, shown in figure 7.12 and 7.18. Had the kite been just one part then only the total lift and drag could have been obtained.

Appendix B: Introduction to laser scanning

Paragraph 5.3.1.3 already gave an overview of a number of common laser scanning techniques. This paragraph deals with the technique that was used in this project: phase difference laser scanning. The scanner that was used was a Faro laser scanner LS420.

The Faro laser scanner LS works in the following way [30]: It sends an infrared beam into the center of a rotating mirror. This deflects the laser on a vertical rotation around the environment being scanned, the beam is then reflected back into the scanner and the "phase shift" of the invisible infrared beam is measured giving the distance of the laser from the object. Using encoders to measure the mirror rotation and the horizontal rotation of the Laser Scanner, the X,Y,Z coordinates of each point can be calculated. Once a scan has been made the user can easily navigate a 3D view where the entire scan data can be inspected and analysed.

To measure distance the laser scanner uses "phase shift" technology as opposed to "time of flight" distance recording. This means that instead of a single pulse being reflected and the time of flight being measured, constant waves of varying length are projected. Upon contact with an object they are reflected back to the scanner. The distance from the scanner to the object is accurately measured by measuring the phase shifts in the waves of infrared light. The laser scanner splits the laser beam into 3 component parts operating on three different modulation lengths 76m, 9.6m and 1.2m, as shown in figure B.1.

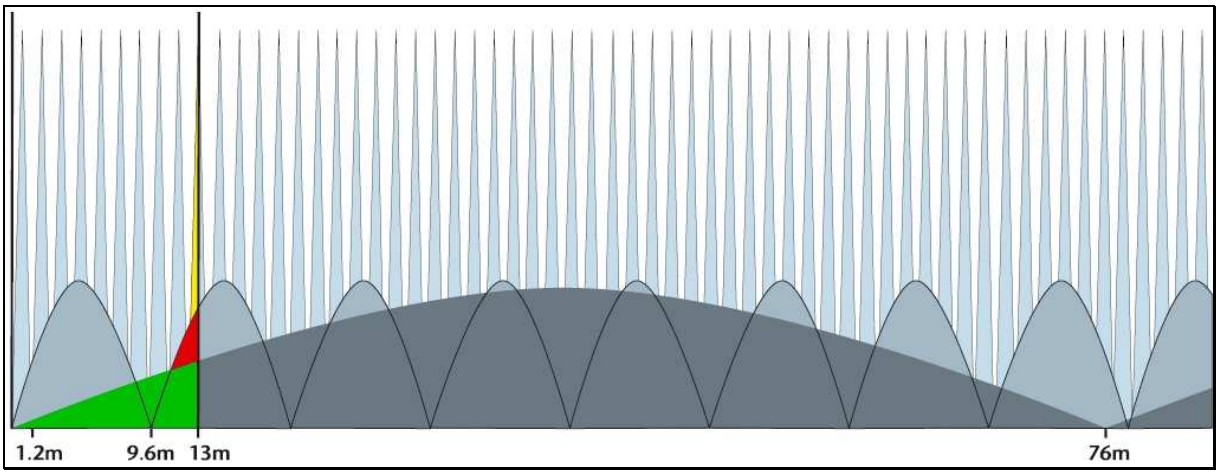

Figure B.1: Distance measuring with a Faro LS scanner. Three light beams with different wave lengths are used to measure the distance to an object. [Source: Faro].

The distance of the reflecting object from the scanner is determined by identifying the location of the reflection in the 1.2m cycle. Firstly, the cycle the reflection occurred on has to be identified, because at the beginning of each cycle the distance reading will start over again. That is, a distance of 2m measured only on the 1.2m modulation would only read as 0.8m as the measurement was in the second cycle but there is no longer modulation length to indicate this. This is known as unambiguity. For example a reflection from 13 meters will register within the 76m range as shown by the green area on the diagram. This is within the second cycle of the 9.6m range as shown in red, and the accuracy is achieved by measuring in the 2nd cycle of the 1.2m range after the beginning of the second cycle of the 9.6m range in yellow. Due to the 76m modulation length the laser scanner is capable of measuring up to 76m without inambiguity.

In order to capture objects out of the line of sight of the laser scanner, registration spheres can be placed within the area to be scanned and the scanner repositioned. Scans from a different viewpoint can then be taken. Once complete the registration spheres can be recognised within different scans and the scans linked together to complete the 3D image.

It takes five different scans to be able to see every part of the surface of half the kite. To be able the see the entire kite takes seven scans. It was only a small amount of extra work to record the other half of the kite also, so contrary to the photogrammetry with laser scanning the entire kite was captured.

The seven scans then need to be put together to give the complete point cloud of the surroundings. This is done with the use of registration spheres. The registration spheres needed to be carefully positioned in the windtunnel, figure B.2. In every scan at least three of the five reference spheres needed to be visible for the scanner to define the orientation of the scan. More visible spheres lead to higher accuracy in the orientation of the scan. Other criteria for placing the spheres are that the spheres should be placed far apart and that every three spheres should form a triangle that is as close as possible to an equilateral triangle. These two criteria make sure that when there is an error in marking the registration spheres that the orientation of the scan is only slightly affected. For example, if three spheres are almost in one line and there is a small marking error of one of the spheres this will give a large angular error in the orientation of a scan. There is of course a trade off between the number of spheres that are visible in each scan and in how far the spheres form equilateral triangles.

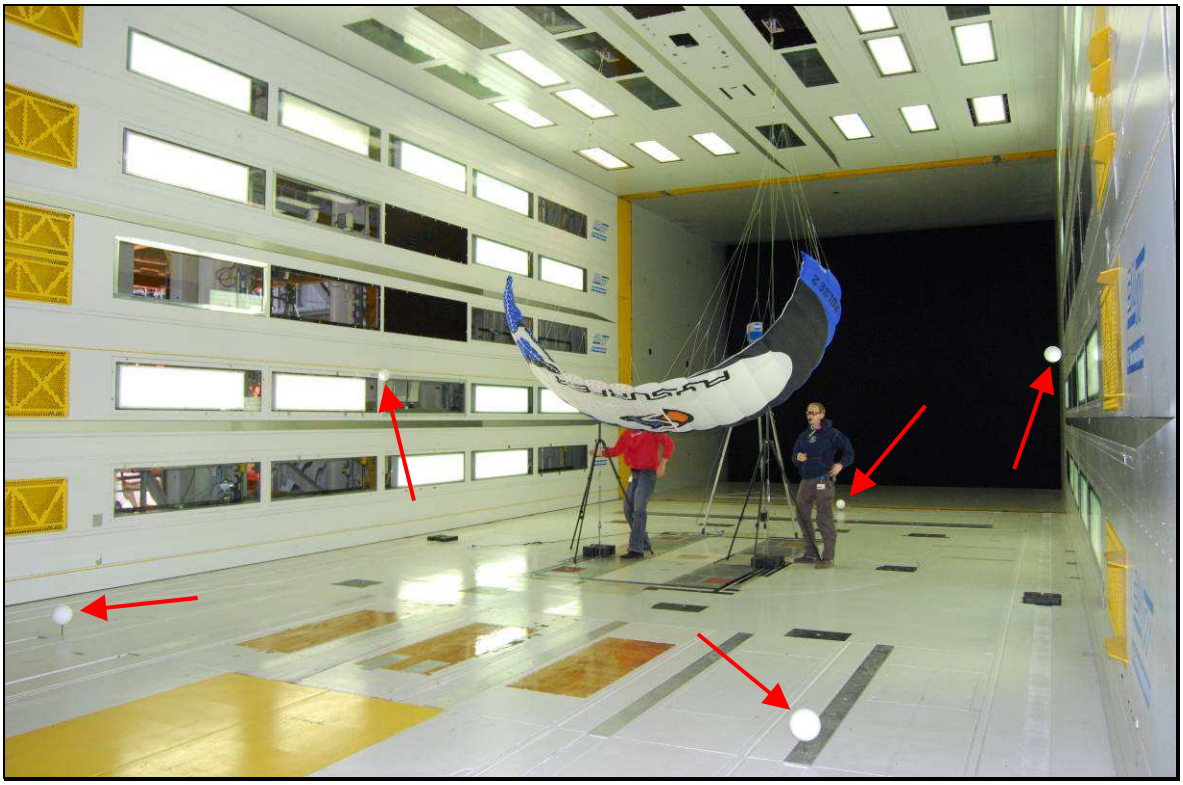

Figure B.2: The registration spheres placed in the windtunnel.

A completely different requirement is that the viewing angle between the scanner and the scanned surface should not become too small. When the laser scanner scans a surface at a 90° angle the laser beam is a round dot on the surface and this gives a high accuracy. The lower the viewing angle becomes the more elliptical the laser dot becomes. Close to 0° viewing angle the scanner can produce very large errors because for a single orientation it receives varying range data. Scanning the complex curved surface of the kite will always give such errors near the edges of the kite. To have a good view of the side of the kite where the suspension lines are attached (the upper side in the windtunnel, the under side when the kite flies normally) the scanner needed to be mounted at a high point. The most straight forward way is to put it on a high tripod. Usually laser scanners or other land surveyor instruments are not used in very windy conditions. So the 3m tall tripod that was available for the laser scanner was made of light weight but very flexible aluminium. If the frame would vibrate in the windtunnel this would introduce an error in the measurement. Therefore, a custom, much stiffer, steel frame was welded together to support the scanner.

It was also considered to mount the scanner upside down on the ceiling. But that plan was rejected because it would be too time consuming to mount it there and take it down again, because it would be too dangerous (risk that the scanner would fall) and because it was unknown if the scanner would work properly when it is held upside down.

Putting the scanner on a tall frame introduced two other problems. One was that at 16m/s the pressure of the wind was large enough to push over the 3m tall, 30kg weighing tripod with the 14.5kg weighing scanner on it. This was solved by adding another 10kg weight to the upwind leg of the tripod. The next problem was that the pressure of the wind was still large enough to make the tripod slide over the windtunnel floor. This was solved by putting thin rubber pads under the legs of the scanner.

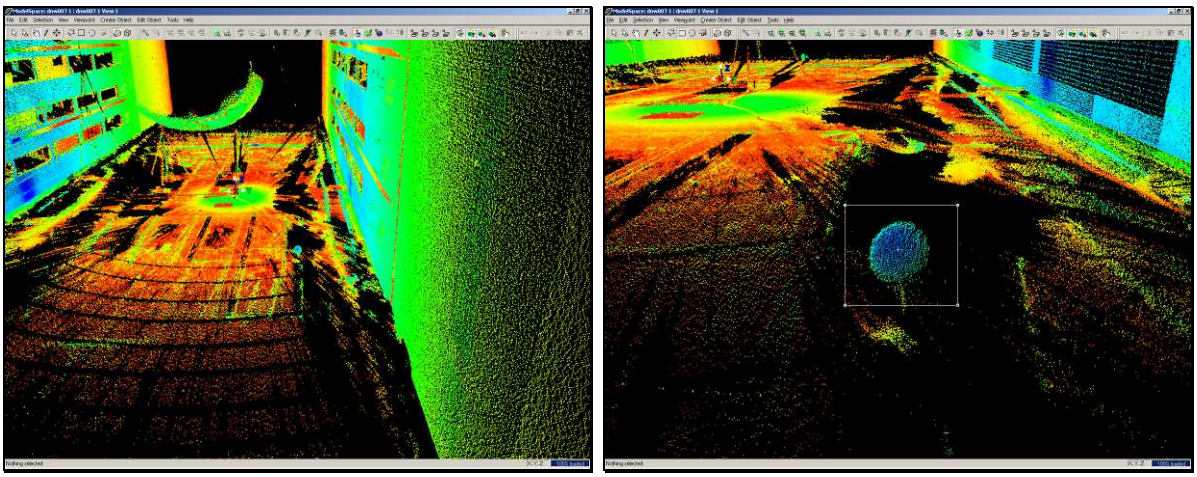

Figure B.3a/b: Left: View of the one of the scans in "rainbow" color scheme. Right: Zoom in on one of the reference spheres. The point cloud of the reference sphere is selected. [Source: Jochem Lesparre]

The process of registration requires that first certain geometric shapes are recognised that can later be used to match the point clouds. These can be for example planes, cylinders and spheres. Figure B.2 showed the registration spheres that were used in this project. Figure B.3a thru B.3d show the process of marking the registration spheres. Figure B.3a thru B.3c show that by turning the scan and modifying the selection from different angles a selelection containing only the points that belong to a registration sphere is made.

Figure B.3d shows the sphere that is fitted through the selected points. By matching the centers of the spheres from different scans, the scans can be combined to form a complete point cloud from the windtunnel with the kite without holes or shadows.

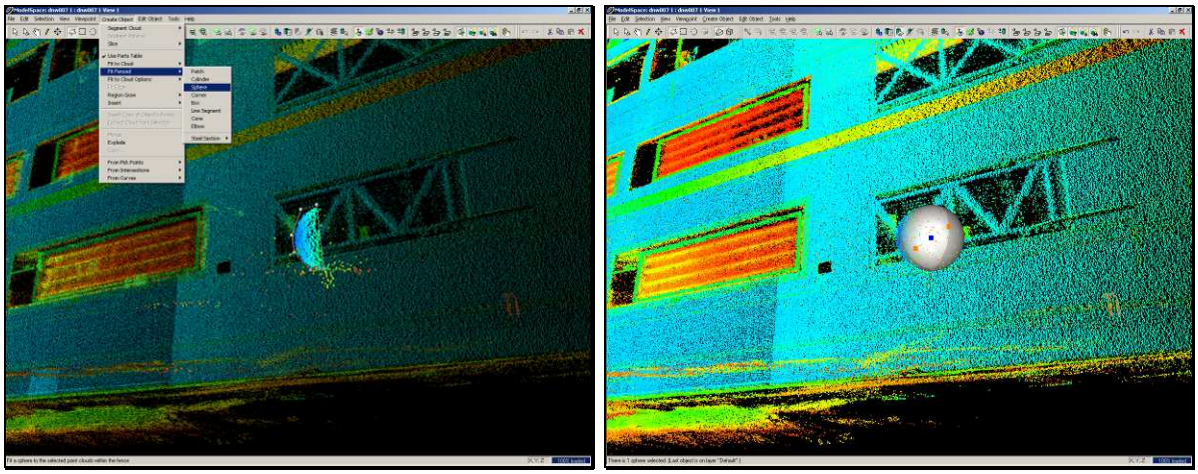

Figure B.3c/d: Left: the view from figure B.3b is rotated 90^{o} and the selection is further reduced to select only the points from the reference sphere. Right: A sphere of given radius is fitted through the point data. The center of this sphere is used for registering the different scans. [Source: Jochem Lesparre].

Appendix C: Introduction to photogrammetry

Photogrammetry is a method to extract measurements and 3D models from photographs. A photograph is in fact a two dimensional projection of three dimensional space. When photos are taken from different angles from an object, they can be combined to extract the three dimensional coordinates again.

When a photograph is made the image is not just an orthographic projection of 3D space. The image has a certain perspective and it is deformed by the lens and sensor of the camera. To be able to extract 3D data from 2D photographs first the deformation, that the projection underwent when the photograph was taken, must be corrected. The three most important distortions that an image undergoes when recorded by a photo camera are: radial distortion, decentring distortion and shear. How these distortions affect the image coordinates is shown in figure C.1.

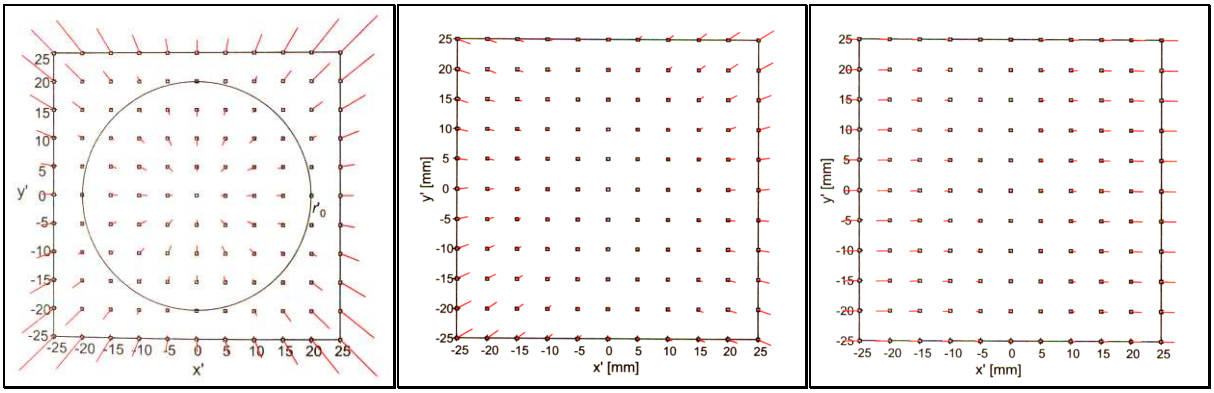

Figure C.1: From left to right the coordinate shift due to a radial, decentring and shear distortion of a photo or video camera. [18]

The total distortion of a camera is a function of the lens design, the focusing distance, object distance and the type of sensor. So first of all the right camera and lens must be chosen for a project. In principle photogrammetry can work with any photo camera: 35mm film, compact digital and SLR. In the case of this project there were a number of restricting requirements:

1. There was little light in the windtunnel
2. The target was moving
3. Some cameras were placed 1.5m from the kite
4. 14 cameras were used
5. The cameras needed to take photos synchronously

Point one requires a camera with high ISO speed and probably a fixed lens because zoom lenses transmit less light. Point two requires a short shutter time. This is contradicting with point one. Point three requires a lens with a sufficiently wide viewing angle. Point four demanded a decision if all lenses were going to be the same or if different lenses, with a longer focal length, were going to be used for the cameras that were placed further away from the kite. Using different lenses would require more time to correct the distortions of the different lenses. Point five meant that camera bodies were needed that could be remotely triggered by a single switch. After discussing these criteria with professional photographer Max Dereta and Nikon the Nikon D300 body with 28mm lens was choosen for all the cameras. These cameras can take good quality photos at ISO speeds of 1600 to 3200 and they can be remotely triggered by short circuiting three external contacts. The triggering scheme is shown in figure C.2. R are resistors of which the resistance depends on the voltage of the power source. OC are opto-couplers, a sort of optical relais. The camera is connected to this switch with a Nikon MC-22 cable. By pressing the pre-release switch the blue pole is shorted with the black pole. This wakes

up the camera from its stand-by modus and focusses the lens. When the release switch is then pressed together with the pre-release switch, also the yellow pole is shorted with the black pole and the camera takes a snapshot. By connecting the fourteen cameras in parallel to the pre-release and release switch all cameras are triggered synchronously. So this required 28 resistors, 28 opto-couplers and 14 MC-22 cables.

For this project the Photomodeler 5 software from EOS Systems Inc. was used. Photomodeler only corrects for the radial and decentring distortion. The shear distortion is caused when the pixels of a camera are rectangular instead of square. If it exist at all the effect is usually minor compared to the other two distortions.

Radial distortion is by far the largest factor that distorts an image. It causes an image to be displayed as if it is displayed on a sperical surface. The effect is most of all visible when using a so-called "fish-eye" or extreme wide angle lens. But also lenses with a smaller viewing angle have a certain amount of radial distortion.

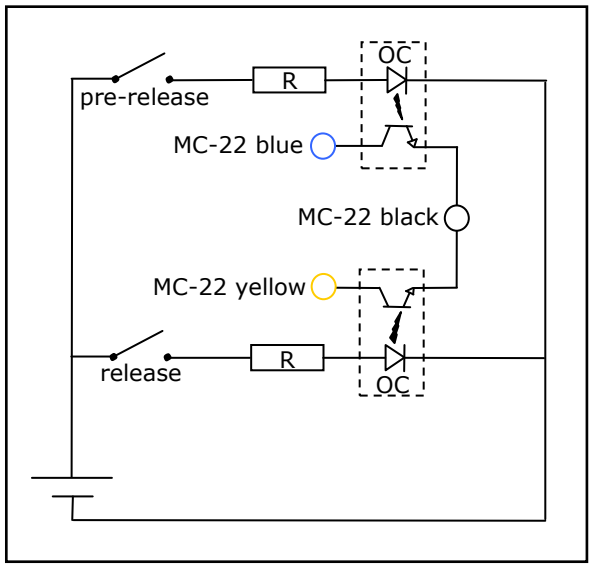

Figure C.2: Electrical scheme for triggering the Nikon D300 cameras remotely and synchronously.

Photomodeler corrects the radial distortion with the following formulas [29]:

$$drx = x \cdot dr \quad \text{(c.1)}$$

$$dry = y \cdot dr \quad \text{(c.2)}$$

where x and y are the coordinates in the image with respect to the principle point (roughly the center of the image for most cameras). drx and dry are the corrections of the x and y coordinate of the image and dr is the correction factor.

dr is defined by:

$$dr = K1 \cdot r^2 + K2 \cdot r^4 + K3 \cdot r^6 \quad \text{(c.3)}$$

where r is given by:

$$r^2 = x^2 + y^2 \quad \text{(c.4)}$$

K1, K2 and K3 are the radial lens distortion parameters. K3 is not used for all cameras. Because it causes a correction of the sixth order of the radius of the image it is mostly only applicable for wide angle lenses where the distortion near the edge of the photograph is very large.

The decentring distortion is caused by the lens not being exactly centered with respect to the sensor or by being at a slight angle with respect to the sensor. Decentring is corrected in the following way:

$$dpx = P1 \cdot \left(r^2 + 2 \cdot x^2\right) + 2 \cdot P2 \cdot x \cdot y \quad \text{(c.5)}$$

$$dpy = P2 \cdot \left(r^2 + 2 \cdot y^2\right) + 2 \cdot P1 \cdot x \cdot y \quad \text{(c.6)}$$

where dpx and dpy are the corrections in x and y direction and P1 and P2 are the decentring parameters. Usually the decentring correction is much smaller than the radial distortion correction.

The corrected image coordinates are then given by:

$$xc = x + drx + dpx \quad \text{(c.7)}$$

$$yc = y + dry + dpy \quad \text{(c.8)}$$

Determining the values of K1, K2, K3, P1 and P2 is done by camera calibration. Camera calibration means that eight photos are taken from a special calibration grid from specific angles and positions. The grid, shown in figure C.3, consists of 96 circular targets and 4 coded targets. After loading the eight calibration images into the software it marks and references the 100 targets. Because the relative position of the targets on the calibration grid is known the lens distortion parameters can be solved for, this is called processing. Referencing the images also gives the focal length of the lens and the camera stations from which the photos were taken.

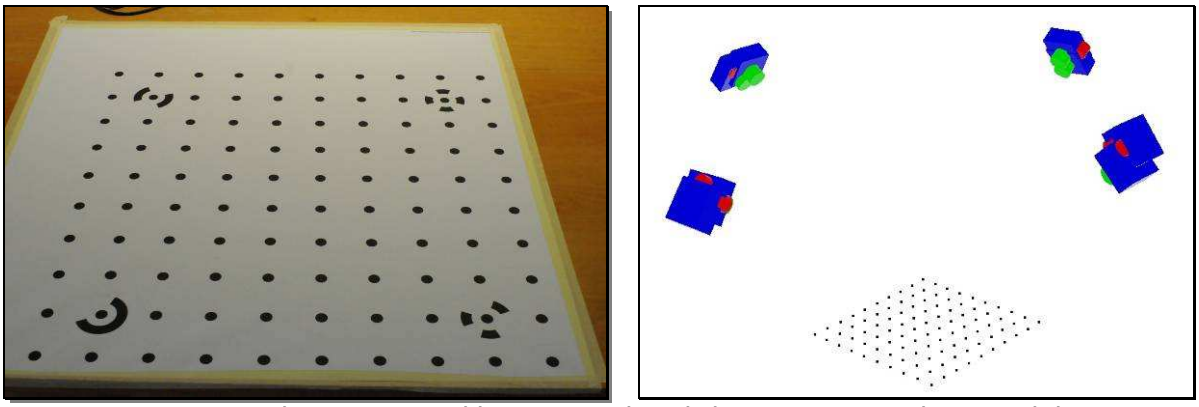

Figure C.3: The camera calibration grid and the 3D view in Photomodeler.

The calibration parameters are only valid for one focal length. So if a zoom lens is used the calibration is only valid for one zoom setting. In principle the calibration is also just valid for one focus distance. Because the calibration sheet needs to fill the image as far as possible to obtain a reliable calibration this can be a bit impractical. In practise that would mean that the calibration grid must have the size of the photographed object. In this project an A0 plot of the calibration sheet was used. For larger projects a projector can be used, but one has to keep in mind that the projector also uses a lens that has its own distortions. A small decrease in the project accuracy can be expected when using a projector or the wrong focus distance. The calibration parameters from the calibration project are used in subsequent projects.

To be able to accurately mark the targets with the software they need to have a certain minimum and maximum size and spacing. According to Luhmann [18] the optimum target size is in between 5 and 15 pixels (page 375). In principle Photomodeler can handle targets with a size of in between 5 pixels and 1/8th of the image size [29].

But it is advised to make the smallest target no smaller than 8 pixels and base the target size on that requirement. This shows the importance of a high resolution camera. The higher the resolution the smaller the targets can be and the closer they can be spaced together.

The minimum real size of a target can be calculated from the 8 pixel requirement using the following formula:

$$\text{minimum target diameter} = 8\,\text{pixels} \cdot \frac{\text{max distance} \cdot \text{format size}}{\text{focal length} \cdot \text{image size}} \qquad \text{(c.9)}$$

Max distance is the maximum distance from the camera to the target [mm], format size is the width of the sensor in the camera [mm], image size is the width of the image in pixels [mm] and focal length is the focal length of the lens [mm]. Filling in the numbers of this project gives:

$$\text{minum target diameter} = \frac{8 \cdot 6000 \cdot 22.8}{28 \cdot 4288} = 9.1\,\text{mm}$$

The targets used on the kite were standard 12mm round stationer's stickers.

The next step is to choose the camera stations to capture all targests on the object. There are a number of requirements that must be fulfilled by the camera stations:

- Every target must be seen by at least two cameras to be able to extract x, y and z coordinates from the targets. Only seeing a target with two cameras means that the targets must be referenced to each other by hand. Referencing cannot be done automatically by the software because there exists ambiguity in the solution.
- If a target is seen by three or more cameras the accuracy generally increases and the automatic target referencing becomes unambiguous.
- The angle between the cameras is important for reducing the referencing error and the confidence region of a target. When the angle between two cameras is 90 degrees the confidence region is a sphere. The smaller the angle gets the more the confidence region turns into a stretched ellipsoid, shown in figure C.4. The out-of-plane accuracy of the cameras decreases.
- The object must be image filling. If the targets only cover a small part of the image the orientation of the image is weak. This means that a small error in marking the targets will result a large error in the orientation angle of the image. More targets on the image spread the error and make the orientation stronger.

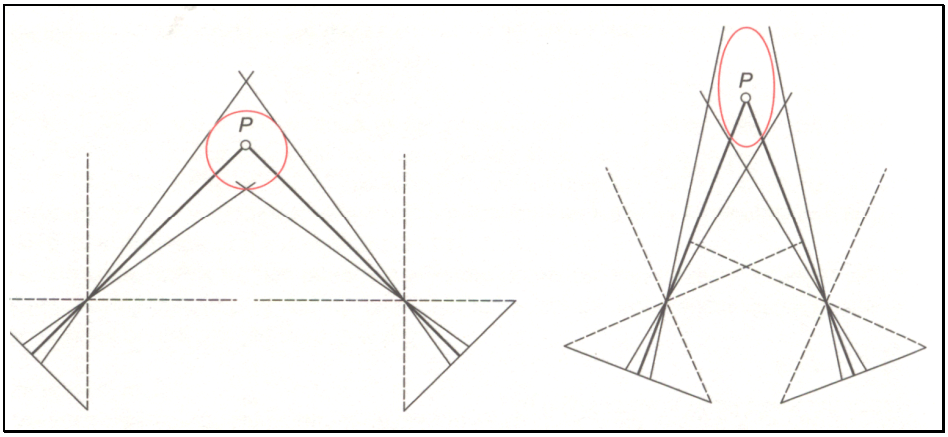

Figure C.4: Left: the ideal camera orientation. The cameras are at a 90° angle and the confidence region is sperical. Right: poor intersection of the cameras. The confidence region becomes an ellipsoid. [18]

The exact position of a target cannot be calculated by the software because the solution matrix of a photogrammetry project is over dimensioned. That means that there are more equations than there are variables to be solved. The position of the targets is determined by minimizing the root-mean-squared (RMS) error of a project. Graphically this means that from each camera there is a ray of light through a target. In an ideal situation these rays would intersect in 3D exactly at the center of the target. In reality, due to marking and calibration errors, these rays don't intersect but at some point there is a minimum distance between them. This distance is called the tightness. By minimizing the RMS distance to the rays the location of the target is found. By assuming that the error has a normal distribution around the location of the target there is certain confidence interval around the target in which the real target should be found. In Photomodeler the tightness (in millimeters) is used as a measure for the accuracy.

When photographing a complex curved surface such as a ram-air kite it is not possible to have all cameras at a 90° angle with respect to one another and use a reasonable amount of cameras. Neither is it possible to see all targets with more than two cameras. The trade off is in the accuracy versus the cost of the camera system and the post-processing time.

In this project 14 cameras were used. The 14 images had over 8000 markers on them. After referencing this resulted in a little over 2000 3D targets. Figure C.5 shows the marked targets on the kite. Approximately one quarter of these were only seen by two cameras. The others were seen by three to five cameras. The target marking was done semi-automatically. The targets that were placed exactly on the ribs were not planar anymore but folded in a V-shape due to the geometry of the kite. The software is only made to mark spheres or planer circles or ellipses. The non-planar targets had to be marked by hand. Because a large part of the targets was only seen by two cameras and because the automatic marking doesn't work very well when the targets are very close to each other, all referencing was done by hand. Referencing consists of making clear to the software that one target in one image is the same as another target in another image.

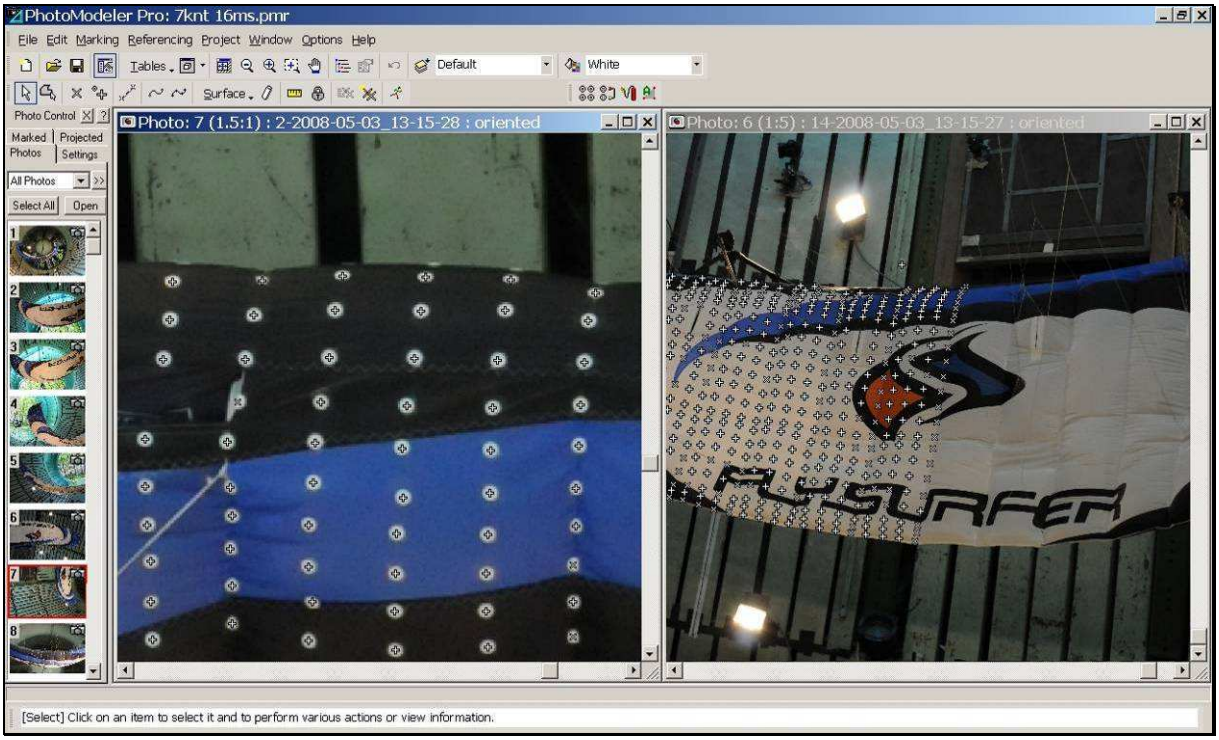

Figure C.5: Screen shot of Photomodeler showing the marked targets on the kite.

After all the points are marked and referenced the project is processed just like in the camera calibration. But in the calibration the relative location of the targets was known and the camera parameters were unknown. Now the camera parameters are known and taken from the calibration file and the relative position of the targets is unknown. From the calibration and referencing data the position of the targets is calculated. As explained before, this is done by numerically minimizing the RMS error of the referenced markers.

The result is a 3D view of all referenced targets and the location of the camera stations, shown in figure C.6. Also a table is constructed consisting of all information about the referenced and unreferenced markers. The most important properties in the table are the tightness as percentage of the project size and in meters, the error in pixels and the RMS error in pixels. These are important measures in marking accuracy. Excessive values of these properties usually indicate marking or referencing errors.

After the project is processed it needs to be scaled and oriented because photogrammetry only gives the relative position of the targets. Scaling was done with two markers on the windtunnel floor that were spaced 1500mm apart. Orienting was done using the same two targets on the floor and reference points on the grid that separated the test section from the fan of the windtunnel.

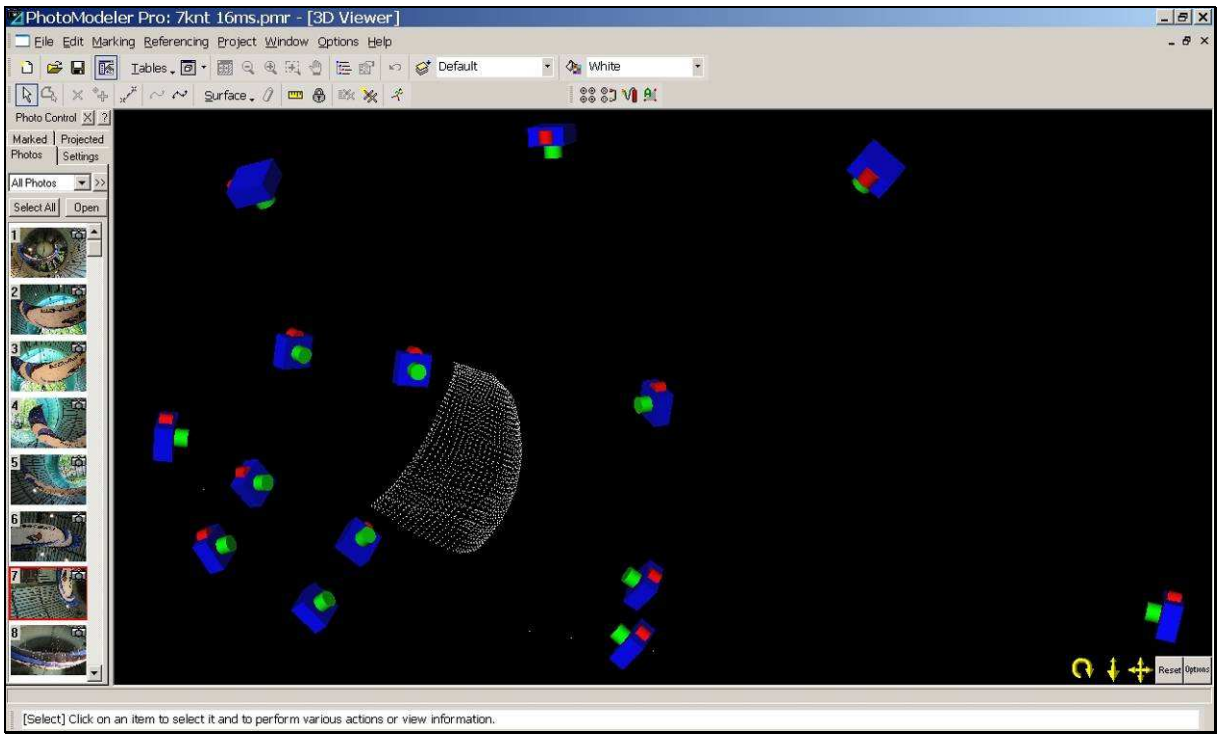

Figure C.6: 3D view of the processed project with all referenced targets and the camera station.

The scaled and oriented point cloud was exported in *.IGS format. This was then imported via the *import point cloud* function in the *digitized shape editor* of Catia. How the kite's surface was reconstructed with Catia is described in Appendix D. All in all generating a point cloud from the fourteen photos with 8000 markers took about five days: three days of target marking and two days of referencing and quality checking. A similar photogrammetry project undertaken by Simpson [24] had approximately 240 planar targets that were all seen by four cameras. This makes marking and referencing significantly easier because both can be done automatically. It should then be a matter of minutes.

Appendix D: Point cloud to CAD model

There are different techniques to turn a point cloud into surfaces. If the point cloud consists of simple geometric shapes, such as planes, cylinders and spheres, these shapes can easily be fitted through parts of the point cloud. Because the kite doesn't consist of such simply geometric shapes another technique, that can treat any complex geometry, can be used: triangulation. With triangulation triangles are drawn through each three neighbouring points. All the triangles together form the surface of the object.

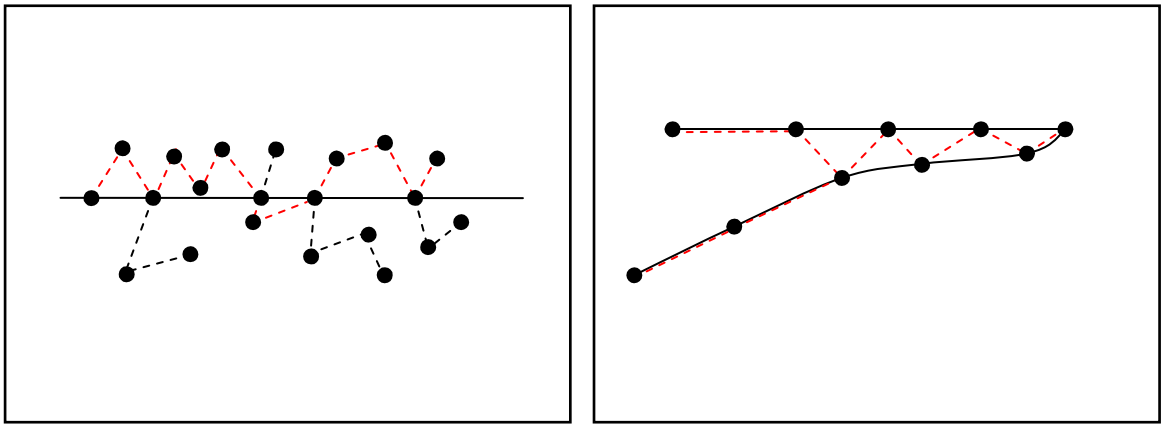

Figure D.1: Left: Point cloud with noise larger than the resolution. The black line represents the surface, red dashed line the surface fit and the black dashed lines are non-manifold protrusion. Right: The point spacing is larger than the distance between the surfaces.

In practice there are a number reason why triangulating a point cloud is not unambiguous. A common problem is that a triangulation algorithm uses a search distance to find the closest neighbours of a point. The problem arises when the noise is greater than the resolution of the scan or when two surfaces are very close to each other. Both situations are sketched in figure D.1. When the noise is greater than the resolution a very coarse, gritty surface is made, which looks a bit like sandpaper. Other than that there are usually non-manifold vertices. Those are vertices where the outer edges of their adjacent surface elements don't form a closed loop. Usually that means that there are surface elements that protrude (black dashed lines) form the continuous surface fit (red dashed lines). The right picture shows that when the point spacing is larger that the distance between the two surfaces that the two surfaces appear to be one surface.

Another problem with automatic mesh algoritms is that they usually leave holes in the mesh. At points where the algorithm doesn't understand the topology of the point cloud no surface mesh is made. All these three problems are present in figure 6.21 and 6.22 that were made with the automatic mesh algorithm of Catia.

A way around this last problem is the Powercrust code. It is an algorithm that never gives holes in a surface mesh. This is achieved by growing spheres from the inside of the point cloud. Their surfaces are merged where the spheres intersect the point cloud and each other. This results in a "watertight" surface. A few attempts were made by PhD candidate Jochem Lesparre, who does a PhD study on using laser data for CFD model generation, to use powercrust to mesh the kite. The result of these attempts is found in figure D.2a thru D.2c.

There were a number of problems though. First of all it was a lot of work to clean up the point cloud and remove enough of the outliers such that Powercrust could handle the point cloud. A second problem was that Powercrust couldn't manage to mesh the whole kite at once. This meant that the kite had to be meshed in parts. Once these parts are smoothed their edge contours have changed shape and they don't fit together very

well anymore. A third problem was smoothing itself. To remove the gritty surface texture the surface needed to be smoothed. Smoothing decreases the maximum angle between the adjacent triangles. This means that smoothing attacks the sharpest corners first. But the kite has such sharp corners also at the trailing edge, the tips and the ribs. Hence, smoothing also changes the global shape of the kite in these areas.

To be able to preserve the shape of the kite and have a smooth surface it was decided to make cross sections of the kite and to blend these together to make a smooth surface. The advantages of this method are that the surface is smooth and doesn't need to be smoothed afterward and that it gives a reasonable approximation of the raw data. A disadvantage is that only three cross sections per cell can be used. The reason for this is that in spanwise direction the curvature of the cell is approximated by a spline. If more then three cross sections are used the curvature of this spline is not uniform over the width of the cell but there is an unnatural curvature near the ribs (see figure D.3). By comparing the CAD model with the photographs from the kite and the raw point cloud data it was found that three cross sections per cell gave the best correspondence between the CAD model and the real kite.

The same method was used to reconstruct surface models from the photogrammetry. That is, five rows of targets per cell were glued on the kite. Three of these rows, two at the ribs and one at the cell center, were used to draw the cross sections. The other two were used to double check if the spanwise curvature was correct.

An exception to this method was the reconstruction of the surface of cell10, the tip. The difference in shape of the three cross sections of the tip was so large that Catia was unable to blend them together. For that reason the surface was made by triangulating the photogrammetry points. This gives a coarser surface approximation than blending the cross sections. But it was the only method that worked well.

The whole process of reconstructing the surface from the photogrammetry data is shown in figure D.4a thru D.4j.

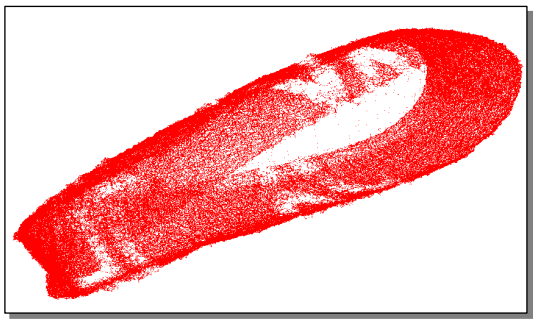

Figure D.2a: Raw point cloud from a laser scan. [Source: Jochem Lesparre]

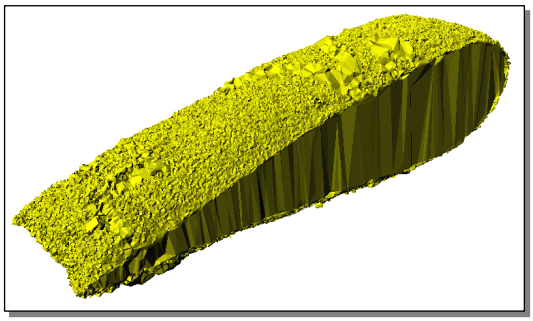

Figure D.2b: Raw surface mesh of the point cloud. [Source: Jochem Lesparre]

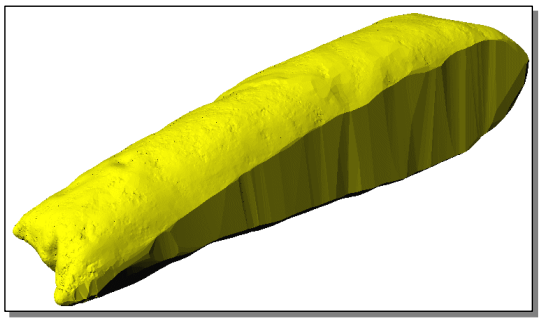

Figure D.2b: Smoothed surface mesh of the point cloud. [Source: Jochem Lesparre]

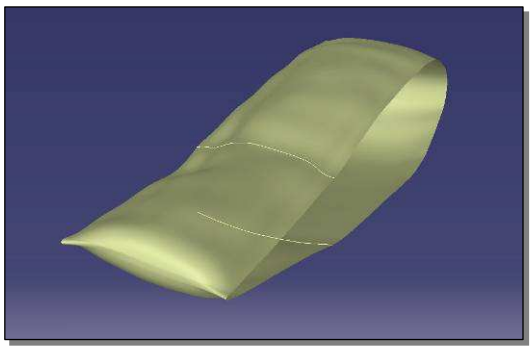

Figure D.3: Unrealistic spanwise curvature when more than three cross sections of the cell are blended together.

Figure D.4a: The point cloud that was exported from Photomodeler is imported in Catia.

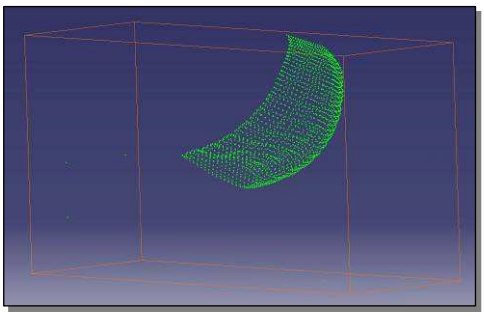

Figure D.4a

Figure D.4b: The ribs and the tip are isolated from the point cloud.

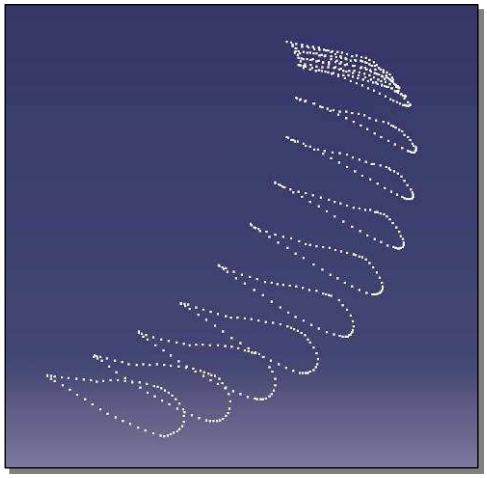

Figure D.4b

Figure D.4c: The cell centers are isolated from the point cloud.

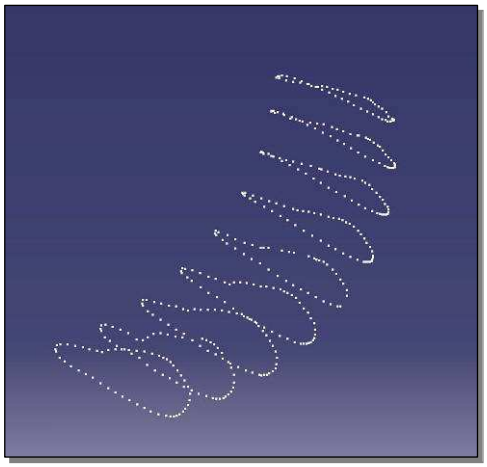

Figure D.4c

Figure D.4d: A cross section of the wing is drawn with a 3D spline.

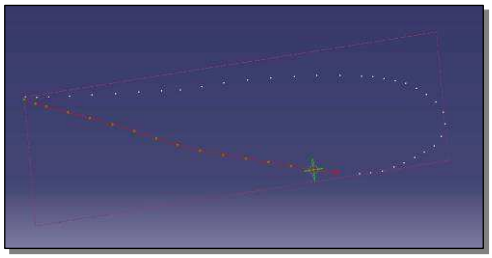

Figure D.4d

Figure D.4e: The cross sections of all ribs and cell centers are drawn.

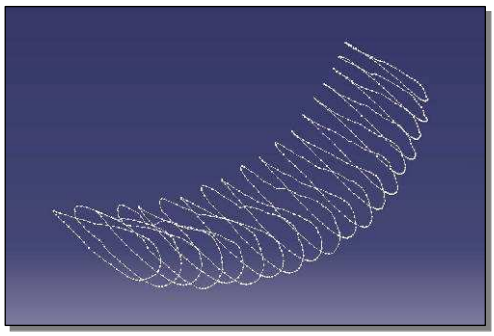

Figure D.4e

Figure D.4f: The curvature of the ribs and cell centers is checked for abnormal distribution. If necessary the tangency can be adapted.

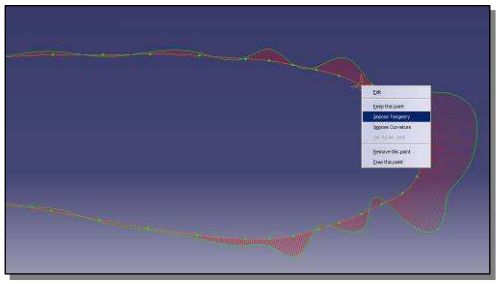

Figure D.4f

Figure D.4g: Every two ribs and corresponding cell center are blended together to form the surface of a cell.

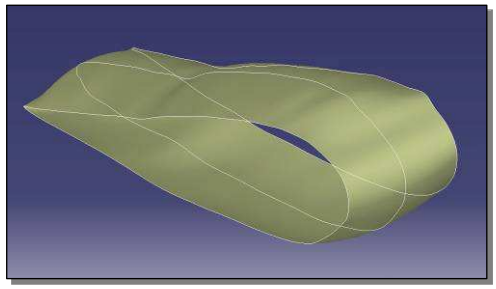

Figure D.4g

Figure D.4h: Cell10, the tip, forms an exception. Because of the odd shape of the tip Catia cannot blend the cross sections. For that reason the tip is triangulated instead of blended. This gives a surface that is coarser than the blended surface.

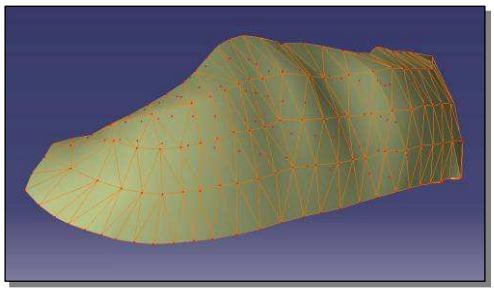

Figure D.4h

Figure D.4i: The angle of attack of the ribs is measured. The free stream vector is assumed to be parallel to the windtunnel walls and is projected in the plane of the rib. The angle between the chord and the projected free stream vector is the angle of attack of the rib.

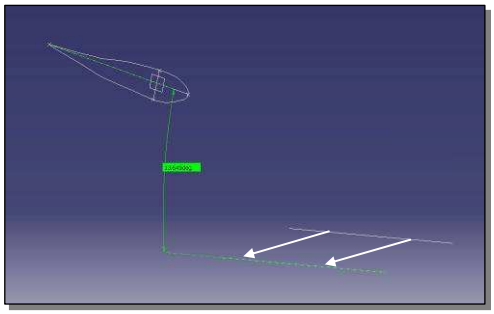

Figure D.4i

Figure D.4j: By blending the chords of the ribs the surface area of each cell is calculated. By projected the kite's surface in the ground plane the projected surface area of the cells is calculated.

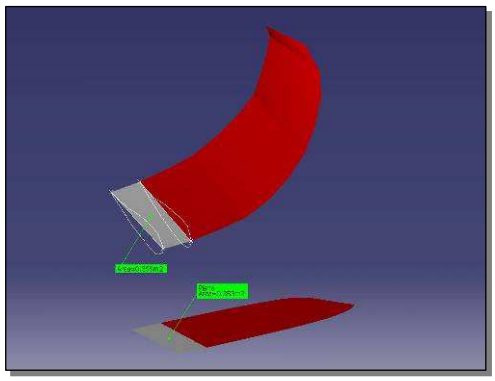

Figure D.4j